

**Free-form Lens Reconstruction of Hubble Frontier Fields
Galaxy Clusters**

**A DISSERTATION
SUBMITTED TO THE FACULTY OF THE GRADUATE SCHOOL
OF THE UNIVERSITY OF MINNESOTA
BY**

Kevin Wayne Sebesta

**IN PARTIAL FULFILLMENT OF THE REQUIREMENTS
FOR THE DEGREE OF
Doctor of Philosophy**

Advisor: Liliya L. R. Williams

September, 2018

© Kevin Wayne Sebesta 2018
ALL RIGHTS RESERVED

Acknowledgements

First and foremost I thank my advisor Liliya L. R. Williams. Working under your guidance during my tenure of graduate school has been a rewarding experience. I gained tremendous insight from being a part of the Hubble Frontier Fields project. Liliya helped me grow as a scientist by encouraging me to approach every problem with new perspectives. I am grateful for Liliya's wisdom.

I thank my committee Claudia Scarlata, Marco Peloso, and Yuichi Kubota. My committee challenged me to think about my research in new ways. Thanks to Claudia and Marco for spending time reviewing my thesis.

Thanks to my family for their everlasting love and support. I thank my parents for always believing in me and encouraging to pursue science. I thank my sister Keri and brother in law Chris for their unwavering support. I thank my niece Adalynn for her lively personality that refreshed me during challenging times.

Lastly, thanks to my friend Chris for his dedication in seeing to it that I graduate on time.

Many thanks to everyone who has helped me during my graduate career.

Dedication

I dedicate this thesis to my friends, without whom I would have finished sooner.

Abstract

Galaxy clusters, because of their massive size, act as powerful lenses for background objects. The Hubble Frontier Fields project was a multiyear international collaboration to examine six galaxy clusters acting as gravitational lenses with the aide of the Hubble Space Telescope. Lens modelling teams used shared data to reconstruct the cluster mass distributions using a variety of methods. We used our free-form method GRALE to solve for the mass distribution of each cluster. The only inputs used were related to the observed images, and unlike most other methods, no information about visible light of the cluster galaxies was part of the input. The lensing models produced by each modelling team were used to study magnified high redshift galaxies, and construct their luminosity functions. These scientific advances prepare the community ahead of the James Webb Space Telescope launch.

Upon reconstructing the cluster distributions, our goal was to see if light traces mass and investigate GRALE uncertainties. We focused on the first two Hubble Frontier Fields clusters, Abell 2744 and MACS J0416. No significant offsets were found between brightest cluster member galaxies and local mass peaks for either cluster on scales of $\approx 10 - 15kpc$. We calculated the correlation function between cluster core member galaxies and mass distribution for each cluster. Our results confirmed the standard biasing scenario of galaxy formation, meaning the clustering of galaxies is heavily influenced by the underlying dark matter distribution. We found light traces mass within HFF clusters, Abell 2744 and MACS J0416.

We directly compared two Abell 2744 GRALE reconstructions to gauge the robustness of calculated uncertainties, and confirmed that GRALE uncertainties were robust to changes in input data and slight modifications in the GRALE code parameters. Moreover, both maps produced relatively low Lens-plane RMS values, comparable to those of other methods. We explained our method for calculating Lens-plane RMS, while also providing multiple alternative definitions, because of a lack of consensus on the subject in the published literature.

Contents

Acknowledgements	i
Dedication	ii
Abstract	iii
List of Tables	vi
List of Figures	vii
1 Introduction	1
1.1 Gravitational Lensing	1
1.1.1 Categories of Gravitational Lensing	7
1.2 Massive and Merging Galaxy Clusters	7
1.3 Hubble Frontier Fields	9
1.4 GRALE	11
1.4.1 Plummer Spheres	12
2 Gracle reconstructions of HFF Clusters	13
2.1 GRALE reconstructions of all HFF clusters	13
3 Testing light-traces-mass in Hubble Frontier Fields Cluster MACS-J0416.1-2403	15
3.1 MACS-J0416.1-2403	15
3.2 Existing Mass Models of MACSJ0416	17
3.3 GRALE Setup	19
3.4 Results	20
3.4.1 Mass Contours and Local Mass Peak Offsets	20
3.4.2 Mass-Galaxy Correlation Function: GRALE	24

3.4.3	Mass-Galaxy Correlation Function: GRALE vs. LENSTOOL	28
3.5	Conclusions	31
4	Two free-form lens reconstruction of Hubble Frontier Fields Cluster Abell 2744	33
4.1	Abell 2744	33
4.2	Existing Mass Models of Abell 2744	34
4.3	GRALE Setup	38
4.3.1	HFFv3	38
4.3.2	HFFv4	39
4.4	Results of Lens Reconstruction	39
4.5	Influence of the mass to the North West of the main cluster	44
4.6	Comparing the distributions of light and mass in Abell 2744	44
4.6.1	Local Mass Peaks near Massive Galaxies	45
4.6.2	Mass-Galaxy Correlation Function	47
4.7	Conclusions	52
5	Lens-plane RMS	55
5.1	Introduction	55
5.2	imgsol.py: Algorithm to find forward projected image positions from GRALE output	55
5.3	Lens-plane RMS Definitions	57
6	Summary	59
	References	61
	Appendix A. Lens-plane RMS Code	67

List of Tables

2.1	GRALE reconstructions of the six HFF clusters	14
3.1	Previous MACS0416 mass models with type of data used and number of multiple images.	19
3.2	Offsets between galaxies G1-G4 and 30 mass models peaks in arcseconds. The third column is the root-mean-square dispersion between the galaxies and mass peaks. The last column is the significance, ratio between the distance and root-mean-square.	23

List of Figures

1.1	Incoming light ray at a point $\vec{\xi}$ on the lens plane, resulting in a deflection angle $\vec{\alpha}(\vec{\xi})$. Credit: Narayan & Bartelmann (1996)	3
1.2	Geometry of incoming light ray from background source S, being bent by a gravitational lens, and then arriving to the Observer O. The light ray is deflected by an angle $\vec{\alpha}$ at a distance $\vec{\xi}$ from the center of the lens. In the source plane, the background source is a distance η from the center of the lens. From the observer, θ is the angular position of the image and β is the angular position of the source. α is the difference between θ and β , also called the reduced deflection angle. D_d , D_{ds} , and D_s are the angular diameter distances separating the observer and lens, lens and source, and observer and source, respectively. Credit: Narayan & Bartelmann (1996)	4
1.3	Hubble image of Abell 2218 showing strong lensing features as arcs and multiple images of background sources. Credit: NASA, ESA, A. Fruchter and the ERO Team (STScI, ST-ECF)	8
2.1	HFFv1 GRALE mass reconstructions of the six HFF clusters. Color scale is projected density in units of kg/m^2 . Green dots are multiple images used in each reconstruction. Credit: Mohammed et al. (2016)	14
3.1	HST image of MACSJ0416. Credit: NASA, ESA and the HST Frontier Fields team (STScI).	16
3.2	Mass contours of averaged mass map of MACSJ0416 red overlaid on a HST F435W image. The blue lines represent the mass density contours and the red circles are images. There are 20 mass contour levels linearly spaced from 0.03827 g/cm^2 up to 0.76531 g/cm^2 . The green dots represent local mass peaks around the 4 central ridge galaxies, in 30 individual mass reconstructions. These galaxies are labeled G1-G4, with G1 appearing the brightest. .	21

3.3	Contours of fractional uncertainty in mass density of MACSJ0416. The contours are separated into two groups distinguishable by their colors. The six blue contour lines range from 3.3% to 19.8% in fractional mass density uncertainty, and the seven green lines range from 23.1% to 49.5%. Images are highlighted by red circles and the two BCGs are marked as magenta crosses.	22
3.4	Normalized galaxy-mass cross-correlation function for Subaru R-band at multiple magnitude cuts. The mass map is the average of 30 individual GRALE reconstructions. Rms dispersion between the 100 realizations of $D_m R_g$ is approximately 0.025 for all magnitude ranges. Shaded regions indicate 1σ error bars.	26
3.5	Differential number counts of galaxies over the entire Subaru field, not just the galaxies behind the cluster. The vertical dashed line marks the magnitude below which counts are incomplete; we did not include these galaxies in any of the analysis. The marked line, $d \log(n[m])/d \log(f) = 1$, is provided for comparison to the two bands.	27
3.6	Galaxy-mass cross-correlation functions for five Subaru R-band and one Z-band magnitude cut. Three mass maps are used: from the GRALE team (violet), CATS team (gold), and Sharon/Johnson (red). Shaded regions indicate 1σ error bars.	29
4.1	HST image of Abell 2744. Credit: NASA, ESA, and J. Lotz, M. Mountain, A. Koekemoer, and the HFF Team (STScI).	35
4.2	Mass contours of averaged mass map of Abell 2744 overlaid on a HST total (F435W, F606W, and F814W combined) image. <i>Left:</i> HFFv3; <i>Right:</i> HFFv4. The lines represent mass contour in units of g/cm^2 and red circles represent images used in the two reconstructions. The two BCGs are labelled as magenta crosses.	40
4.3	Contours of fractional uncertainty in surface mass density of Abell 2744, overlaid on the same HST image as in Fig. 4.2 with same field of view. <i>Left:</i> HFFv3; <i>Right:</i> HFFv4. The contours are linearly spaced by 10% and start at 10% (dark blue line). The left panel has a total of ten contour lines and the right panel has a total of eleven contour lines. Images are highlighted by red circles and the two BCGs are marked as magenta crosses.	41

4.4	<p><i>Left:</i> Difference map of the two mass reconstructions of Fig. 4.2, $\Delta_\Sigma = \Sigma_{v3} - \Sigma_{v4}$, where v3 and v4 are for HFFv3 and HFFv4 respectively. The solid contour lines are at $\Delta_\Sigma = 0, \pm 0.1, \pm 0.2$. <i>Right:</i> Map of the statistical significance of the difference map. The solid contour lines are at $\sigma_\Sigma = 0, \pm 2, \pm 4$. The yellow and green circles represent images that have a difference in redshift of $\delta(z_{v3} - z_{v4}) > 0.1$ and $\delta(z_{v3} - z_{v4}) < -0.1$, respectively. The size of the circle corresponds to the magnitude of difference in redshift. Both panels show the same region as in Fig. 4.2 and Fig. 4.3.</p>	42
4.5	<p>Zoomed in area of Fig. 4.2, spanning $35.6''$ by $49.6''$, with the left and right panel showing HFFv3 and HFFv4 respectively. Magenta points represent peaks of 40 mass reconstructions in the projected surface mass density around four main galaxies, labelled G1-G4. These points were slightly displaced from their positions by random amounts to make them visible. (The points were obtained on a grid, so many were superimposed.) Red crosses are the images used for each reconstruction version. Contours lines match the scale from Fig.4.2, but only extend up to 0.7 g/cm^2. Higher density contour lines were left out for clarity around local mass peak points. A zoomed in region around G1 and G2 of HFFv4 is provided in the right panel. It uses a lighter gray scale shading to highlight the region between the two galaxies.</p>	46
4.6	<p>The left and right panel show normalized galaxy-mass correlation functions for R-band Subaru galaxies with HFFv3 and HFFv4 averaged mass maps, respectively. These calculations were done in a circular region centered on the core of Abell 2744 and over eight magnitude cuts of the galaxies. Each magnitude cut is color coded and has the number of galaxies within it listed. An additional correlation function (gray) is done for HFFv3 which is the same as the $m_R \leq 20$, but with galaxies G1-G3 removed. Shaded regions are 1σ error bars, such that the RMS dispersion for 100 randomizations of $D_m R_r$ is between 0.01 and 0.025 for both panels.</p>	48
4.7	<p>Same plot as Fig.4.6 with normalized galaxy-mass correlation functions for Z-band Subaru galaxies with HFFv3 and HFFv4 averaged mass maps on the left and right panels, respectively. These calculations were done in a circular region centered on the core of Abell 2744 and over nine magnitude cuts of the galaxies.</p>	50

4.8	Differential number galaxy counts versus magnitude of Subaru R-band and Z-band galaxies. Because of low number counts in the cluster region, the field of view used is the entire Subaru region. A dashed vertical line indicates where the catalogue suffers from incompleteness. A solid line with slope equal to one is provided for reference.	51
4.9	Plot of magnitudes of Subaru galaxies against BPZ redshifts. Blue dots indicate R-band Subaru galaxies and red x's are Z-band Subaru galaxies. Two lines are provided for clarity, one on the cluster redshift, $z = 0.308$, and the other at the magnitude $m = 24$ separating our two magnitude cuts. . .	53

Chapter 1

Introduction

1.1 Gravitational Lensing

Gravitational lensing is the bending of light by the presence of mass. The effects of gravitational lensing was predicted long before the work of Albert Einstein but not fully worked out until the General Theory of Relativity. Assuming a point mass M , the deflection of an incoming light ray a distance ξ in the lens-plane, away from the mass, predicted by General Relativity is

$$\hat{\alpha} = \frac{4GM}{c^2\xi}, \quad (1.1)$$

where c is the speed of light and G is the Gravitational constant. Assuming the gravitational field is weak, the field equations of General Relativity can be linearized. In this regime the deflection of light from an extended body can be approximated as a sum of deflections due to point masses. Another approximation, the thin lens approximation, used in gravitational lensing assumes that the thickness of the lens is much smaller than the distances between the lens, observer and source. Then, given a volume of mass, with density ρ , the projected surface mass density in the z direction, or line-of-sight direction, can be described by

$$\Sigma(\vec{\xi}) = \int \rho(\vec{\xi}, z) dz, \quad (1.2)$$

where $\vec{\xi}$ is a two dimensional vector in the plane of the lens. By summing the deflections from every mass element, the total deflection at a point $\vec{\xi}$ in the plane is

$$\vec{\alpha}(\vec{\xi}) = \frac{4G}{c^2} \int \frac{(\vec{\xi} - \vec{\xi}') \Sigma(\vec{\xi}')}{|\vec{\xi} - \vec{\xi}'|^2} d^2\xi'. \quad (1.3)$$

A schematic of a light ray being deflected at a point $\vec{\xi}$ in the lens plane can be seen in Fig. 1.1. The light ray then comes to the observer after having its path bent by the lens. The difference in the observed image position, $\vec{\theta}$, and the unlensed source position, $\vec{\beta}$, is the deflection angle multiplied by a ratio of angular diameter distances, as seen in Fig. 1.2.

From this geometry, the reduced deflection angle can be introduced

$$\vec{\alpha} = \frac{D_{ds}}{D_s} \vec{\alpha}, \quad (1.4)$$

where D_{ds} and D_s are angular diameter distances between the lens and source and between the observer and source, respectively. A quick primer on standard cosmology now. Angular diameter distance is the ratio of the physical size of an object to the angular size. The angular diameter distance is then

$$D_A(z) = \frac{d_c(z)}{1+z}, \quad (1.5)$$

where z is the redshift of an object and d_c is the comoving distance. The comoving distance, is the distance between observer and an object at redshift z , measured at the present cosmological time. The proper distance is defined as the distance measured between two points at the same time. The comoving distance and proper distance are related to each other by

$$d_c = \int_{t_{obs}}^t c \frac{dt'}{a(t')}, \quad (1.6)$$

where $a(t)$ is the scale factor and parametrizes the expansion of the Universe. The scale factor describes how the Universe is changing size with respect to time, or the ratio of the proper distance at time t and the distance at reference or present time t_o , $a(t) = \frac{d(t)}{d_o}$. At present time, $a(t_o) = 1$. The comoving distance can then be thought of as the distance between two objects without the expansion of the Universe. The scale factor is related to the redshift of an object as

$$\frac{1}{a(t)} = 1+z, \quad (1.7)$$

where t is the time from which a photon was emitted from the object at redshift z . The rate of expansion of the Universe is defined as the Hubble parameter

$$H(t) = \frac{\dot{a}}{a}, \quad (1.8)$$

where \dot{a} is the time derivative of the scale factor. The contents of the Universe, or how much the Universe is made of each thing x , can be defined with the density parameter Ω_x

$$\Omega_x = \frac{8\pi G\rho_x(t_o)}{3H_o^2}, \quad (1.9)$$

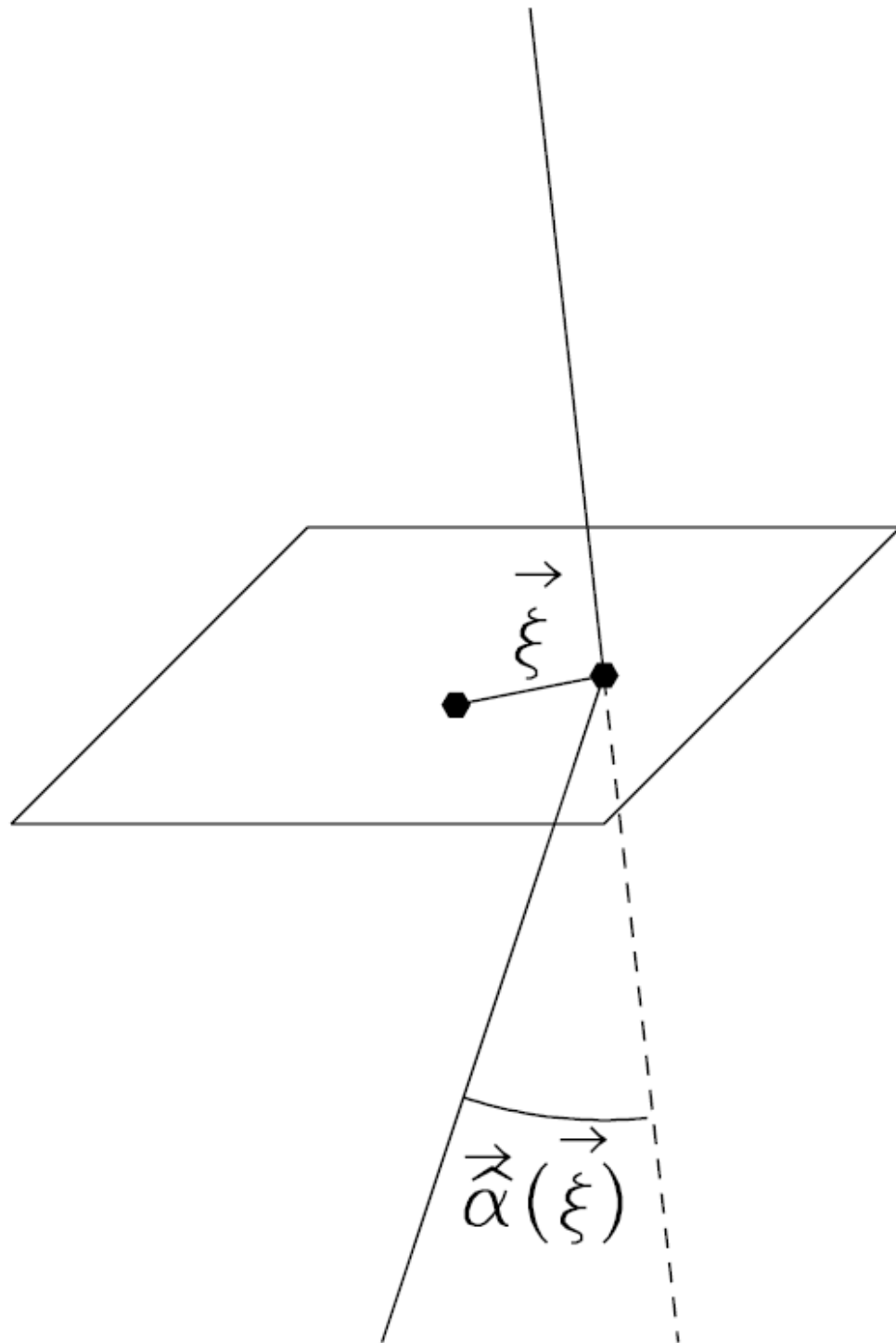


Figure 1.1 Incoming light ray at a point $\vec{\xi}$ on the lens plane, resulting in a deflection angle $\vec{\alpha}(\vec{\xi})$. Credit: Narayan & Bartelmann (1996)

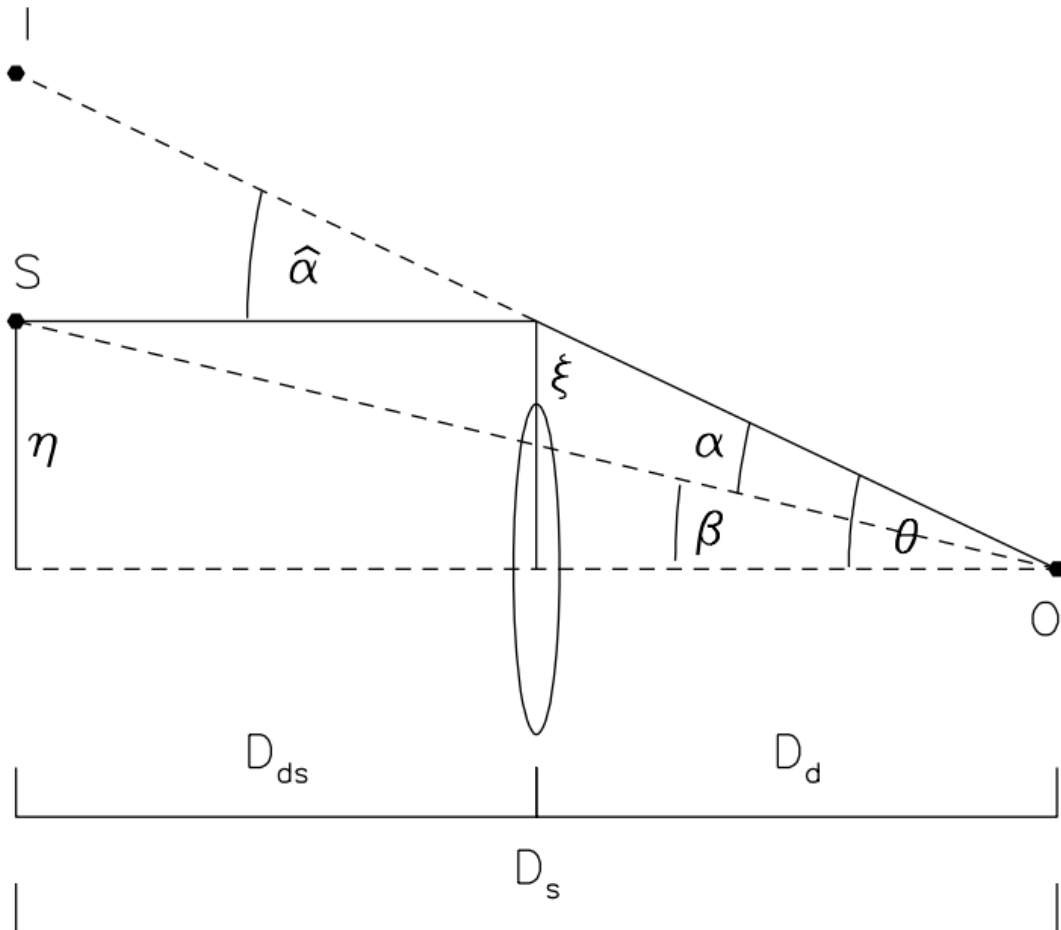


Figure 1.2 Geometry of incoming light ray from background source S , being bent by a gravitational lens, and then arriving to the Observer O . The light ray is deflected by an angle $\hat{\alpha}$ at a distance ξ from the center of the lens. In the source plane, the background source is a distance η from the center of the lens. From the observer, θ is the angular position of the image and β is the angular position of the source. α is the difference between θ and β , also called the reduced deflection angle. D_d , D_{ds} , and D_s are the angular diameter distances separating the observer and lens, lens and source, and observer and source, respectively. Credit: Narayan & Bartelmann (1996)

where x is radiation, matter, or dark energy Λ . The comoving distance depends on the cosmology chosen, but for standard Λ CDM cosmology the curvature is assumed to be zero, $\Omega_k = 0$, and the density parameter of radiation is near zero, $\Omega_{rad} \approx 10^{-4}$, the form is simple

$$d_c(z) = d_H \int_0^z \frac{dz'}{\sqrt{\Omega_m(1+z')^3 + \Omega_\Lambda}}, \quad (1.10)$$

where $d_H = \frac{c}{H_0}$ is the Hubble distance and Ω_m and Ω_Λ are the density parameters of matter and dark energy, respectively. In general for angular diameter distances, $D_s \neq D_d + D_{ds}$ because of the cosmology involved.

Now that angular diameter distances have been defined, and using Eq. 1.4, the lens equation can be properly introduced

$$\vec{\beta} = \vec{\theta} - \vec{\alpha}(\vec{\theta}) = \vec{\theta} - \frac{D_{ds}}{D_s} \vec{\alpha}(\vec{\xi}). \quad (1.11)$$

As seen from Fig. 1.2, this equation states that the difference in the position of the observed images, $\vec{\theta}$, and unlensed source position, $\vec{\beta}$, is the reduced deflection angle, $\vec{\alpha}$. This equation can have multiple image solutions from the same source, a phenomena called multiple imaged or strong lensing. When the lens is a point mass and the source sits right behind the lens $\vec{\beta} = 0$, we can use Eq. 1.1 to get the observed image position

$$\theta_E = \sqrt{\frac{4GM}{c^2} \frac{D_{ds}}{D_d D_s}}. \quad (1.12)$$

The observed image of the background source is produced an a ring, known as an Einstein Ring. When the point-like background source sits off axis, a ring will no longer be produced but two images will be.

Most astronomical lenses are not treated as a point mass, due to the complexity of their total mass distribution, or projected surface mass density $\Sigma(D_d \vec{\theta})$. The convergence is defined as

$$\kappa(\vec{\theta}) = \frac{\Sigma(D_d \vec{\theta})}{\Sigma_{cr}}, \quad (1.13)$$

where Σ_{cr} is the critical surface density of the lens. The critical surface density is defined as

$$\Sigma_{cr} = \frac{c^2}{4\pi G} \frac{D_s}{D_d D_{ds}}, \quad (1.14)$$

so that given a lens with surface density equal to the critical surface density, $\Sigma = \Sigma_{cr}$, the observed image position is equal to the reduced deflection angle, $\vec{\theta} = \vec{\alpha}$, and the unlensed position is zero, $\vec{\beta} = 0$. When this happens, the resulting image is an Einstein ring as

noted before. Using Eq. 1.4, the reduced deflection angle can be written in terms of the convergence as

$$\vec{\alpha}(\vec{\theta}) = \frac{1}{\pi} \int \frac{(\vec{\theta} - \vec{\theta}') \kappa(\vec{\theta}')}{|\vec{\theta} - \vec{\theta}'|^2} d^2\theta'. \quad (1.15)$$

From the convergence, an effective lensing potential can be defined as

$$\psi(\vec{\theta}) = \frac{1}{\pi} \int \kappa(\vec{\theta}') \ln |\vec{\theta} - \vec{\theta}'| d^2\theta', \quad (1.16)$$

such that

$$\vec{\alpha}(\vec{\theta}) = \vec{\nabla}\psi(\vec{\theta}), \quad (1.17)$$

and

$$\kappa(\vec{\theta}) = \frac{1}{2} \nabla^2 \psi(\vec{\theta}), \quad (1.18)$$

are satisfied. The lensing potential can be defined in terms of the gravitational potential of the lens as

$$\psi(\vec{\theta}) = \frac{2D_{ds}}{D_d D_s c^2} \int \Phi(D_d \vec{\theta}, z) dz. \quad (1.19)$$

The transformation matrix, or the Jacobian, between the lensed and unlensed coordinates is therefore given by

$$A_{ij} = \frac{\partial \beta_i}{\partial \theta_j}. \quad (1.20)$$

Using the lens equation and definition of the deflection angle in terms of the lensing potential, the transformation matrix can be rewritten as

$$A_{ij} = \delta_{ij} - \frac{\partial^2 \psi}{\partial \theta_i \partial \theta_j}, \quad (1.21)$$

where δ_{ij} is the Kronecker delta. This matrix shows how sources are distorted by gravitational lenses. To get a clearer picture of this, we define the shear tensor as

$$\begin{aligned} \gamma_1(\vec{\theta}) &= \frac{1}{2} \left(\frac{\partial^2 \psi}{\partial \theta_1 \partial \theta_1} - \frac{\partial^2 \psi}{\partial \theta_2 \partial \theta_2} \right) = \gamma(\vec{\theta}) \cos 2\phi(\vec{\theta}), \\ \gamma_2(\vec{\theta}) &= \frac{\partial^2 \psi}{\partial \theta_1 \partial \theta_2} = \gamma(\vec{\theta}) \sin 2\phi(\vec{\theta}), \end{aligned} \quad (1.22)$$

where ϕ is the orientation angle and the shear scalar is $\gamma = \sqrt{\gamma_1^2 + \gamma_2^2}$. The transformation matrix can then be rewritten as

$$A_{ij} = (1 - \kappa) \begin{bmatrix} 1 & 0 \\ 0 & 1 \end{bmatrix} - \gamma \begin{bmatrix} \cos 2\phi & \sin 2\phi \\ \sin 2\phi & \cos 2\phi \end{bmatrix}. \quad (1.23)$$

The convergence causes a uniform expansion of the image of the background source, whereas the shear tangentially stretches the source. The surface brightness from background sources is preserved during gravitational lensing. This causes magnification of the

image because of the change in solid angle of the source. The magnification can then be written as

$$\mu = \frac{1}{\det A} = \frac{1}{[(1 - \kappa)^2 - \gamma^2]}, \quad (1.24)$$

with the definition of the magnification matrix as inverse of the transformation matrix.

Magnification can be either positive or negative, which correspond to different image properties. When magnification is positive, the parity of the source is preserved, whereas when magnification is negative the image is flipped like a mirror image. Where the magnification is infinite, this represents critical lines in the lens plane. Around critical lines, images merge with one another and form arcs. These lines projected back to the source plane are known as caustic lines. If the background source's position were to move over a caustic line, two images would be created or destroyed depending on the direction of movement.

1.1.1 Categories of Gravitational Lensing

Gravitational lensing occurs in three classes: (i) strong lensing, (ii) weak lensing, and (iii) microlensing. Strong lensing is when multiple images, usually as rings or arcs, of the background source are produced. These strong lensing features can be seen in the galaxy cluster Abell 2218 in Fig. 1.3. For strong lensing to occur, the projected mass density of the lens has to be greater than the critical surface density, $\Sigma \gtrsim \Sigma_{cr}$, at some location in the lens plane. Because of this condition, strong lensing is mostly found within galaxy clusters or massive galaxies as lens. Weak lensing produces distortions of the background sources, but no multiple images, on a larger scale. The background sources, typically galaxies, are tangentially stretched and magnified by the foreground mass. The massive size of galaxy clusters makes them a common occurrence of weak and strong lensing. The last class of gravitational lensing, microlensing, usually occurs on smaller scales where the distortion of shape is difficult to detect. Multiple images are produced, but the image separation is very small $\delta\theta \lll 1''$. However, the light received from the background source changes with time.

1.2 Massive and Merging Galaxy Clusters

According to the standard hierarchical model of structure formation, the earliest objects to form in the universe come from the gravitational collapse of the initial density perturbation of the Universe (Kravtsov & Borgani, 2012). Given the mean mass density of the Universe,

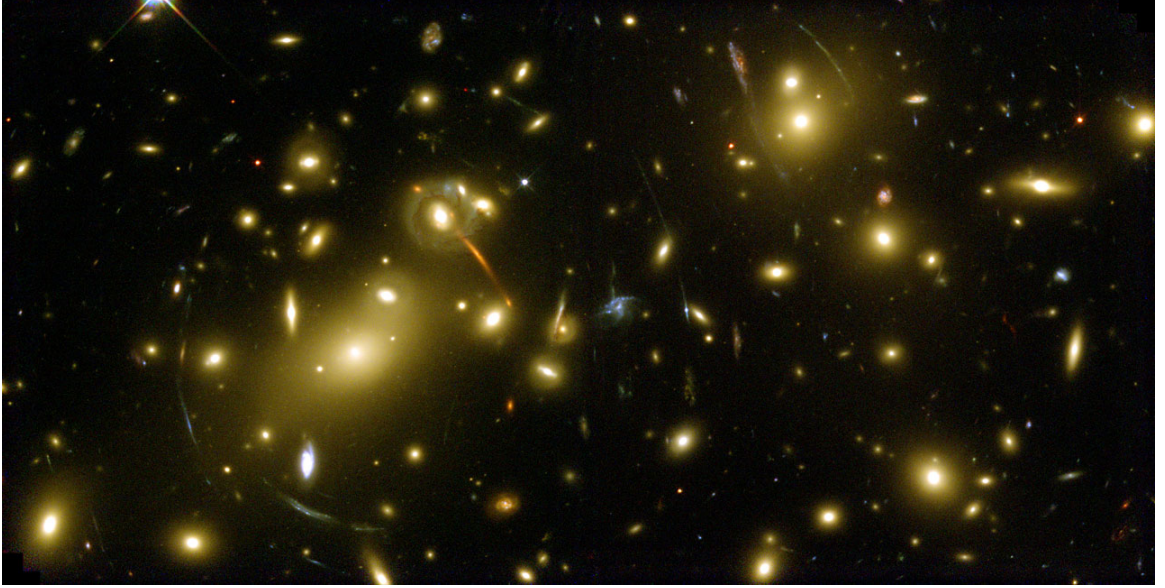


Figure 1.3 Hubble image of Abell 2218 showing strong lensing features as arcs and multiple images of background sources. Credit: NASA, ESA, A. Fruchter and the ERO Team (STScI, ST-ECF)

$\bar{\rho}_m$, the density contrast is defined as

$$\delta(\vec{x}) = \frac{\rho(\vec{x}) - \bar{\rho}_m}{\bar{\rho}_m}, \quad (1.25)$$

and describes local enhancements and deficits of the underlying density. First, small scale fluctuations in the density field form. The amplitudes of these fluctuations are characterized by linear growth theory when $\delta(\vec{x}) \ll 1$. Eventually, these fluctuations grow to a size, $\delta(\vec{x}) \gg 1$, where nonlinear growth theory is needed. Dark haloes form and merge together into bigger halos. Baryonic matter then collapses into these halos and starts the formation of stars and galaxies. Galaxies merge together to form galaxy clusters. The mass of a galaxy cluster is dominated by the dark matter halo(s). Dark matter halos have been routinely modeled with the Navarro-Frenk-White (NFW) density profile:

$$\rho_{NFW}(r) = \frac{\rho_o}{\frac{r}{r_s} \left(1 + \frac{r}{r_s}\right)^2}, \quad (1.26)$$

where r is the radius of the halo, r_s is the scale radius, and ρ_o is a scaling parameter (Navarro et al., 1996). Besides the dark matter halo(s), galaxy clusters are made up of galaxies and gas of the intracluster medium (ICM). Their total mass is usually between 10^{14} - $10^{15} M_\odot$.

Galaxy clusters are either dynamically active and in an ongoing merger between the

galaxy members, or relaxed. The gas within a merging cluster is heated up from infall of cluster members. Merging clusters have been identified by extended radio halos in their centers or smaller radio relics in the outer regions of the clusters (Ferrari et al., 2008). Similarly, peculiarities in the distribution of X-ray emission of the ICM appear in merging clusters. Other signatures have been in the offsets between mass and X-ray distributions in the 'Bullet Cluster', (Markevitch et al., 2004), or offsets between mass and the Brightest Cluster Galaxies (BCGs) in Abell 3827 (Massey et al., 2015), although the offsets may not be significant, (Massey et al., 2018). Relaxed clusters are characterized by large X-ray peaked emissions from the ICM plasma cooling down (Hudson et al., 2010). Throughout the evolution of the Universe, galaxy clusters have come to exist in many states.

1.3 Hubble Frontier Fields

Deep field surveys have looked at the earliest and most distant galaxies to gain insights into the origins of the early Universe. The launch of the *Hubble Space Telescope* (*HST*) provided the opportunity to investigate these faint and distant galaxies at depths never seen before. The Hubble Deep Field observations in 1995 were the first to utilize the power of the HST to capture these galaxies, (Williams et al., 1996), followed by HDF-South in 2000 (Casertano et al., 2000). A significant number of galaxies were detected, with redshifts out to $z \approx 5$. Many of those galaxies showed signs of ongoing star formation. Over the years, more deep field imagery, with aid of the Advanced Camera for Surveys (ACS) in 2002 and Wide Field Camera 3 (WFC3) in 2009, pushed the boundaries of galaxy detections at high redshifts (Great Observatories Origins Deep Survey (GOODS): Giavalisco et al., 2004, Hubble Ultra Deep Field: Bouwens et al., 2010). Detections of galaxies with a redshift $z > 9$ were now possible, albeit small in number, (Brammer et al., 2013; Finkelstein et al., 2015).

Another technique for studying distant galaxies is to utilize the lensing, magnifying power of massive galaxy clusters foreground to the galaxies. A recent study, The Cluster Lensing And Supernova survey with Hubble (CLASH), focused on 25 galaxy clusters to study properties of galaxies in the early universe. These discoveries and the planned future launch of the James Webb Space Telescope (*JWST*), motivated the proposal of the Hubble Frontier Fields initiative (Bullock et al., 2012).

The Hubble Frontier Fields program (hereafter HFF) was a multi-year program, using the *HST* and *Spitzer Space Telescope* (*Spitzer*), to study six massive galaxy clusters and associated parallel fields Lotz et al. (2017). By utilizing the WFC3 and ACS, scientists obtained the deepest observations of galaxy clusters ever. The primary science goals of the

HFF program were to (i) find new populations of galaxies at $z = 5-10$ (ii) gain insight into star-forming galaxies at the earliest ages of the Universe (iii) quantitatively study the structure of star-forming galaxies at $z > 5$ (iv) use powerful cluster lenses to be able to see the composition of the faintest galaxies, $z > 8$ (Bullock et al., 2012; Lotz et al., 2017). Starting with 25 clusters from Bullock et al. (2012) and other community recommendations, six clusters were chosen to meet these goals: Abell 2744, MACSJ0416.1-2403, MACSJ0717.5+3745, MACSJ1149.5+2223, Abell S1063, and Abell 370. Each cluster and associated parallel field was observed for two epochs of *HST* time, totaling over 840 *HST* orbits. Lens modeling teams were invited to apply their reconstruction methods to solve for the mass distributions of the HFF clusters. Preliminary mass models were produced by five teams using pre-HFF data to help upcoming observations (Coe et al., 2015). Additional lens modeling teams joined as the HFF program progressed. Updated mass models of every cluster were produced with new spectroscopic and weak-lensing data, where available, by each lens modeling team. Every lens mass model can be found on the MAST website.¹

The goal of lens reconstruction techniques is to build mass models of the lens constrained by the gravitational lensing data, which, for strong lensing consists of identifications, positions and redshifts of multiple images of background sources. There are a few different lens inversion methods in existence, based on one of the two different approaches to lens reconstruction – parametric and non-parametric, or free-form. Some methods are hybrid (Diego et al., 2015), and incorporate features of both approaches. Parametric methods assume an underlying functional form of the mass distribution of the lens, and the lensing data is used to constrain the parameters of the functional form. The number of parameters is usually small (10-50), and statistical inference can be made using regular sampling methods, like Markov-Chain Monte-Carlo (MCMC). Though in principle these physical models can take any form, in practice parametric models assign mass to cluster galaxies, assuming light-traces-mass, and add a few additional mass components to represent the large-scale cluster dark matter. One widely used example of such techniques is LENSTOOL (Jullo et al., 2007).

On the other hand, non-parametric models (or free-form) solve for the lensing mass by using the images data alone, with no reference to cluster galaxies. Some free-form methods match the number of free parameters to the number of lensing observables, while others work with a parameter space whose dimensionality greatly exceeds the number of constraints. An example of the latter type of method is GRALE (Liesenborgs et al., 2006, 2007, 2008, 2009) which uses no light information from the lens, and requires only the position and redshifts of the multiple images of the background sources.

¹ <https://archive.stsci.edu/prepds/frontier/lensmodels/>

This dissertation uses the free-form lens reconstruction method of GRALE and strong lensing data to investigate two HFF clusters: Abell 2744 and MACS-J0416.1-2403.

1.4 Grale

GRALE is a free-form technique of lens reconstruction that uses a genetic algorithm to calculate the mass distribution of a lens. Only the images' identifications, locations and redshifts are used as inputs for GRALE. The images' positions can be modeled either as point sources or as extended regions. To start, a uniform grid is initialized with fixed width, projected Plummer mass distributions. These Plummer spheres are used as the basis set. The genetic algorithm then searches for the best solution of the mass distribution, in nine successive steps, according to a fitness value with two components, to be described later. At each step, the genetic algorithm refines the original grid, subdividing it into smaller grid cells where mass density is high, and places a Plummer sphere in each grid, with its size matching the size of the grid cell, and its mass determined by the constraints provided by the lensed images. Through each iteration, reproduction and mutation are used to breed new solutions. After this process is repeated nine times, GRALE obtains a final mass distribution (Liesenborgs et al., 2006).

The fitness measures of a genetic algorithm assesses how well a mass distribution satisfies the lens equation, and is therefore used to select the best solution for any given GRALE run. In general GRALE's fitness value can be based on one, two, or more fitness criteria; we chose to use two. The first fitness measure, positional fitness measure, depends upon image positions and the second fitness measure uses the absence of images. For a given mass distribution, the lens equation can be used to project the images from the same source back to the source plane. The positional fitness measure is based on how close observed back-projected images converge to each other. The second fitness measure is based on spurious extra images. In complex lensing systems, additional images could exist that trace back to sources. If the modeler is sure that these extra images do not exist, then the null space of GRALE is defined to be the area of no images in the image plane. The null space is divided in triangles and each triangle is back-projected to the source plane. The second fitness measure of GRALE's fitness is the number of all the triangles that back-projects to the region containing all back-projected images. The fitness value then is proportional to the product of the two fitness measures and used to compare the different iterations of a given run.

Both fitness measures depend upon the choice of modeling images as point-like or extended regions. For the positional fitness measure, the overlap is either fractional between rectangles surrounding extended back-projected images, or measured as distances between back-projected point-like images. For point-like images, GRALE uses the size of the region containing all back-projected images as a length scale. Thus an absolute scale is not used, because this would favor solutions that place the images into smaller source plane regions, and result in overfocusing. For extended images, an absolute scale is also not used, but the average size of the rectangles acts as the length scale which helps avoid overfocusing images, (Liesenborgs et al., 2006). When using extended images for the second fitness measure, the area of existing images is cut out from the null space. Holes are made for regions where one suspects additional images, based on lensing theory. Point-like images do not remove any regions from the null space.

1.4.1 Plummer Spheres

The Plummer sphere is a mass model which, for a Plummer mass M , has density as a function of radius r as

$$\rho_p(r) = \left(\frac{3M}{4\pi r_p} \right) \left(1 + \frac{r^2}{r_p^2} \right)^{-\frac{5}{2}}, \quad (1.27)$$

where r_p is the plummer width (Plummer, 1911). The gravitational potential of a Plummer sphere is

$$\Phi_p(r) = -\frac{GM}{\sqrt{r^2 + r_p^2}}, \quad (1.28)$$

(Liesenborgs, 2010). Using Eq. 1.19, the lensing potential follows as

$$\psi_p(\theta) = \frac{D_{ds}}{D_s D_d} \frac{2GM}{c^2} \ln(\theta^2 + \theta_p^2), \quad (1.29)$$

where $\theta_p = \frac{r_p}{D_d}$. Using Eq. 1.17, the reduced deflection angle caused by a Plummer sphere is

$$\vec{\alpha}(\vec{\theta}) = \frac{D_{ds}}{D_s D_d} \frac{4GM}{c^2} \frac{\vec{\theta}}{\theta^2 + \theta_p^2}. \quad (1.30)$$

Following this, using Eq. 1.18, the convergence from a Plummer sphere is

$$\kappa_p(\vec{\theta}) = \frac{D_{ds}}{D_s D_d} \frac{4GM}{c^2} \left(\frac{\theta_p^2}{(\theta^2 + \theta_p^2)^2} \right). \quad (1.31)$$

Similarly, using Eq. 1.22, the shear tensor for a Plummer sphere is

$$\begin{aligned} \gamma_1(\vec{\theta}) &= \frac{D_{ds}}{D_s D_d} \frac{4GM}{c^2} \left(\frac{\theta_2^2 - \theta_1^2}{(\theta^2 + \theta_p^2)^2} \right), \\ \gamma_2(\vec{\theta}) &= \frac{D_{ds}}{D_s D_d} \frac{4GM}{c^2} \left(\frac{-2\theta_1\theta_2}{(\theta^2 + \theta_p^2)^2} \right). \end{aligned} \quad (1.32)$$

Chapter 2

Grave reconstructions of HFF Clusters

2.1 Grave reconstructions of all HFF clusters

Over the entire duration of the HFF project, four versions of cluster reconstructions were done. Lens modeling teams used pre-HFF data for HFFv1. HFFv2, HFFv3, and HFFv4 used updated data primarily from *HST* observations. A list of lensing observables were required to be submitted for each reconstruction per version. FITS maps were made for the convergence (κ), shear and components ($\gamma, \gamma_1, \gamma_2$), lensing potential (ψ), deflection angles in x and y direction (α_x, α_y) for a source at 'infinity', $\frac{D_{ds}}{D_s} = 1$. In addition, FITS maps were made for magnifications (μ) for sources at $z = 1, 2, 4, 9$. There was a target set of clusters for each submission, but lens modeling teams were free to provide more models than the target.

We, as the GRALE lens modeling team, delivered mass models for all six HFF clusters over the four submission periods. As an example, HFFv1 models using pre-HFF data are shown in Fig. 2.1, for all six HFF clusters. Several submissions had two reconstructions per cluster. Our mass models are available for public use on the 'Frontier Fields Lens Models' webpage of the MAST website under the *L. Williams (PI)* drop-down menu.¹ Readme files are provided that contain the image list used, size of the maps, and other relevant information.

Use of our reconstructions, outside of our team, can be found in McLeod et al. (2016); Bouwens et al. (2017a,b); González et al. (2018); Montes & Trujillo (2018), and other papers. Chapters 3 & 4 use HFFv2 of MACSJ0416 and HFFv3 & HFFv4 of Abell 2744, respectively.

¹ <https://archive.stsci.edu/prepds/frontier/lensmodels/>

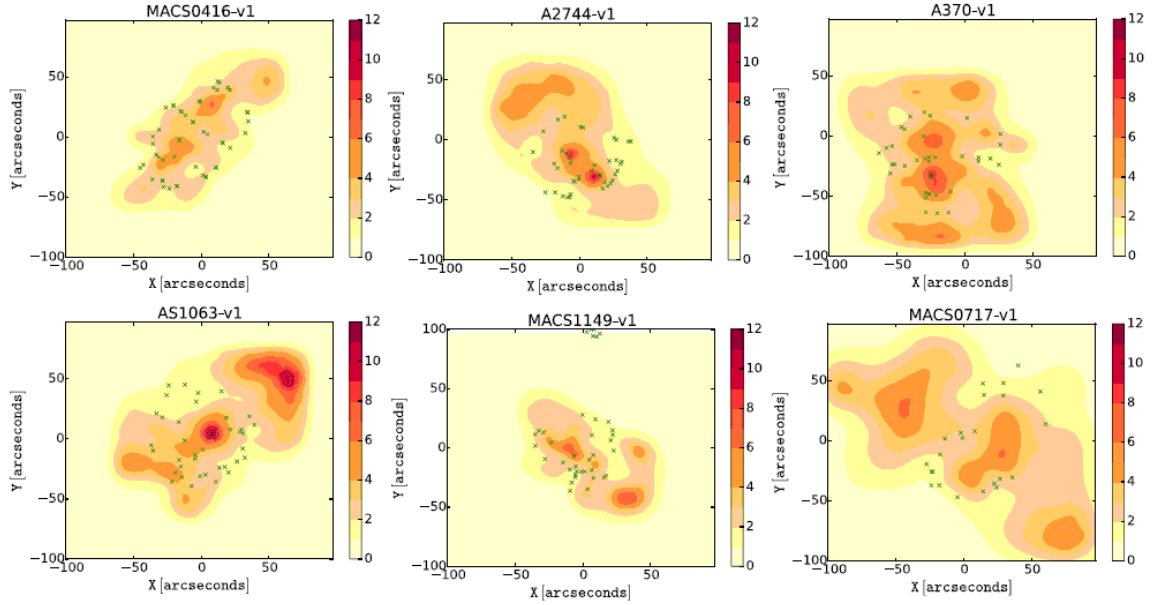


Figure 2.1 HFFv1 GRALE mass reconstructions of the six HFF clusters. Color scale is projected density in units of kg/m^2 . Green dots are multiple images used in each reconstruction. Credit: [Mohammed et al. \(2016\)](#)

Table 2.1 GRALE reconstructions of the six HFF clusters

Abell 2744	HFFv1, HFFv3, HFFv4
Abell 370	HFFv1, HFFv4, HFFv4.1
Abell S1063	HFFv1, HFFv4, HFFv4.1
MACSJ0416	HFFv1, HFFv2, HFFv3, HFFv3.1, HFFv4
MACSJ0717	HFFv1, HFFv4
MACSJ1149	HFFv1, HFFv4

Chapter 3

Testing light-traces-mass in Hubble Frontier Fields Cluster MACS-J0416.1-2403

3.1 MACS-J0416.1-2403

To use clusters as telescopes one must have a detailed and accurate characterization of their optics, or maps of the mass distribution. This chapter is concerned with the mass distribution of one of the HFF clusters, MACSJ0416.1-2403 (hereafter MACSJ0416). It is a massive gravitational lens at a redshift of 0.396, and right ascension 04:16:09, and declination -24:03:58, (Mann & Ebeling, 2012). An *HST* image of the cluster can be seen in Fig. 3.1. The cluster shows features of a recent major merger or pre-merger (Jauzac et al., 2015; Ogrea et al., 2015), like double-peaked X-ray surface brightness (Mann & Ebeling, 2012), elongation, and many sub-structures (Zitrin et al., 2013; Grillo et al., 2015). It has been studied in detail for its mass distribution (Zitrin et al., 2013; Jauzac et al., 2014a,b; Grillo et al., 2015; Diego et al., 2015), magnification maps (Johnson et al., 2014; Richard et al., 2014), and mass power spectrum (Mohammed et al., 2016) using different inversion methods.

This chapter has two goals: (i) to study the mass distribution of the cluster with respect to the light, and (ii) to compare results of two very different methodologies: free-form GRALE with $n_{param} \gg n_{constr}$, and light-traces-mass LENSTOOL, with $n_{param} \lesssim n_{constr}$. To accomplish the first goal in an unbiased way one needs a method that does not include cluster galaxies as input; GRALE satisfies that criterion. One motivation for this is the

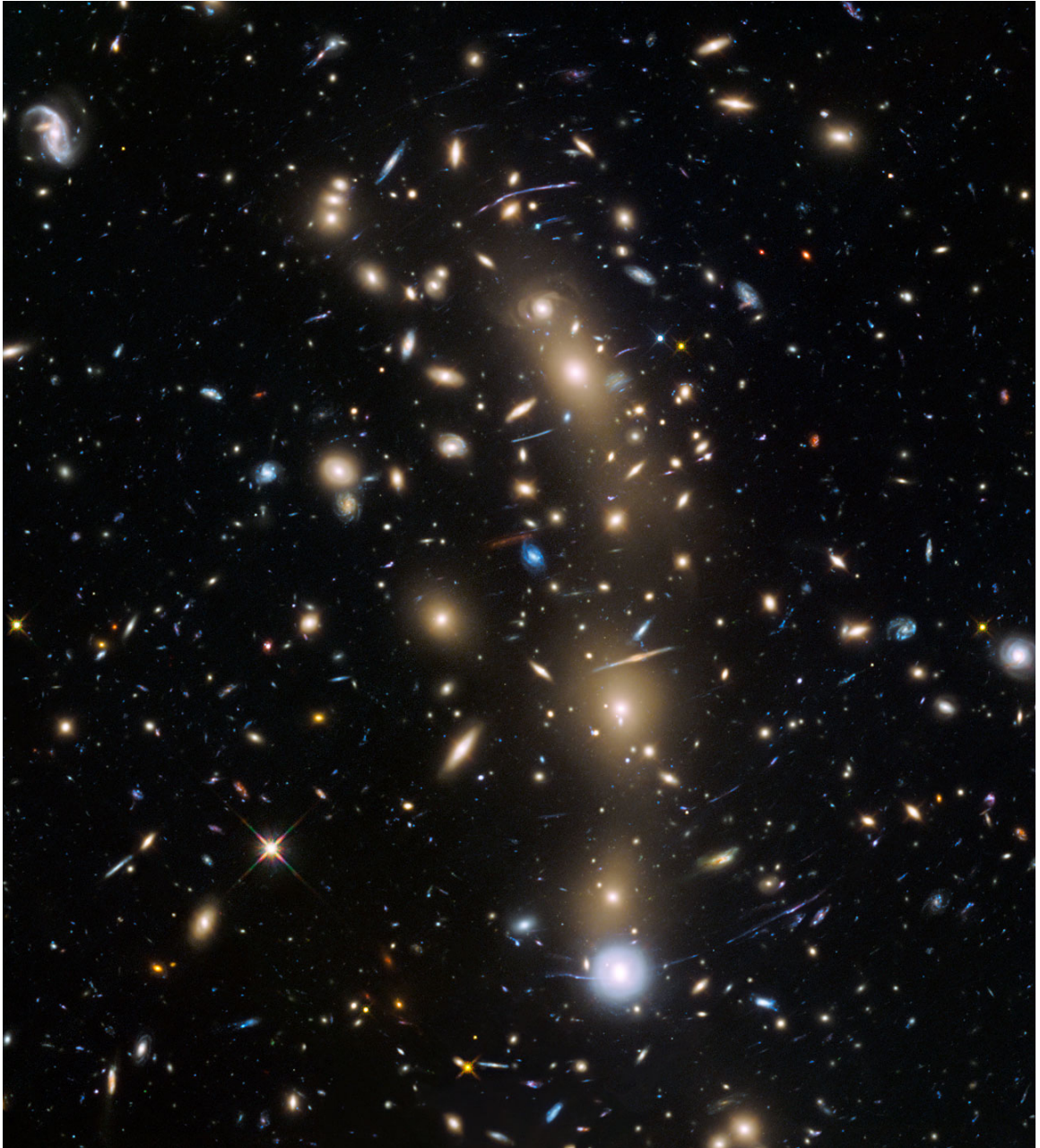


Figure 3.1 HST image of MACSJ0416. Credit: NASA, ESA and the HST Frontier Fields team (STScI).

recent discovery of an offset between a galaxy deep inside the gravitational potential of a massive cluster, ACO 3827 and its dark matter halo (Williams & Saha, 2011; Mohammed et al., 2014; Massey et al., 2015). Because our analysis is confined to the central portions of the cluster we do not expect to find mass-light discrepancies of the kind found by Merten et al. (2011) and Jauzac et al. (2014b). Our second goal has been addressed by some recent papers (Zitrin et al., 2010; Coe et al., 2012), but usually these compare circularly averaged density profiles, which is probably not the most suitable statistic in this case as MACSJ0416 underwent a recent merger. We use a more detailed metric, namely mass-galaxy correlation function.

In Section 3.2 we give a brief summary of the existing mass reconstructions of this cluster. In Section 3.3 we discuss our lens reconstruction method. Section 3.4 presents our results, and in particular discusses light and mass offsets and galaxy-mass correlation function obtained with GRALE, and two inversions with LENSTOOL. In Section 3.5 we summarize our findings for MACSJ0416. We use flat Λ CDM cosmology, with $\Omega_m = 0.27$, and $h = 0.71$, which results in a scale of $5.31 \text{ kpc}''$ at the cluster redshift of $z = 0.396$

3.2 Existing Mass Models of MACSJ0416

Current literature on mass reconstructions of MACSJ0416 have used free-form, hybrid and parametric methods to calculate the associated mass distribution. Zitrin et al. (2013) used two different parametric methods to determine the mass distribution of MACSJ0416. Their first method assigned a PIEMD (pseudo-isothermal elliptical mass distribution) mass profile to every galaxy and smoothed the total resulting mass map with an elliptical Gaussian to obtain a cluster-wide dark matter distribution. The latter was added to the mass due to individual galaxies. The second method used the same PIEMD model for galaxies, and two elliptical NFW halos to describe the dark matter. The authors ran an MCMC algorithm to obtain the solution for both methods. The large number of multiple images in this cluster was attributed to the extreme elongation of MACSJ0416. With their analysis the authors discovered 70 new multiple images from 23 sources.

Johnson et al. (2014) modeled all 6 HFF clusters using pre-HFF data, and analyzed the resulting mass and magnification properties of the reconstructions. They followed the parametric approach by utilizing LENSTOOL to find the best solution for the mass distribution in the clusters. They assigned a PIEMD to each cluster member, and to two cluster-scale components. The best solution was found through an iterative process of running an MCMC algorithm at each step. The final model was computed under image plane optimization,

meaning the differences in the observed and model predicted positions were optimized in the lens plane. The authors report a smaller mass inside the $z = 2$ critical curve than Zitrin et al. (2013) because of different redshifts used in each model.

Richard et al. (2014) adopted a strong- and weak-lensing approach to find the mass distribution of MACSJ0416. They used LENSTOOL with dual pseudo-isothermal elliptical (dPIE) mass profiles for each cluster member, and two cluster-wide mass clumps placed in the regions of high galaxy number density plus a third halo for a lower-redshift galaxy not belonging to the cluster.

Jauzac et al. (2014a) used LENSTOOL, which assigns a dPIE mass profile to cluster galaxies, and cluster wide components. Based on the HFF data the authors identify 51 new multiply imaged systems, for a total of 68, comprising red 194 individual lensed images. Their best model produces lens plane rms of $0.68''$ for 149 images of 57 most securely identified sources.

Grillo et al. (2015) used a parametric method called GLEE. They considered a range of ways of parametrizing the mass distribution in the cluster, and found that the best fit was obtained with a model that has two cored elliptical pseudo-isothermal mass distributions to represent the dark matter and 175 galaxy-size dual pseudo-isothermal mass distributions with the mass-to-light scaling with luminosity. Their model reproduces the positions of 10 image systems, totaling 30 spectroscopically confirmed lensed images very well, with lens plane rms of $0.3''$. Their results are largely in agreement with previous reconstructions of the shape of the mass distribution. A comparison with simulated galaxy clusters with total masses similar to that of MACSJ0416 shows that the former contain considerably less mass in subhalos in their cores relative to MACSJ0416.

Diego et al. (2015) used a hybrid approach to reconstruct the mass distribution of MACSJ0416. Three separate mass models were made for the galaxy component of the lens, two following the light traces mass assumption and the third linking every galaxy to a circularly symmetric NFW distribution. The rest of the mass distribution was modeled by a free-form method. These mass models showed a bimodal mass distribution, similar to the X-ray emission distribution, except for small offsets in the two peaks. Collisional effects such as dynamical friction are believed to be the reason behind the offsets between X-ray and dark matter distributions. In addition, a flat mass profile was found on medium distance scales surrounding the two peaks of the mass distribution, likely because of tidal forces, projection effects, or possibly self interacting dark matter. The authors find that overall light traces mass in MACSJ0416.

Table 3.1 Previous MACS0416 mass models with type of data used and number of multiple images.

Author	Type of Data	Num. of multiple images
Zitrin et al. (2013) LTM-Gauss	pre-HFF	34
Zitrin et al. (2013) NFW	pre-HFF	34
Johnson et al. (2014)	pre-HFF	34
Richard et al. (2014)	pre-HFF	47
Jauzac et al. (2014a)	HFF	149
Grillo et al. (2015)	CLASH	30
Diego et al. (2015)	CLASH	96

Published mass reconstructions of MACSJ0416 are summarized in Table 2.1. Besides the Zitrin et al. (2013) LTM-Gauss method, every previous parametric method used two cluster-scale haloes. All previous reconstructions made use of the galaxy light in MACSJ0416 in some form when calculating the mass distribution. We go about the reconstruction process differently, and use only the positions of the lensed images as input. Thus, light is not assumed to trace mass in our reconstruction processes, and our results represent a completely independent way of modeling MACSJ0416 and testing if light follows mass in clusters.

3.3 Gracle Setup

We generated 30 GRALE reconstructions, each one using nine successive lensing grid refinements. We used 149 secure images as outlined in Jauzac et al. (2014a) and updated redshifts from Grillo et al. (2015). For each grid the number of Plummer distributions was chosen at random from a selected range. The first lensing grid’s range was 300-400 and the last, ninth lensing grid’s range was 1700-1800. Each subsequent grid had a greater density of Plummer spheres. In addition, the center coordinates and size of each grid was allowed to fluctuate by 5'' and 10'' respectively to eliminate the imprint of a fixed grid on the solution. Finally, for each run the best mass map was selected depending upon the fitness value described above. Each reconstruction’s results are somewhat different because the random seed used by GRALE to initialize a run enables it to explore different regions of the large dimensional model parameter space. To reduce the random variations and to enhance the common features in mass maps of different runs, the runs—30 in our case—are averaged to produce one final mass map, which is also a solution, as discussed in Mohammed et al.

(2014).

3.4 Results

The average map of the 30 individual GRALE reconstructions is shown in Fig. 3.2; this map is the basis of our analysis. The blue lines are the mass density contours and the red circles indicate images. There are 20 contour lines linearly spaced from 0.03827 g/cm^2 up to 0.76531 g/cm^2 . Using the 30 individual maps we can calculate the fractional uncertainty defined at every location in the lens plane as the ratio of the root-mean-square deviation between the maps' κ values and the average κ of all the maps. (κ is the projected surface mass density in units of critical density for lensing). The fractional uncertainty highlights areas in the mass distribution that contain small and large uncertainty. As seen in Fig. 3.3, there are some small areas within the central parts of the galaxy cluster that contain large fractional uncertainty, 30-40% (where contour lines are green and the density of lines is greater), however most of the galaxy cluster is minimal in fractional uncertainty, usually below 15% and in some regions below 5% (where contours are thin and the density of lines is lower), because GRALE is very well constrained by the images in this region. Large fractional uncertainty values can be seen outside the central elongated region of the cluster where GRALE does not have many constraints.

GRALE, or any other lens reconstruction method that does not explicitly place mass at the location of visible galaxies as part of its input is the right tool for investigating how well mass follows light on the scale of galaxies in the cluster. No other published lensing inversion of MACSJ0416 is form-free in this sense. Here, we investigate this using two approaches, described in the next subsections.

3.4.1 Mass Contours and Local Mass Peak Offsets

One way to determine if light traces mass is to analyze the projected mass contours, shown in Fig. 3.2, and their relation to the galaxies.

It is apparent that the overall mass distribution of the cluster, including its elongation is well reproduced. GRALE finds two prominent cluster-wide mass clumps; these correspond to the two parametric dark matter components used in most of the models of MACSJ0416 described in Section 3.2. Visual inspection shows that close to the center of the cluster, where the map is best constrained the mass density contours around galaxies encircle the galaxies indicating that GRALE places mass concentration at those locations, even though galaxies are not part of the input. Towards the edges of the cluster, where the mass is least

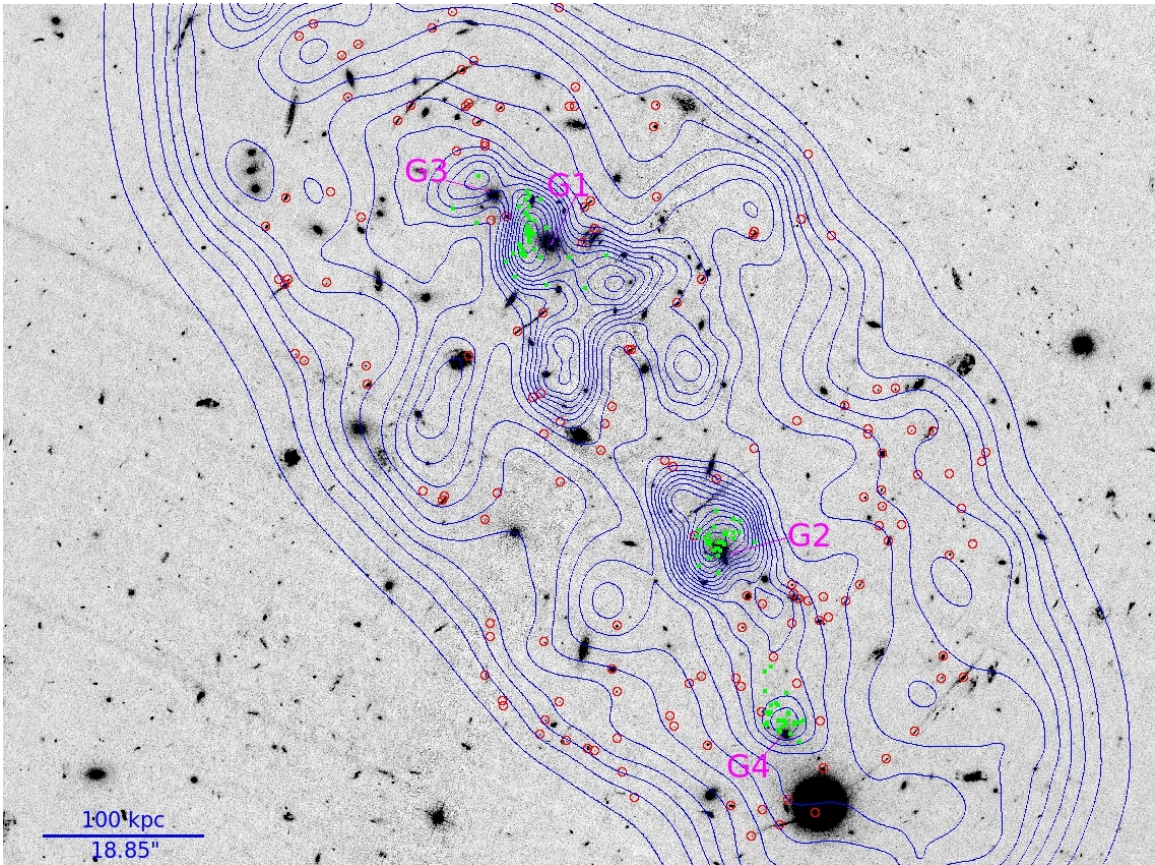


Figure 3.2 Mass contours of averaged mass map of MACSJ0416 red overlaid on a HST F435W image. The blue lines represent the mass density contours and the red circles are images. There are 20 mass contour levels linearly spaced from 0.03827 g/cm^2 up to 0.76531 g/cm^2 . The green dots represent local mass peaks around the 4 central ridge galaxies, in 30 individual mass reconstructions. These galaxies are labeled G1-G4, with G1 appearing the brightest.

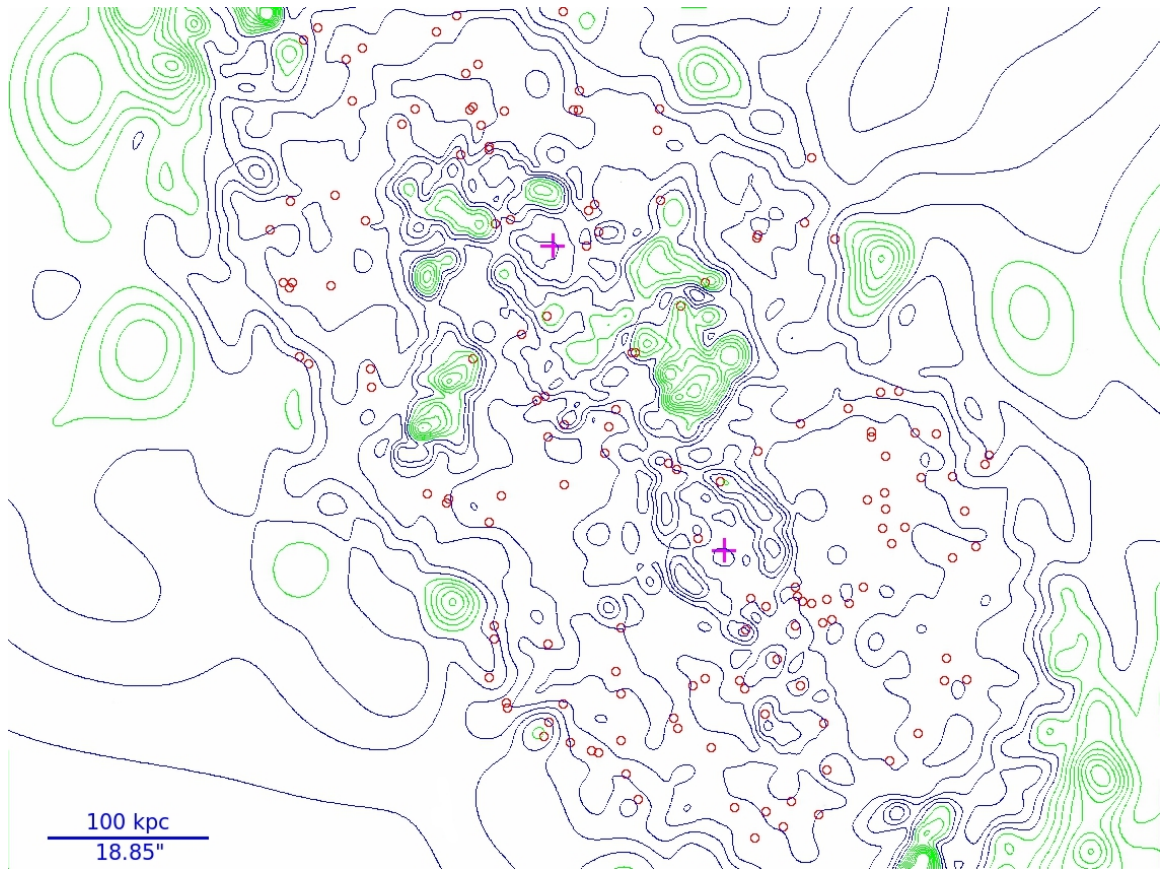


Figure 3.3 Contours of fractional uncertainty in mass density of MACSJ0416. The contours are separated into two groups distinguishable by their colors. The six blue contour lines range from 3.3% to 19.8% in fractional mass density uncertainty, and the seven green lines range from 23.1% to 49.5%. Images are highlighted by red circles and the two BCGs are marked as magenta crosses.

constrained, some contour lines go through galaxies, indicating that these galaxies are not ‘detected’ by GRALE.

One of our goals is to determine how well mass follows light in the immediate vicinity of galaxies. These latter galaxies that GRALE does not detect cannot be used for the purpose, but the former ones can. There are four such galaxies along the central ridge line of MACSJ0416; they are marked in Fig. 3.2 and have magenta labels G1-G4. These regions also correspond to low fractional uncertainties, $\lesssim 10\%$, in reconstructed mass.

A closer inspection of the mass contours around these four galaxies reveals that the peaks of the mass distribution are displaced from the closest galaxy cluster member. To find out if the displacement is statistically significant we can look at the scatter of the positions of the local density peaks in the 30 individual mass maps. The green dots in Fig. 3.2 mark the highest single mass pixel in each of the 30 reconstructions, in circular regions of radius $8''$ around the four galaxies. Even though the galaxy positions are not centered on the corresponding cloud of 30 mass peaks, they are also not significantly offset from that distribution. Table 3.2 shows the distance in arcseconds between galaxy and average position of the 30 mass peaks. The significance can be defined as the ratio between the offset and root-mean-square dispersion. The last column of Table 3.2 shows none of the galaxies to be significantly offset from the mass peaks. We conclude that there is no compelling evidence that the mass in the immediate vicinity of the central galaxies does not trace the light. This is in contrast to the case of galaxy N1 in ACO 3827 (Williams & Saha, 2011; Mohammed et al., 2014; Massey et al., 2015), where the displacement between the galaxy and the nearest mass peak is $0.89_{-0.27}^{+0.26}''$, or $1.62_{-0.49}^{+0.47}$ kpc.

Table 3.2 Offsets between galaxies G1-G4 and 30 mass models peaks in arcseconds. The third column is the root-mean-square dispersion between the galaxies and mass peaks. The last column is the significance, ratio between the distance and root-mean-square.

Galaxy	Dist. ($''$)	RMS ($''$)	$\frac{\text{Dist.}}{\text{RMS}}$
G1	2.77	3.62	0.77
G2	0.94	2.16	0.43
G3	5.94	3.62	1.64
G4	2.20	2.35	0.94

The width of the distribution of the 30 local mass peaks from individual reconstructions, i.e. our uncertainty, is $\sim 5''$, and represents the smallest offset we could have detected, if these were present. Given that the galaxy-mass offset in ACO 3827, $\sim 0.9''$, yields dark matter self-interaction cross section that is approximately the same as the upper limit

from other studies (Clowe et al., 2006; Randall et al., 2008; Kahlhoefer et al., 2014, 2015), means that the level of uncertainty in MACSJ0416 will not allow a more stringent upper limit on dark matter self-interaction cross section. Although the total number of images in MACSJ0416 is high, ≈ 150 , it appears that their distribution, for example the proximity to the four galaxies, or the accuracy of the source redshifts, are not adequate to constrain the offsets at a level comparable to those seen in ACO 3827. The role of image (or image knot) number density in accurately constraining mass maps was discussed in Liesenborgs et al. (2008). The authors showed that the monopole degeneracy, a way to redistribute mass between images by adding circularly symmetric density distributions with zero total mass, does not change image positions, and is largely responsible for uncertainty in the mass determination. The prevalence of monopole degeneracy will depend on whether the distribution of images allows adding such circular regions. It is possible that this is easier to do near the galaxies G1-G4 in MACSJ0416 than in ACO 3827. It is possible that in other HFF clusters the configuration of the images is more fortuitous for the detection of possible offsets.

3.4.2 Mass-Galaxy Correlation Function: Grale

A further measure of how well mass follows light is provided by the correlation function, $\xi(\theta)$ between galaxies and the average reconstructed mass map. The projected galaxy-mass correlation function describes how galaxies and mass are clustered, as a function of separation, θ , on the sky. It is defined through conditional probability, dP of finding a galaxy in a volume dV , a distance θ away from another galaxy, $dP = n(1 + \xi)dV$, where n is the average number density of galaxies. It typically decreases with separation, after attaining the largest amplitude at zero. We use the estimator $\xi(\theta) = \frac{D_m D_g}{\langle D_m R_g \rangle} - 1$, where $D_m D_g$ represents the number of mass pixel-galaxy pairs, and $\langle D_m R_g \rangle$ is the average number of pairs of 100 trials, where the positions of the galaxies have been randomized.

The galaxy-mass correlation function between the galaxies in the Subaru R-band catalog in MACSJ0416 and the average mass map is shown in Fig. 3.4. It was computed using a bin size of $0.52''$ within a region of area 5903.52 squared arcseconds and enclosing galaxies and images along the cluster's line of elongation. This is the line extending through the two brightest cluster galaxies of the cluster. We chose Subaru galaxies over HST galaxies because Subaru catalog contains magnitudes for all HST galaxies, including those that are too bright for HST. Furthermore, Subaru filters we use are closely matched by HST filters; specifically, galaxy magnitudes in Subaru Z (R) band are tightly correlated with HST F814W (F606W) magnitudes. Since Subaru is a ground-based telescope, the light profiles of the brightest

galaxies are extended, and may block fainter galaxies. To reduce this bias, we masked the 10 brightest galaxies in the Subaru R-band with a circle of radius $8''$ before calculating the correlation functions. Fig. 3.4 shows $\xi(\theta)$ for several galaxy magnitude cuts; the number of galaxies in each cut is indicated in the figure.

If galaxies traced the underlying mass distribution according to the standard biasing scheme one would expect that the brightest galaxies would show the strongest clustering with the mass, and as the galaxy magnitude limit is pushed towards lower fluxes, the amplitude of the correlation function would decrease due to two reasons: fainter galaxies contain less mass, and are thus biased towards less mass. This is indeed what is seen. Because GRALE input does not include any information about the galaxies, the trend of brighter galaxies being more biased towards mass is an important confirmation of the standard biasing scenario.

Fig. 3.4 also shows that at very small separations, $\lesssim 2''$, the correlation function decreases, instead of increasing as separation approaches zero. Taken at face value, this would be indicative of an offset between dark and light matter in cluster galaxies. However, the uncertainties in ξ , which are approximately 0.025, are too large to make that conclusion. This behaviour at small separations and its marginal statistical significance was already seen in Section 3.4.1.

While it is safe to assume that bright galaxies are mostly cluster members, the same cannot be said of fainter ones. One way to find the apparent magnitude below which most galaxies are background to the cluster is to use lensing magnification bias. Behind a galaxy cluster lensed galaxies are made brighter than unlensed ones at the same redshifts and the area behind the lens is simultaneously stretched by the same magnification factor. To predict the net effect of this bias we can look at the differential galaxy counts as a function of apparent magnitude. Fig. 3.5 shows these counts based on the entire Subaru field; using just the galaxies in the direction of the cluster would produce very noisy counts. Magnification bias decreases galaxy counts at magnitudes where the slope of the counts is shallow, and increases them at magnitudes where the slope is steep. When the slope is equal to one, $d\log(n[m])/d\log(f) = 1$, there is no magnification bias because the flux magnification and area dilution cancel each other out. In principle, one should look at the unlensed counts slope for this purpose, which are unobservable, but in the case of relatively shallow counts, the lensed observed counts provide a reasonable approximation.

Because at magnitudes where $d\log(n[m])/d\log(f) < 1$ area dilution wins over flux magnification, magnification bias predicts anti-correlation between cluster mass and background galaxies. According to Fig. 3.5, $d\log(n[m])/d\log(f)$ becomes shallower than 1 below

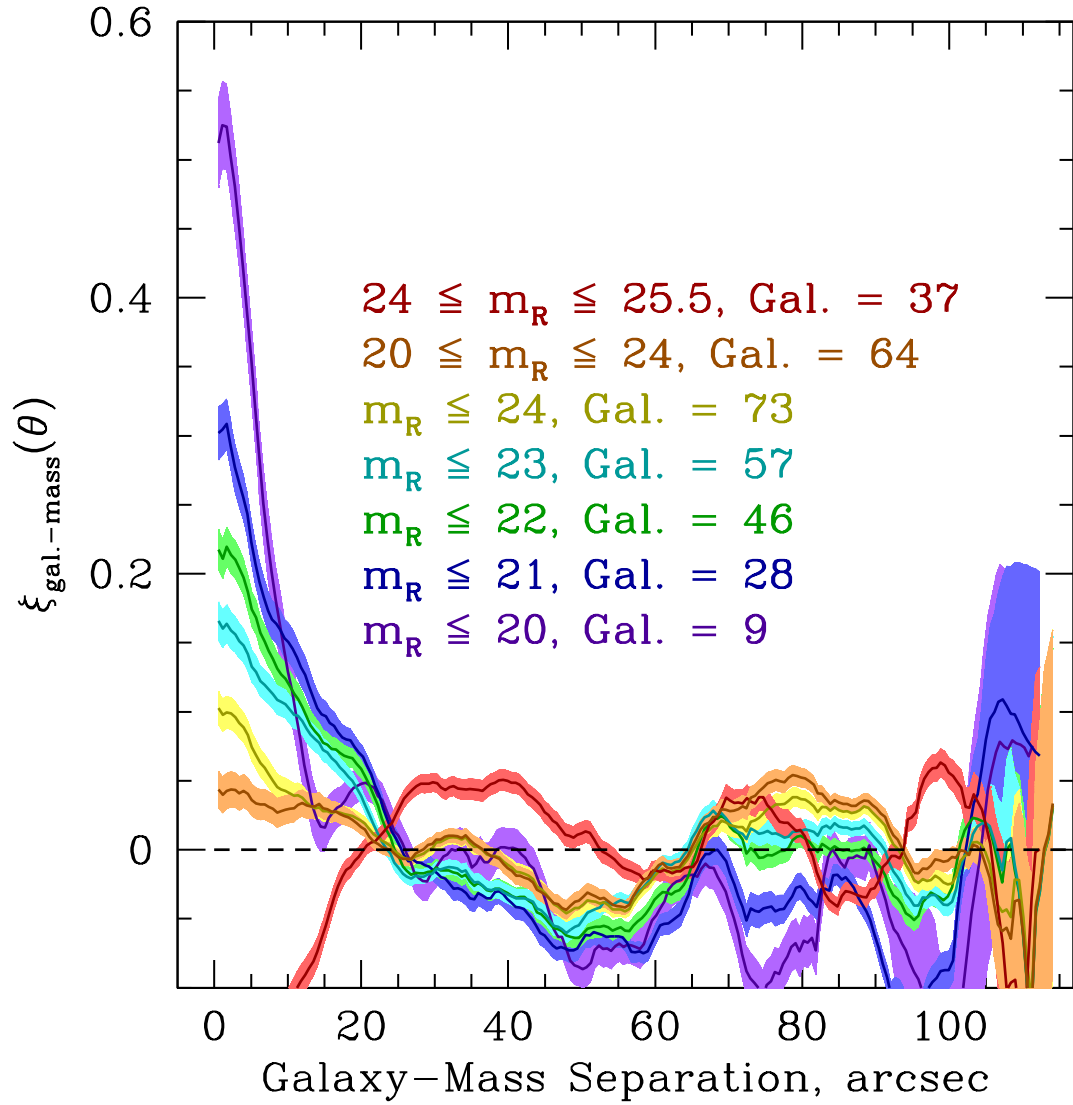


Figure 3.4 Normalized galaxy-mass cross-correlation function for Subaru R-band at multiple magnitude cuts. The mass map is the average of 30 individual GRALE reconstructions. Rms dispersion between the 100 realizations of $D_m R_g$ is approximately 0.025 for all magnitude ranges. Shaded regions indicate 1σ error bars.

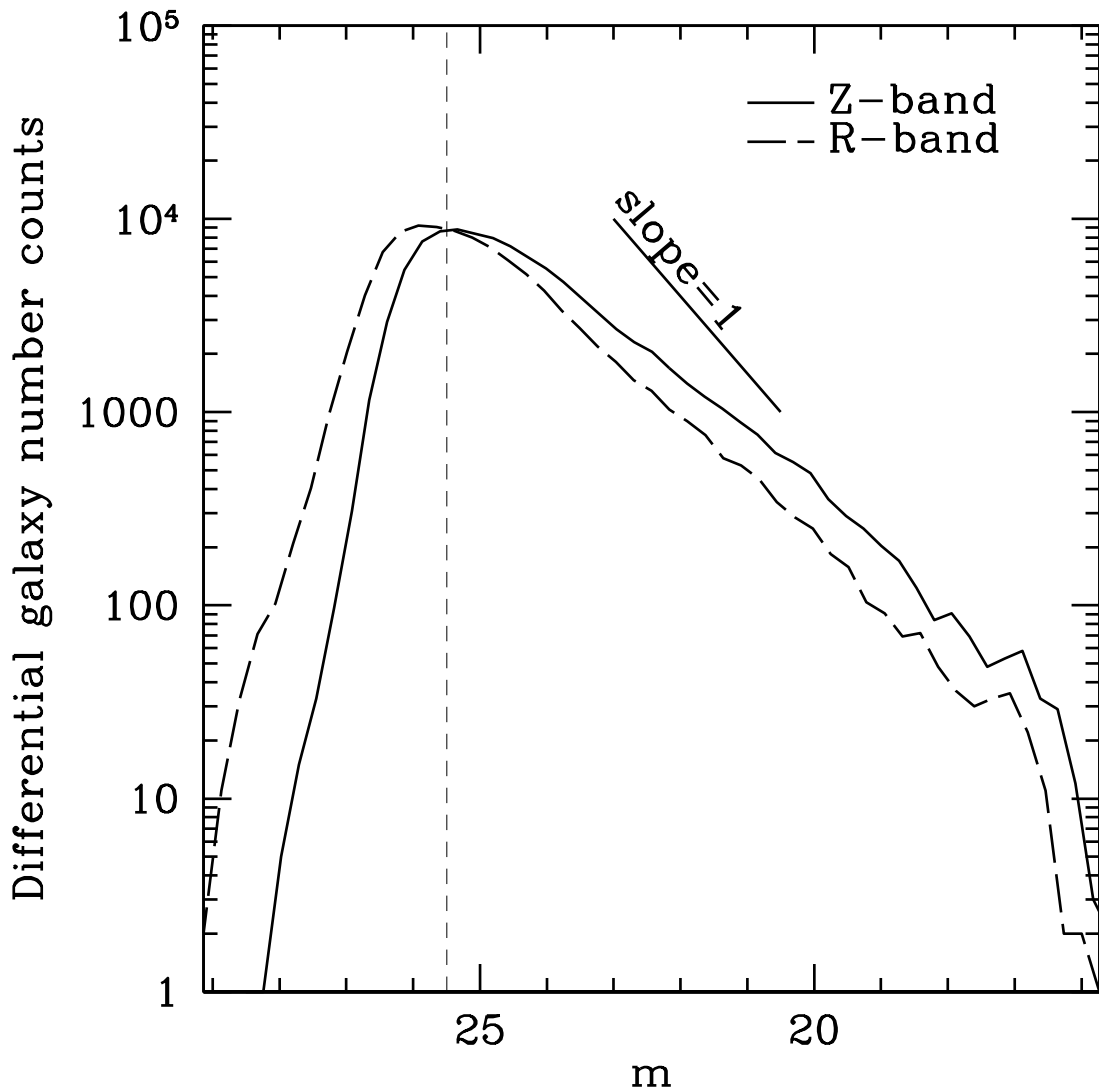


Figure 3.5 Differential number counts of galaxies over the entire Subaru field, not just the galaxies behind the cluster. The vertical dashed line marks the magnitude below which counts are incomplete; we did not include these galaxies in any of the analysis. The marked line, $d \log(n[m])/d \log(f) = 1$, is provided for comparison to the two bands.

$m \approx 20$, for both R and Z magnitudes. We select two magnitude cuts, $20 \leq m \leq 24$ and $24 \leq m \leq 25.5$; we did not use galaxies fainter than 25.5 because beyond this magnitude counts suffer significantly from incompleteness.

For the $20 \leq m \leq 24$ cut we expect modest anti-correlation for the R-band, and somewhat larger anti-correlation for the Z-band, because Z-band counts are shallower than those in R-band. The same masking procedure was applied to the Z-band for computing the correlation function. The computed correlation functions for both bands are shown in violet in the lower middle left and right panels of Fig. 3.6. Indeed, the Z-band galaxies show less correlation than the R-band galaxies. However, neither the R-band selected galaxies nor the Z-band selected galaxies show an anti-correlation between GRALE cluster mass and galaxies. This might indicate that some of the galaxies in this magnitude range are cluster members, and so the total correlation function signal consists of a superposition of mass clustering with the cluster member galaxies, and magnification bias resulting from the cluster mass lensing background galaxies.

At fainter galaxy magnitudes, $24 \leq m \leq 25.5$, we expect that most, if not all galaxies are background to the cluster, and so magnification bias will be the only effect. Consistent with this expectation we find a strong anti-correlation between cluster mass and cluster galaxies for both Subaru magnitude bands (we show only R band results here). Thus, different magnitude cuts show features that imply that magnification bias exists in MACSJ0416, and so many of the fainter galaxies are significantly background to the cluster. Magnification bias is sometimes used to aid mass reconstruction in clusters (Umetsu & Broadhurst, 2008; Umetsu et al., 2016).

We note that the (anti-)correlations extend to about $20''$, or 100 kpc at the redshift of the cluster (Fig. 3.4), which is roughly the typical separation between bright, $m \lesssim 20$ galaxies, and considerably smaller than the size of the cluster, $120'' \times 50''$.

3.4.3 Mass-Galaxy Correlation Function: Grale vs. Lenstool

A number of metrics can be used to compare mass reconstructions from different lens inversion methods. One can look at the differences, or fractional differences between two κ maps on the x, y plane, however, summarising that information in a concise way is difficult. One can also look at the circularly averaged radial density profiles of the different maps, however, this entails a lot of averaging, which hides many potentially interesting differences. We use the correlation function, which is similar to circular averaging, but is done around each galaxy, instead of just the center of the cluster. It is a good compromise between too much and too little detail.

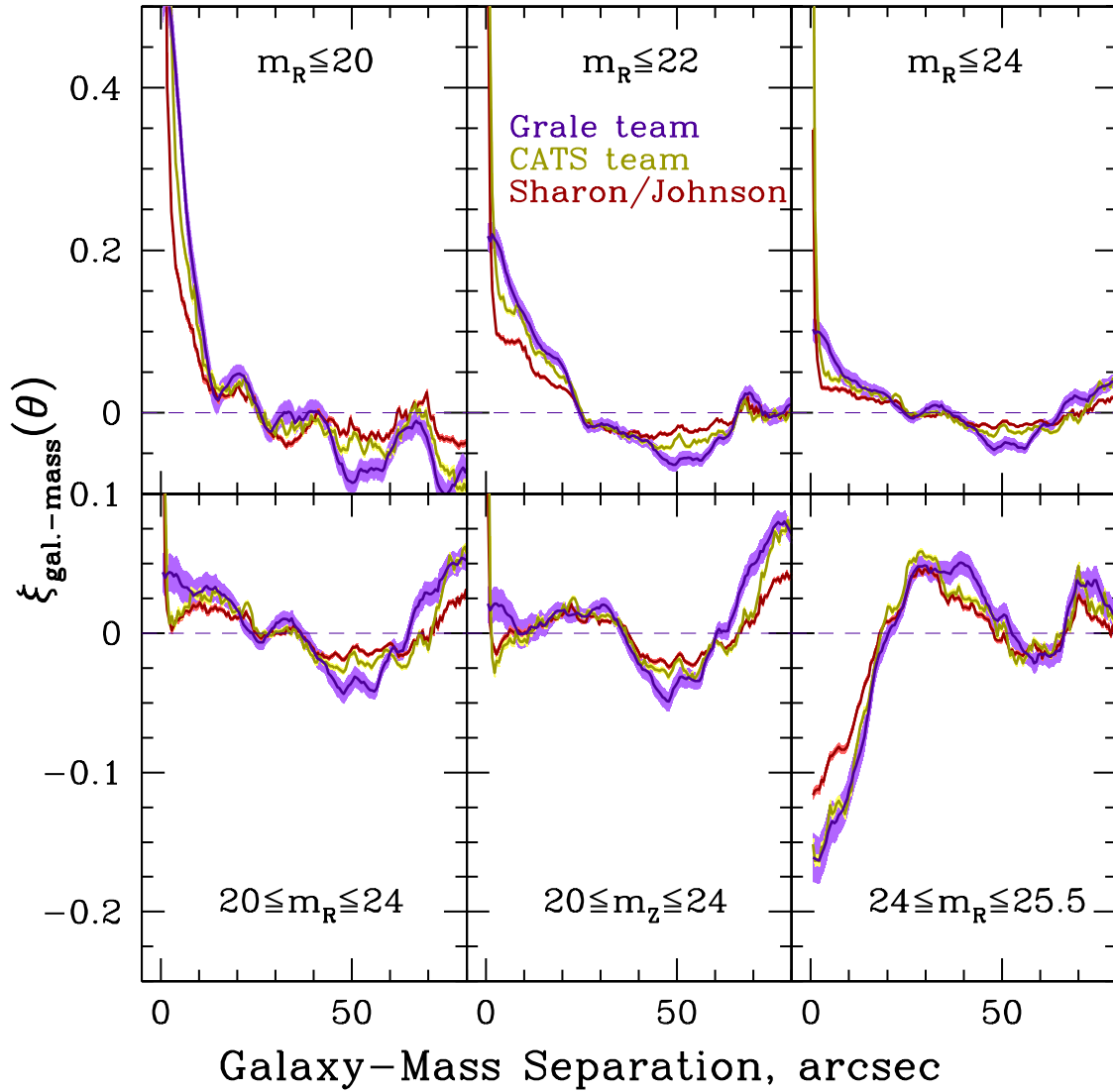


Figure 3.6 Galaxy-mass cross-correlation functions for five Subaru R-band and one Z-band magnitude cut. Three mass maps are used: from the GRALE team (violet), CATS team (gold), and Sharon/Johnson (red). Shaded regions indicate 1σ error bars.

We compare GRALE results to those of two groups that use different implementations of LENSTOOL, CATS team and Sharon/Johnson team, which are presented in Jauzac et al. (2014a) and Johnson et al. (2014), respectively, and are available for download on the HST MAST website. In this work, we limit our comparison to reconstructions based on LENSTOOL only, because GRALE and LENSTOOL are at the opposite ends of the spectrum of assumptions going into lens inversion methods. We leave a broader comparison to a later work. The CATS reconstruction is based on the HFF strong and weak lensing data, and Sharon/Johnson reconstruction uses pre-HFF strong lensing data. Both assume flat Λ CDM cosmology, with $\Omega_m = 0.3$, and $h = 0.7$. This is different from our assumed cosmology, but the difference results in negligible deviations of length scales, $\sim 0.5\%$.

Figure 3.6 plots mass-galaxy correlation function for six different galaxy magnitude cuts. All but the bottom middle panel use Subaru R-band to select galaxies; the bottom middle panel uses Z-band. The magnitude cuts in the six panels are $m_R \leq 20$, $m_R \leq 22$, $m_R \leq 24$, $20 \leq m_R \leq 24$, $20 \leq m_Z \leq 24$, and $24 \leq m_R \leq 25.5$. A cursory look at these reveals that all three teams recover very similar clustering properties. The fact that parametric and free-form methods yield very similar results is encouraging, and leads to two conclusions, (a) strong priors about mass following light are not required to recover mass distribution in clusters with very many lensed images, (b) light follows mass quite well in this merging cluster.

Though GRALE and the two implementations of LENSTOOL agree overall quite well, there are notable differences between the three.

CATS and Sharon/Johnson correlation functions have a sharp spike near zero separations. This tight correlation is the result of LENSTOOL placing mass at the locations of the visible galaxies. The central spike in LENSTOOL models can be also seen in the projected mass power spectrum of the cluster studied by Mohammed et al. (2016): see the left panel of their Fig. 9, where the fluctuation power at large k does not fall as fast as GRALE's. GRALE, which is blind to galaxies, still detects galaxies as gauged by this metric, but does not associate as much mass with them due to a combination of two reasons, (i) the positions of lensed images do not require it, and (ii) GRALE does not have sufficient spatial resolution.

Aside from the central spike, the correlation functions of the two implementations of LENSTOOL, CATS and Sharon/Johnson, disagree with each other at the same level as they disagree with GRALE. In fact, in the range $\theta = 2''-20''$ CATS and GRALE are closer to each other than CATS and Sharon/Johnson. This behaviour is probably the result of the data sets used: GRALE and CATS use HFF, while Sharon/Johnson use pre-HFF.

Given that CATS and GRALE teams use the same strong lensing data sets, the difference

between these two should be entirely due to the differences in the reconstruction method. A closer examination shows that at separations $2''-10''$ and magnitude cuts above $m_R = 24$, CATS team correlation functions' amplitude is below that of GRALE—one can say it shows a dip—and below a smooth extrapolation of $\xi(\theta)$ from larger separations. On these scales GRALE's $\xi(\theta)$ looks smooth and rises monotonically in that region. In other words, compared to GRALE, CATS LENSTOOL mass maps show a steeper decline in correlation function with increasing separation. This is likely a consequence of how LENSTOOL builds its mass maps as a superposition of large, smooth dark matter component(s) and mass spikes due to galaxies. There is no intermediate mass component that could bridge the gap and introduce more mass on these length scales around galaxies.

GRALE's $\xi(\theta)$ gentler decline with θ on scales $2''-10''$ or $10 - 50$ kpc may suggest that there is more galaxy-mass correlation on these scales, i.e. that galaxies, and especially those in the magnitude range $22 \lesssim m_R \lesssim 24$, are more biased traces of mass in clusters than LENSTOOL assumes. In this context it is interesting to recall a recent discovery of nearly a thousand low surface brightness galaxies with $1 \text{ kpc} \lesssim R_e \lesssim 3 \text{ kpc}$ in the center of Coma cluster (Koda et al., 2015). Since these galaxies are old and evolved, they likely existed in clusters at higher redshifts, comparable to those of HFF clusters. Though faint and likely low mass, they still outnumber cluster members. These are not part of LENSTOOL input, and if they cluster with brighter galaxies, they could contribute to higher correlation amplitude on scales of tens of kpc.

In general, the somewhat different galaxy-mass clustering amplitudes found by the three groups imply distinct models of how mass is distributed in clusters, and have different implications for the cluster structure and evolution. For example, a larger galaxy-mass clustering amplitude, such as obtained by LENSTOOL vs GRALE, may imply that galaxies form at much higher density peaks of the matter distribution, or that only the most compact galaxies can survive in cluster centers. Hydrodynamic numerical simulations could help to further determine the implications of the degree of biasing within clusters.

3.5 Conclusions

We carried out a lens inversion of MACSJ0416 using GRALE, a free-form genetic algorithm based method. The only inputs were 149 lensed images, identified by Jauzac et al. (2014a) based on HFF data. First, we summarize our results on the comparison between GRALE and the two LENSTOOL mass reconstructions of this massive, merging $z \sim 0.4$ cluster. Because the true mass distribution in galaxy clusters is unknowable, it is important to critically

compare the commonly used estimators. Our conclusions based on these two very different methodologies are:

- Though the mass maps of GRALE and LENSTOOL reconstructions look somewhat different in detail, GRALE and LENSTOOL (specifically, CATS and Sharon/Johnson teams) recover very similar statistics of the mass-galaxy correlation.
- The most striking, but expected difference is that LENSTOOL’s galaxy-mass correlations show a pronounced spike near zero separation. This is because LENSTOOL places a lot of mass at the locations of galaxies as part of its input, whereas GRALE does not.
- Another notable difference is that on scales of $2''$ – $10''$, or tens of kpc, GRALE’s correlation function falls less steeply than LENSTOOL’s. It is possible that the lensing constraints are compatible with both the steeper and the shallower decline. However, it is also possible that the mass distribution is more extended on these scales around galaxies, as GRALE suggests, due to the presence of many hundreds of low surface brightness galaxies of the kind recently detected in Coma (Koda et al., 2015).

The fact that two very different methodologies—GRALE and LENSTOOL—give similar results leads us to conclude that when lensed image number is around 100 or more, the images alone are sufficient to recover the mass distribution in clusters very well. Strong priors on galaxies are not needed.

Our conclusions regarding the mass vs. light distribution in MACSJ0416 are:

- Even with the high number of images present in MACSJ0416, no significant mass-light offsets are found between the four central galaxies and the nearest mass peaks, in contrast to ACO 3827. Our uncertainties are $\sim 5''$, larger than $0.9''$ offset observed in ACO 3827. It is possible that other HFF clusters have a more fortuitous image configuration and hence smaller uncertainties around the bright cluster galaxies.
- Overall, on scales larger than a few arcseconds, light traces mass, as reconstructed by GRALE, in the merging cluster MACSJ0416 quite well, as measured by the galaxy-mass correlation function. This is the only analysis of this merging cluster that does not use any information about the visible light, hence the conclusion that light follows mass is not trivial.
- The faintest galaxies in the direction of MACSJ0416 are anti-correlated with the cluster mass, implying the presence of the lensing magnification bias

Chapter 4

Two free-form lens reconstruction of Hubble Frontier Fields Cluster Abell 2744

4.1 Abell 2744

The first goal of this chapter is to address systematic uncertainties, for a single lens reconstruction method, free-form GRALE, applied to the multiple image, strong lensing data. We evaluate the reliability of GRALE-derived uncertainties by comparing two reconstructions of the same HFF cluster, Abell 2744, that differ in input image properties, as well as certain code parameters. Our first reconstruction described in this paper, HFFv3, was done for the second year of the HFF project, using an image list with a combination of spectroscopic and photometric redshifts from [Richard et al. \(2014\)](#); [Johnson et al. \(2014\)](#); [Wang et al. \(2015\)](#); [Jauzac et al. \(2015\)](#). The following year, our second reconstruction, HFFv4, was completed with an all spectroscopic image list from [Mahler et al. \(2018\)](#).

Since GRALE is fully free-form, and uses no information pertaining to the distribution of light from the cluster or its galaxies, it serves as an excellent method to accomplish our second goal, to investigate if there are any significant unexpected differences between the reconstructed mass and the observed light distributions. Following the previous chapter and work on a different HFF cluster, MACSJ0416, we use mass-light centroid offsets, and galaxy-mass correlation function as our metrics to accomplish the second goal.

Abell 2744 is a massive galaxy cluster with a right ascension of $00^{\text{h}}:14^{\text{m}}:19^{\text{s}}$ and declination of $-30^{\circ}:22':15''$, and a redshift of 0.308 ([Mann & Ebeling, 2012](#)). The cluster can

be seen in Fig. 4.1. The cluster is in an ongoing merger, first evidenced from a radio halo (Giovannini et al., 1999; Govoni et al., 2001a,b). The merger scenarios for Abell 2744 have been a popular topic of debate for the last 20 years (Owers et al., 2011; Merten et al., 2011; Medezinski et al., 2016; Jauzac et al., 2016). Inversion methods have utilized many multiply-imaged systems (Zitrin et al., 2014; Johnson et al., 2014; Ishigaki et al., 2015; Jauzac et al., 2015; Kawamata et al., 2016, 2018; Mahler et al., 2018), cluster-wide weak lensing distortions (Cypriano et al., 2004; Medezinski et al., 2016), or both (Merten et al., 2011; Lam et al., 2014; Wang et al., 2015; Jauzac et al., 2016) to study the mass distribution at different scales.

In Section 4.2 we give an overview of the previous mass models of Abell 2744. In Sec. 4.3 we outline the inputs for our lens reconstruction method. Section 4.4 presents the comparison between our two reconstructions. In Section 4.5 we discuss the influence of mass outside the region of images on our results, and in Section 4.6 we examine how well light traces mass in this cluster. Finally, Section 4.7 presents a summary of our findings. We use a flat Λ CDM cosmology, with $\Omega_m = 0.3$ and $h = 0.7$ which results in a scale of $4.536 \text{ kpc}''$ at the cluster redshift of $z = 0.308$.

4.2 Existing Mass Models of Abell 2744

The first lensing mass estimates of Abell 2744 (also known as AC 118) were published by Smail et al. (1997) and Allen (1998). Smail et al. (1997) constructed a weak lensing shear map for Abell 2744 from a catalogue of faint background objects built from HST data. Using this shear map and the singular isothermal sphere (SIS) profile to model the cluster, the cluster mass around the central core region, $r < 400 \text{ kpc}$, was calculated to be $M = 1.85 \pm 0.32 \cdot 10^{14} h^{-1} M_\odot$. The authors note that the configuration of the shear map reveals that the cluster contains two prominent mass clumps. Allen (1998) used strong lensing data from previous literature to calculate the mass of Abell 2744. Using an arc at $z = 1.00$, the mass of a circular distribution was calculated to be $M = 5.68 \cdot 10^{13} h^{-1} M_\odot$.

Cypriano et al. (2004) reconstructed the mass of Abell 2744, and 23 other clusters, using the LENSENT software for weak lensing. Catalogues of galaxies within each cluster field were built, and galaxy ellipticity parameters were extracted using a Bayesian technique. Background galaxies were chosen based on their location behind the cluster and light properties, leading to accurate shape measurements. The total mass distribution was calculated using LENSENT, with a maximum entropy method, starting from the reduced shear field. After smoothing, two mass models, SIS and singular isothermal ellipsoid (SIE), were used



Figure 4.1 HST image of Abell 2744. Credit: NASA, ESA, and J. Lotz, M. Mountain, A. Koekemoer, and the HFF Team (STScI).

to fit the cluster through minimization of χ^2 . Discrepancy between velocity dispersion calculated from weak-lensing data and that calculated from the dynamical study of [Girardi & Mezzetti \(2001\)](#), along with A2744 having the second highest cluster luminosity of the sample, further supported the idea that A2744 is the result of two merging clusters.

[Merten et al. \(2011\)](#) carried out the first comprehensive strong lensing and weak lensing mass reconstruction of Abell 2744. A parametric method was used to identify 34 multiple images from 11 background sources. Weak lensing analysis was done by combining three image sets (*HST/ACS*, *VLT/FORS1*, and Subaru/SuprimeCam) to get ellipticity measurements of background galaxies, and a final shear map. A total χ^2 to be minimized consisted of a strong lensing term (dependent upon the lensing Jacobian), a weak lensing term (dependent upon the complex reduced shear), and a regularization term. The resulting mass, estimated as a function of radius, was $M(r < 1.3Mpc) = 1.8 \pm 0.4 \cdot 10^{15} M_{\odot}$, and $M(r < 250kpc) = 2.24 \pm 0.55 \cdot 10^{14} M_{\odot}$. The joint X-ray and lensing analysis revealed four main mass components, and provided clarity into the merging details of Abell 2744.

The CATS collaboration produced a mass model of Abell 2744 each year of the HFF program (v1: [Richard et al., 2014](#), v2: [Jauzac et al., 2015](#), v3: [Jauzac et al., 2016](#), v4: [Mahler et al., 2018](#)). The algorithm LENSTOOL was used to model cluster mass distributions from strong and weak lensing data. They represent the cluster’s mass distribution by a few large cluster-scale haloes and galaxy-scale haloes. A Markov Chain Monte Carlo (MCMC) sampler is used to probe the parameter space and find the best fitting solution to the lens equation ([Jullo et al., 2007](#)). [Richard et al. \(2014\)](#) used pre-HFF data of 55 images from 18 sources along with weak lensing data to obtain a best fitting model with Lens-plane RMS of $1.26''$. [Jauzac et al. \(2015\)](#) used only strong lensing data and two cluster-scale haloes to model the core. The best fitting model used 154 images from 54 sources and produced a Lens-plane RMS of $0.79''$. [Jauzac et al. \(2016\)](#) used new spectroscopic redshifts from [Wang et al. \(2015\)](#) to model Abell 2744 with a combined strong and weak lensing data set. Using 113 images from 39 different background sources, their best fit model produced a Lens-plane RMS of $0.70''$. [Mahler et al. \(2018\)](#) performed an analysis of MUSE observations to extract new spectroscopic redshifts for objects in Abell 2744. An updated strong and weak lensing mass reconstruction obtained a Lens-plane RMS of $0.67''$ from 188 images and 60 systems.

[Johnson et al. \(2014\)](#) also used the parametric method LENSTOOL lens inversion algorithm to model galaxy clusters using strong lensing data. A total of 47 images from 15 sources were used with redshifts either computed from Bayesian Photometric Redshifts (BPZ), measured from spectroscopy, or obtained from [Richard et al. \(2014\)](#). Cluster member galaxies and 5, including 2 in the core, cluster-scale haloes were modelled with the

psuedo-isothermal elliptical mass distributions (PIEMD). The iteration process uses minimization in the source plane, which is easier and computationally cheaper, but concludes with a minimization in the image plane. The resulting mass model with a Lens-plane RMS of $0.40''$ produced a central mass of $M(r < 250kpc) = 2.43_{-0.07}^{+0.04} 10^{14} M_{\odot}$, within the range of Merten et al. (2011).

Zitrin et al. (2014) used light traces mass (LTM) lensing model to reconstruct the mass distribution of Abell 2744. Their models assume that both the baryonic and dark matter components follow the light distribution, but to different degrees. A MCMC was used to find the best fit solution to the cluster's mass distribution. The best fitting model produced a Lens-plane RMS of $1.3''$. Zitrin et al. (2014) used another version of the algorithm, with elliptical NFW distributions, to check image positions predicted by LTM. This allowed them to find one of the most distant multiply imaged galaxies, at $z \approx 10$.

Lam et al. (2014) utilized a free-form lens reconstruction method, known as WSLAP+, to determine the cluster mass. The algorithm finds solutions for the surface mass density and positions of background sources in the source plane, by solving a set of linear equations. In addition to the free-form part to represent the cluster, parametric forms for cluster member galaxies were used. Model and photometric redshifts were used to identify several new image systems and correct several previously known systems, bringing the total image number to 65 from 21 background sources. The resulting mass model highlighted two major cluster components and significant excess mass near a large region of X-ray emission. The best mass model produced a Lens-plane RMS of $1.25''$.

Wang et al. (2015) used a free-form lens reconstruction method, called SWUNITED, to reconstruct Abell 2744 using strong and weak lensing data, over an adaptive grid. This lens inversion method differs from most other methods in that it reconstructs lensing potential, instead of projected mass. Using multiply imaged sources and ellipticity of background galaxies as input, the algorithm minimizes χ^2 and converges to a final solution of the potential. Version v1 used pre-HFF data, including 44 images from 11 background sources. Using new spectroscopic Grism Lens-Amplified Survey from Space (GLASS) data, their selection algorithm found 72 images from 25 distinct sources. Their v2 mass model found two main mass peaks in the core and a lesser third peak north of the center.

Medezinski et al. (2016) performed a weak lensing analysis of Abell 2744 using newly obtained imaging from Subaru/Suprime-Cam. The reduced shear from background galaxies was used to construct the mass distribution out to 5 Mpc, the largest extent probed by lensing in this cluster. Four substructures were found and modelled with NFW and truncated NFW profiles. Results suggested an alternative merging scenario compared to

Merten et al. (2011): the northwestern mass clump is the result of a smaller merger from two haloes that are falling into the main core of the cluster, instead of being produced from a ‘slingshot’ effect of the main merger activity, as suggested by Merten et al. (2011).

The GLAFIC team used a parametric reconstruction method applied to strong lensing data. The mass distribution of the cluster was modeled with cluster-scale NFW haloes, pseudo-Jaffe ellipsoids for cluster member galaxies, and external perturbations. A best fit model was found using a downhill-simplex algorithm to minimize a χ^2 . Errors of the mass models were derived through MCMC. Ishigaki et al. (2015) used pre-HFF image data (67 images from 24 background sources) to model Abell 2744 and find faint galaxies at high redshifts. Kawamata et al. (2016) used 111 images from 37 sources to produce their v3 map which had a Lens-plane RMS of $0.37''$. Kawamata et al. (2018) increased the total number of images used to 132 from 45 sources for their v4 map, which produced a Lens-plane RMS of $0.42''$.

4.3 Grale Setup

We describe two sets of Abell 2744 reconstructions, HFFv3 and HFFv4, carried out using multiple image data shared by the HFF community.

4.3.1 HFFv3

We generated 40 GRALE reconstructions based on 55 multiply lensed images from 18 different sources for HFFv3. The image list was compiled by the HFF community data presented in Richard et al. (2014); Johnson et al. (2014); Wang et al. (2015); Jauzac et al. (2015). Six sources had spectroscopic redshifts from Richard et al. (2014); Johnson et al. (2014); Wang et al. (2015), and the rest of the sources used model redshifts from Jauzac et al. (2015). Each reconstruction was the result of finding the best solution of nine successive grid refinements. We increased the number of Plummer spheres in each subsequent grid by approximately 200. The number of Plummers in the first and last grid were chosen by the genetic algorithm from ranges of 300-400 and 1700-1800, respectively. The final solution for each reconstruction was chosen based on the fitness values, described above, for all nine grids. Each reconstruction is started with its own random seed, and is somewhat different from the rest because of the very large dimensionality of the parameter space that the genetic algorithm searches. An average is taken of these 40 reconstructions, which highlights the common features in the mass distribution, and suppresses one-off features.

4.3.2 HFFv4

For HFFv4, we produced 40 GRALE reconstructions using 91 multiply lensed images from 29 different sources. All 91 images used updated spectroscopic redshifts from [Mahler et al. \(2018\)](#). There is some overlap between the image lists for our HFFv3 and HFFv4. There are 29 images, from 10 sources, that have the same positions for both HFF versions. Of these, 10 images have a difference in redshift $|\delta(z_{v3} - z_{v4})| < 0.1$, whereas the rest have a larger difference in redshift up to $|\delta(z_{v3} - z_{v4})| = 1.42$. We used only images with spectroscopic redshifts because they typically have a higher degree of accuracy than model redshifts.

The process for producing mass distribution solutions for HFFv4 is similar to that for HFFv3 described above, with one exception. The number of Plummer spheres in each grid refinement no longer increased linearly with grid number. Instead, the number of Plummer spheres increased by, on average, 175, starting from the first to seventh grid, ending with a maximum range of 1100-1200. The eighth and ninth grid had approximately 150 fewer Plummer spheres than the preceding grid. This procedure, similar to what was used in [Mohammed et al. \(2014\)](#), and different from that used for Abell 2744 in HFFv3, was implemented to test if reducing the number of Plummer spheres, and hence parameters, will retain the goodness of fit achieved in the seventh grid. The best mass map for each run was selected according to the fitness values of the nine grids. The eighth and ninth grids were the most frequently preferred by GRALE, showing that GRALE does not always converge to the grid with the highest number of Plummer spheres. As for HFFv3, an average of the 40 individual reconstructions was calculated as the best solution for HFFv4.

4.4 Results of Lens Reconstruction

The average mass maps of the 40 individual GRALE reconstructions for HFFv3 and HFFv4 are shown in left and right panels, respectively, of [Fig. 4.2](#). The contour lines represent the projected surface mass density, Σ , starting from 0.1 g/cm^2 and linearly spaced by 0.1 g/cm^2 . The left (right) panel has twelve (eight) lines, with the last one at 1.2 g/cm^2 (0.8 g/cm^2). The red circles represent the images used as input for each version. The two brightest cluster galaxies (BCGs) are highlighted as magenta crosses. The elongated shape of Abell 2744 is clearly visible in both maps. Likewise, the two major cluster components that have been identified by previous reconstructions, are found by both maps. HFFv3 shows steeper mass peaks around the two BCGs, relative to HFFv4; we will return to this in [Section 4.6](#). Both versions produced good Lens-plane RMSs, $0.53''$ and $0.87''$ for HFFv3 and HFFv4, respectively. The mass enclosed within 250 kpc of the cluster center is

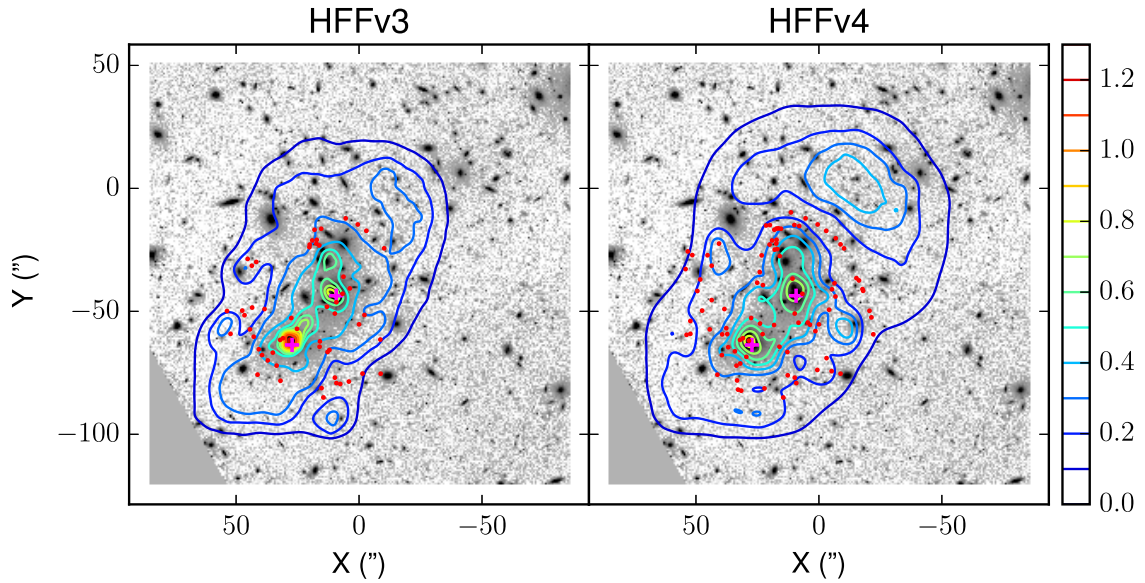


Figure 4.2 Mass contours of averaged mass map of Abell 2744 overlaid on a HST total (F435W, F606W, and F814W combined) image. *Left:* HFFv3; *Right:* HFFv4. The lines represent mass contour in units of g/cm^2 and red circles represent images used in the two reconstructions. The two BCGs are labelled as magenta crosses.

$M(r < 250 \text{ kpc}) = 2.25 \times 10^{14} M_{\odot}$ and $2.27 \times 10^{14} M_{\odot}$ for HFFv3 and HFFv4, respectively, nearly the same as that found by [Merten et al. \(2011\)](#) and 2.3σ lower than the value found by [Johnson et al. \(2014\)](#).

Next, we look at the fractional mass uncertainty in the HFFv3 and HFFv4 sets of 40 individual reconstructions. For a set of mass maps, the fractional uncertainty at any point in the lens plane is ϵ/Σ where ϵ is the root-mean-square deviation in the maps' Σ values. Fig. 4.3 shows the fractional uncertainty map for HFFv3 (left panel) and HFFv4 (right panel). Similar to MACS J0416 in [Sebesta et al. \(2016\)](#), GRALE produces low fractional uncertainty within the cluster region where images lie. Most of the cluster's elongated shape, the central $\sim 20'' \times 60''$, has errors below 10% for HFFv4, and below 20% for HFFv3. Circular regions of radius $r \approx 2.5''$ around the two BCGs have errors of less than 10% in both versions. Outside the center of the cluster, where there are no images, the fractional uncertainty is $\gtrsim 30 - 50\%$, with no clear pattern, because GRALE is not constrained here and is therefore less reliable in reconstructing the mass distribution.

In addition to analysing the results of our reconstructions, we also present the comparison of HFFv3 and HFFv4. Prompted by the Hubble Frontier Fields project, several papers have examined the statistical and systematic uncertainties in lens reconstruction methods

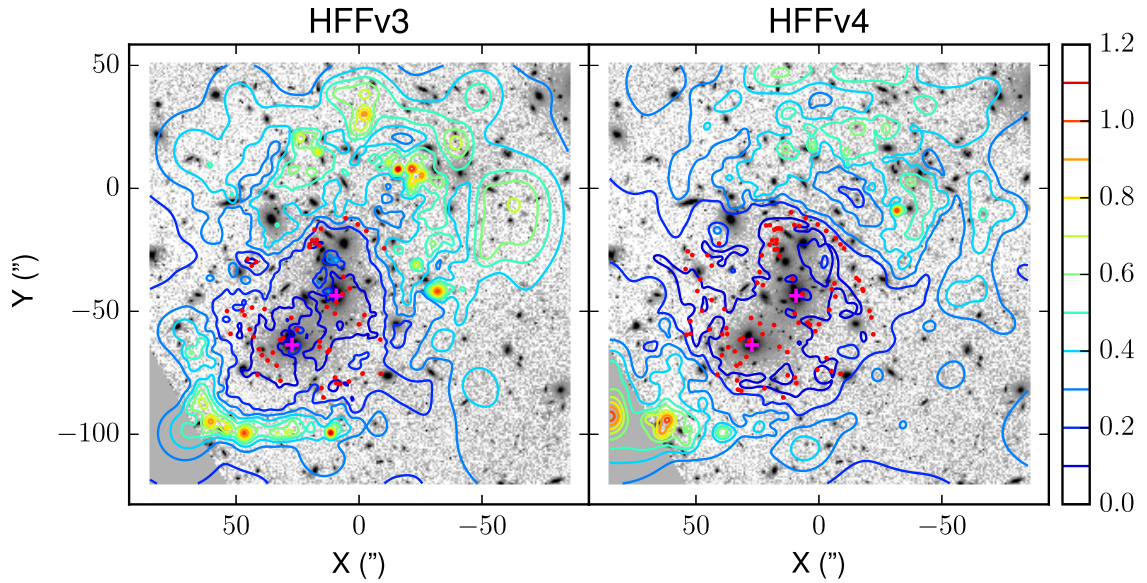


Figure 4.3 Contours of fractional uncertainty in surface mass density of Abell 2744, overlaid on the same HST image as in Fig. 4.2 with same field of view. *Left:* HFFv3; *Right:* HFFv4. The contours are linearly spaced by 10% and start at 10% (dark blue line). The left panel has a total of ten contour lines and the right panel has a total of eleven contour lines. Images are highlighted by red circles and the two BCGs are marked as magenta crosses.

(Meneghetti et al., 2017; Priewe et al., 2017; González et al., 2018). Most of these analyses compared different lens inversion methods, while keeping the input data as similar as possible. Our approach is the opposite: we use (nearly) the same lens inversion method, but different data input. We compare two reconstructions of Abell 2744 using GRALE, that are based on different data sets, both in terms of image sets used, image positions, and source redshifts; only 10 out of 91 images used in HFFv4 are the same in all respects, as in HFFv3. The two implementations of GRALE are also somewhat different, as described in Sections 4.3.1 and 4.3.2.

The left panel of Fig. 4.4 shows the difference map of HFFv3 and HFFv4, $\Delta_{\Sigma} = \Sigma_{v3} - \Sigma_{v4}$. A more meaningful understanding of the difference map can be gained by considering the significance, defined as $\sigma_{\Sigma} = \Delta_{\Sigma} / \sqrt{\epsilon_{v3}^2 + \epsilon_{v4}^2}$, which highlights regions of the lens plane where discrepancies in the mass distributions are statistically significant. The σ_{Σ} map is shown in the right panel of Fig. 4.4.

Since GRALE relies solely on image data as input, it is instructive to see if there is a direct connection between changes in input data and changes in the resulting mass distribution. The circles in Fig. 4.4 represent images, used in both reconstructions, that have a significant change in input redshift, $|z_{v4} - z_{v3}| > 0.1$. Yellow circles are images with a

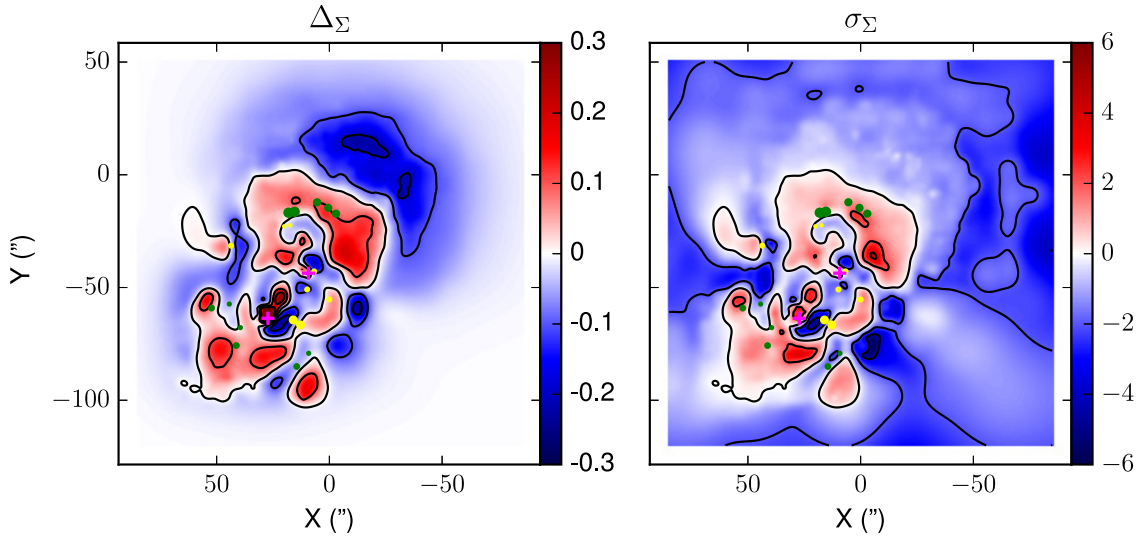


Figure 4.4 *Left:* Difference map of the two mass reconstructions of Fig. 4.2, $\Delta_{\Sigma} = \Sigma_{v3} - \Sigma_{v4}$, where v3 and v4 are for HFFv3 and HFFv4 respectively. The solid contour lines are at $\Delta_{\Sigma} = 0, \pm 0.1, \pm 0.2$. *Right:* Map of the statistical significance of the difference map. The solid contour lines are at $\sigma_{\Sigma} = 0, \pm 2, \pm 4$. The yellow and green circles represent images that have a difference in redshift of $\delta(z_{v3} - z_{v4}) > 0.1$ and $\delta(z_{v3} - z_{v4}) < -0.1$, respectively. The size of the circle corresponds to the magnitude of difference in redshift. Both panels show the same region as in Fig. 4.2 and Fig. 4.3.

positive difference (HFFv4 redshift is larger) and green circles are images with a negative difference (HFFv3 redshift is larger). The radius of the circle is scaled to the change in redshift, with the target difference being $|z_{v3} - z_{v4}| = 1.42$. The distribution of these images reveals no clear pattern in the difference or significance map, implying that the input image data affects the mass distribution on most of the lens plane.

The steeper density profiles in the few arcseconds around the two BCGs in HFFv3 (Fig. 4.2 and the left panel of Fig. 4.4), is seen to have $\sim 2\sigma$ significance in the right panel of Fig. 4.4. Though the difference is not statistically significant, it is still interesting to understand the reason for it. The peaks in the difference and significance maps surrounding the Southern BCG are caused by the higher concentration of Plummer spheres in HFFv3 compared to HFFv4. Recall from Sec. 4.3 that HFFv3 reconstructions used more Plummer spheres as inputs than HFFv4. Combined with the fact that GRALE refines the grid based on the local mass density, which is high close to galaxies, and that HFFv3 was allowed to continue to refine the grid in the eighth and ninth grids, resulted in the HFFv3 average map having roughly four times as many Plummer spheres within a $4''$ radius around the Southern BCG compared to the same region in the HFFv4 average map. It is important to note that this higher concentration of mass, or higher steepness, is possible because there are no images within $\sim 5''$ of the BCG center to act as model constraints. In regions with no constraints, the monopole degeneracy (Liesenborgs et al., 2008) is free to redistribute the mass in any circularly symmetric, mass conserving fashion.

The differences between the two mass maps, expressed in units of GRALE derived errors (right panel of Fig. 4.4) tells us how robust GRALE reconstructions are to changes in input lens data and GRALE implementation procedure, and how reliable GRALE's estimate of uncertainties is. The area of regions with significant differences in mass distribution, $\sigma_{\Sigma} \geq 4$, is 74.85 sq. arcsec, which is very small compared to the area covered by the cluster. Since most of the mass maps HFFv3 and HFFv4 are within each other's errors, GRALE-derived uncertainties can be trusted, because they cover changes in mass distribution if the true images properties turn out to be somewhat different from the ones used as input.

Somewhat different, but consistent findings about GRALE-derived uncertainties are presented in Rodney et al. (2015) Figure 6, where GRALE's uncertainties on the magnification of Type Ia SN HFF14Tom cover nearly the full range of uncertainties of all other lens inversion methods, as well as the true magnification of the supernova. Priewe et al. (2017) extended this type of magnification analysis to the whole strong lensing regions of MACS J0416 and Abell 2744, and confirmed the conclusion obtained from a single lens plane location of SN HFF14Tom.

4.5 Influence of the mass to the North West of the main cluster

GRALE reconstructions show a prominent broad peak North West of the main cluster, with HFFv4 showing a larger mass excess than HFFv3. It is located approximately at $(-15'', 0'')$ in Fig. 4.2, and about $50''$ to the North West of the northern BCG. While the peak is beyond the image region, and hence outside the region that GRALE can constrain well, it sits in the area of relatively low fractional mass uncertainties, $\lesssim 30$, in both versions. The detailed features of this mass clump cannot be taken too seriously, but its existence and approximate location are robust.

This mass clump is at the same location as the broad peak in the X-ray distribution of Abell 2744, seen, for example in the maps X-ray luminosity contours presented in [Merten et al. \(2011\)](#). However, despite the coincidence in the location of the peak, the mass in the X-ray emitting gas is unlikely to be large enough to cause the mass clump. [Govoni et al. \(2001b\)](#) examined the X-ray emission of Abell 2744, as a part of a larger study. From their Fig. 14, the X-ray mass within $r \approx 100$ kpc of the X-ray peak is $M \approx 5 \times 10^{11} M_{\odot}$. Within the same radius, GRALE finds $M_{v3} = 3.17 \times 10^{13} M_{\odot}$ and $M_{v4} = 4.88 \times 10^{13} M_{\odot}$, or about 100 times more than the mass in X-ray emitting gas. Assuming the X-ray gas mass to be an external point source, located at the peak of the X-ray emission, outside the main cluster, the amplitude of deflection angles at the North West and South East ends of the lensed image distribution are $\alpha \approx 0.16''$ and $\alpha \approx 0.04''$, respectively. Since these are smaller than the Lens-plane RMS of any reconstruction, it is unlikely that either GRALE or any other lens inversion method would be able to discern the X-ray gas.

Instead, the excess mass recovered by GRALE must be attributed to the cluster merging with A2744, located about $150''$ North West of A2744. In GRALE reconstructions this mass acts as external shear due to the merging cluster. This cluster is seen directly in wider field weak lensing reconstructions ([Merten et al., 2011](#); [Wang et al., 2015](#); [Jauzac et al., 2016](#); [Medezinski et al., 2016](#)), and also in strong lensing reconstruction, for example, [Johnson et al. \(2014\)](#) and [Lam et al. \(2014\)](#).

4.6 Comparing the distributions of light and mass in Abell 2744

In this section we look at how closely the distribution of mass follows the light distribution of cluster member galaxies. GRALE is well suited for this purpose, since no information

about member galaxies is used as input in creating the mass maps. Only one other existing techniques is similar to GRALE in this regard—SWUNITED (Wang et al., 2015)—all others use parametrized forms to represent mass in cluster galaxies. We utilize two types of analysis to quantify how closely cluster member galaxies of Abell 2744 follow the overall mass distribution.

4.6.1 Local Mass Peaks near Massive Galaxies

Fig. 4.5 zooms in on the central region of Fig. 4.2, containing the four central massive galaxies, labeled in magenta as G1-G4. According to the right panel of Fig. 4.3 this region has fractional uncertainty $\lesssim 10\%$ for HFFv4 reconstruction, i.e. it is well constrained. For HFFv3 (left panel), the fractional uncertainty is larger, $\lesssim 20 - 30\%$, but still low enough for consideration. As indicated by the mass density contour lines, both HFFv3 and HFFv4 pick out the two prominent mass concentrations, associated with G1-G2 and G3. These correspond to the cluster-scale dark matter haloes used in previous literature. Galaxy G4 is also identified by GRALE, but many galaxies further away from the center are not; in several cases mass contour lines go right through fainter galaxies.

The contour lines represent projected density distribution of the average GRALE maps, and the magenta dots show the local mass density peaks, within a circle of radius $5''$ centered on the four galaxies, G1-G4, in each of the 40 individual reconstructions. The dispersion of these points on the lens plane gives an estimate of the uncertainty in the location of the mass peaks associated with the massive central galaxies. The clouds of magenta points are centered on the corresponding galaxies, consistent with there being no detectable offsets between the center of light and the center of mass, on scales larger than $\sim 3''$, or ~ 14 kpc. This is consistent with the findings of Massey et al. (2018) in the case of Abell 3827.

The distribution of magenta points around G1 and G2 galaxies is more compact in HFFv4 compared to HFFv3, and requires some explanation. The inset in the right panel of Fig. 4.5 shows a zoomed in version of this region. We believe that the reason for this compact distribution is a single observed lensed image, located between G1 and G2. This image is a part of a five-image configuration. In the absence of any information about the light distribution, GRALE is interpreting this system as a regular “quad” with a central image. However, this is most likely a misinterpretation. Because of the presence of adjacent G1 and G2 near that image, instead of single mass peak, the actual image configuration is probably more complex, and the image multiplicity is seven. The observed central image is likely a saddle point in the arrival time surface, with two galaxies producing nearby maxima in the arrival time. (This triple is surrounded by the 4 images of a quad.) But

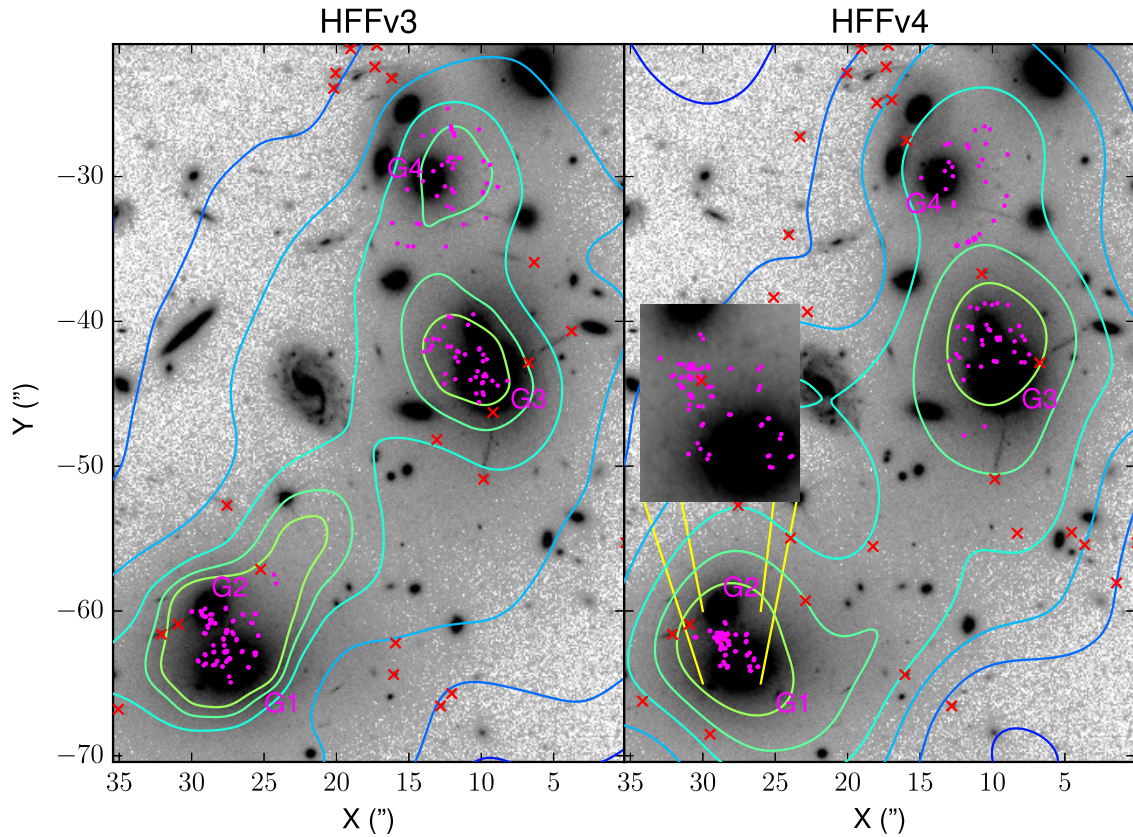


Figure 4.5 Zoomed in area of Fig. 4.2, spanning $35.6''$ by $49.6''$, with the left and right panel showing HFFv3 and HFFv4 respectively. Magenta points represent peaks of 40 mass reconstructions in the projected surface mass density around four main galaxies, labelled G1-G4. These points were slightly displaced from their positions by random amounts to make them visible. (The points were obtained on a grid, so many were superimposed.) Red crosses are the images used for each reconstruction version. Contours lines match the scale from Fig.4.2, but only extend up to 0.7 g/cm^2 . Higher density contour lines were left out for clarity around local mass peak points. A zoomed in region around G1 and G2 of HFFv4 is provided in the right panel. It uses a lighter gray scale shading to highlight the region between the two galaxies.

GRALE prefers the simpler five-image solution, where the central image is a maximum in the arrival time surface. There are no other images within $\sim 2 - 3''$ to help GRALE with the interpretation.

4.6.2 Mass-Galaxy Correlation Function

The second technique we will use to investigate how well light traces mass is the correlation function between cluster member galaxies and average mass maps, $\xi_{gm}(\theta)$. The probability of finding a second galaxy in a small area, dS , at distance, θ , away from a galaxy is $dP = n(1 + \xi_{gm})dS$, where n is the average surface number density of galaxies within that cluster. This metric $\xi_{gm}(\theta)$ will help us determine if total mass, which is mostly dark matter, clusters with visible galaxies in Abell 2744. We use the same estimator as in 3.4.2, $\xi_{gm}(\theta) = \frac{D_g D_m(\theta)}{\langle R_g D_m \rangle(\theta)} - 1$, where $D_g D_m$ is the number of galaxy-mass pixel pairs, and $\langle R_g D_m \rangle$ is the number of random galaxy-mass pixel pairs, averaged over 100 realizations. (Here, D stands for direct, and R stands for random.)

A Subaru galaxy catalogue was provided to us by E. Medezinski, which encompasses the total field of view for Abell 2744. We restrict our galaxy-mass correlation calculation to the core of Abell 2744, where strong lensing features are present. We use a circular region centered on $\alpha = 3.5886563$ $\delta = -30.401297$ with radius $r = 39''$ and a bin size of $0.39''$. This region encompasses all the images of HFFv3 and most of the images of HFFv4, along with the two BCGs in the core of Abell 2744. Our choice of Subaru galaxies requires masking to deal with the light of bright galaxies that may block nearby fainter galaxies. When calculating the galaxy-mass correlation functions, we mask regions around the 10 brightest galaxies with a circle of variable radius ($4-11''$), which scales with the galaxy brightness profile in Subaru images.

The correlation function between Subaru R-band and Z-band galaxies and averaged HFFv3 and HFFv4 mass maps are shown in the two panels of Fig. 4.6. We chose eight magnitude cuts to investigate the behaviour of GRALE reconstructions against Subaru galaxies. The numbers of galaxies used in each magnitude cut are listed in the figure.

The galaxy-mass correlation functions in Fig. 4.6 for both versions of GRALE show similar behavior, clearly showing that the reconstructed total mass clusters around brighter galaxies. However, comparing HFFv3 and HFFv4 within each galaxy color shows that $\xi_{gm}(\theta)$ of HFFv3 has a higher amplitude than that of HFFv4 for every magnitude cut. This is a direct consequence of the mass distribution around galaxies being less peaked in HFFv4 compared to HFFv3, already seen in Fig. 4.2. In addition to being more peaked, $\xi_{gm}(\theta)$ of HFFv3 shows small elbows, around $\theta \approx 6 - 7''$, which can be attributed to the very central

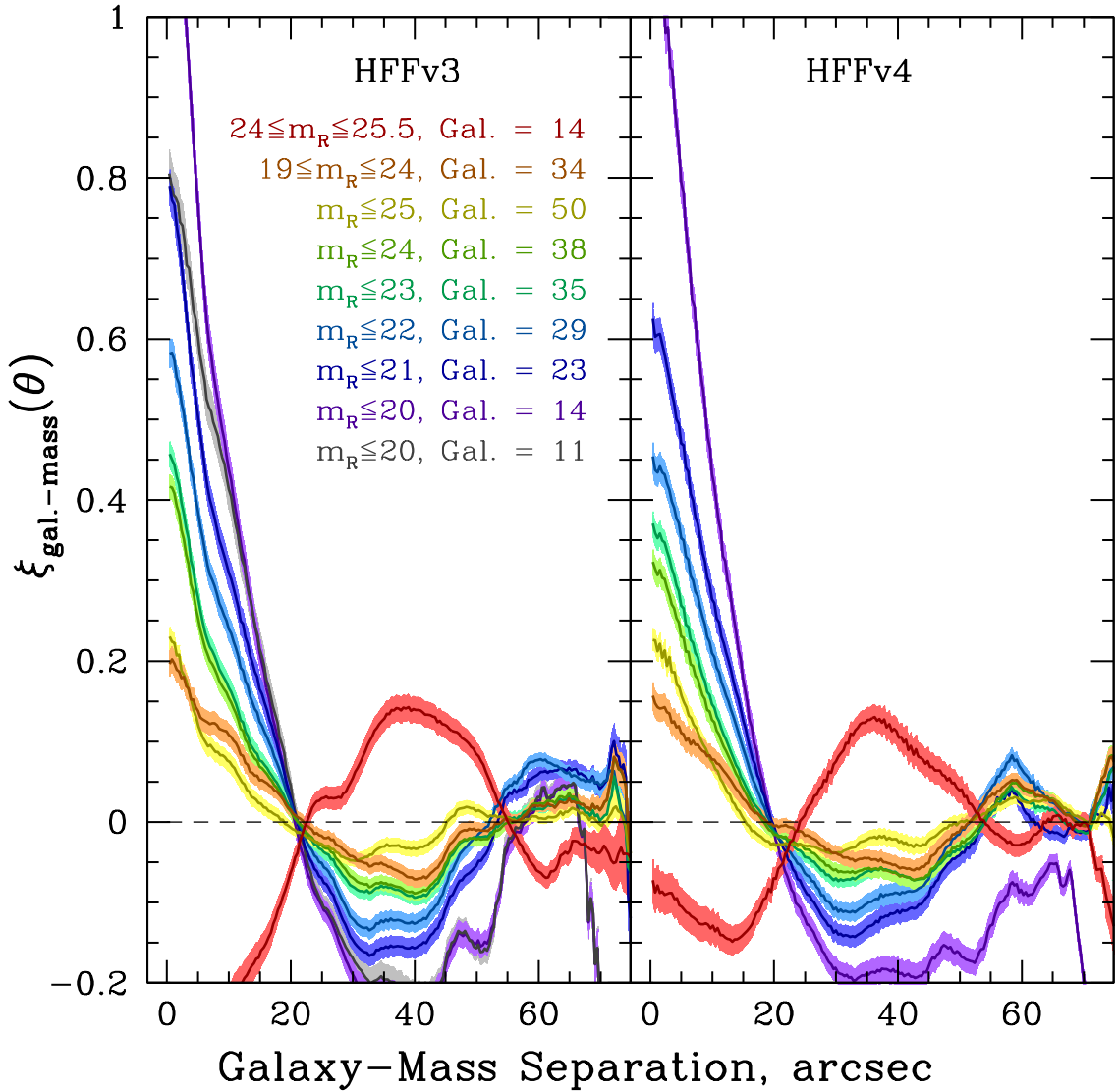


Figure 4.6 The left and right panel show normalized galaxy-mass correlation functions for R-band Subaru galaxies with HFFv3 and HFFv4 averaged mass maps, respectively. These calculations were done in a circular region centered on the core of Abell 2744 and over eight magnitude cuts of the galaxies. Each magnitude cut is color coded and has the number of galaxies within it listed. An additional correlation function (gray) is done for HFFv3 which is the same as the $m_R \leq 20$, but with galaxies G1-G3 removed. Shaded regions are 1σ error bars, such that the RMS dispersion for 100 randomizations of $D_m R_r$ is between 0.01 and 0.025 for both panels.

peaks in HFFv3 being more massive than in HFFv4. To test if the most massive galaxies are solely responsible for the elbow, we removed the galaxies G1-G3 from the $m_R \leq 20$ magnitude bin and computed the normalized correlation function for HFFv3, shown as a gray band in the left panel of Fig. 4.6. This correlation function has an initial amplitude close to the one for the $m_R \leq 21$ magnitude cut, then falls off more gradually and connects to the $m_R \leq 20$ correlation function around $12''$ separation. Since the elbow persists, we conclude that the elbows are due to a wide range of galaxies, and are likely the result of the differences in GRALE's resolution in HFFv3 vs. HFFv4, discussed in Section 4.4. Both reconstructions show a crossing of zero correlation around $20''$ which is approximately the separation between the two BCGs.

The trend of brighter galaxies clustering stronger with mass matches the results of our previous study of GRALE's reconstruction of MACSJ0416, another HFF galaxy cluster. The standard biasing scenario of galaxy formation states that galaxies are biased tracers of the underlying mass distribution and GRALE's results are further validations of this. The faintest galaxies contain the least amount of mass and are least biased to mass; conversely, brighter galaxies cluster closely to mass. For both reconstructions in Fig. 4.6, the initial amplitudes of $\xi_{gm}(\theta)$ grow as the galaxy magnitudes decrease.

The correlation functions between Subaru Z-band galaxies and the two GRALE reconstructions are shown in Fig.4.7. The general results of the galaxy-mass correlation functions for the Z-band galaxies follow the galaxy-mass correlation functions for the R-band galaxies, in both GRALE reconstruction versions. As the galaxies get fainter, the correlation amplitude decreases, but the amplitude of HFFv3 is always higher than that of HFFv4 for the same magnitude cuts.

The galaxy-mass correlation function is a powerful tool to investigate how well light traces mass in galaxy clusters, but caution needs to be exercised when selecting the galaxies to use. Whereas bright galaxies are most likely cluster members, faint galaxies can be background galaxies that underwent lensing magnification bias, and can be falsely included as members. Magnification bias is the result of two effects. The area behind the lens is enlarged, thereby diluting the number density of background galaxies. The second effect, competing against the first, is that background galaxies are magnified to appear brighter than unlensed galaxies at the same redshifts. The slope of the unlensed number counts of background galaxies determines which of the two effects dominates. The two effects cancel each other when the slope of $d \log(n[f])/d \log(f) = 1$, or $d \log(n[m])/dm = 0.25$, if magnitudes are used.

The differential galaxy counts of the entire Subaru field as a function galactic magnitude

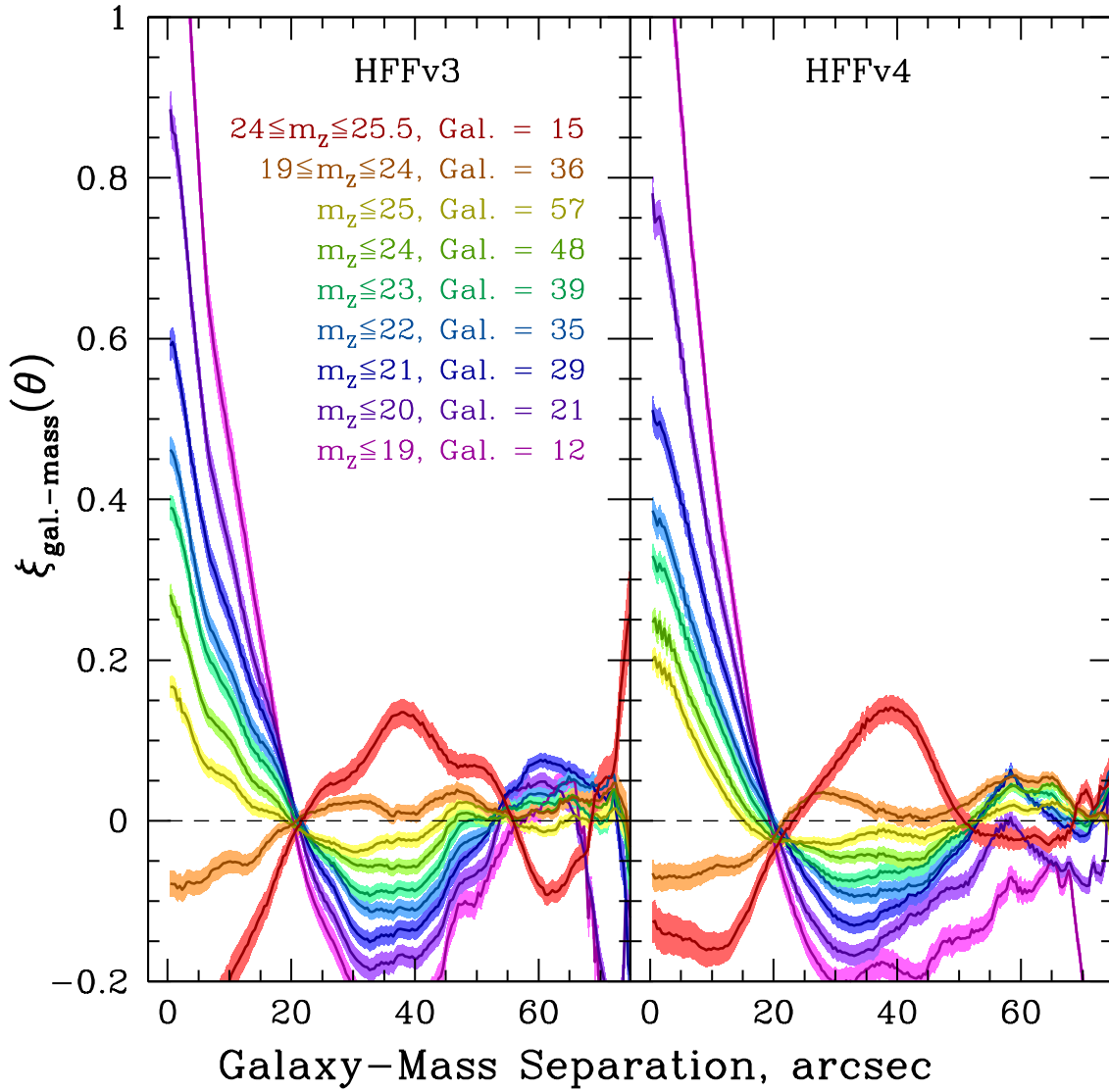


Figure 4.7 Same plot as Fig.4.6 with normalized galaxy-mass correlation functions for Z-band Subaru galaxies with HFFv3 and HFFv4 averaged mass maps on the left and right panels, respectively. These calculations were done in a circular region centered on the core of Abell 2744 and over nine magnitude cuts of the galaxies.

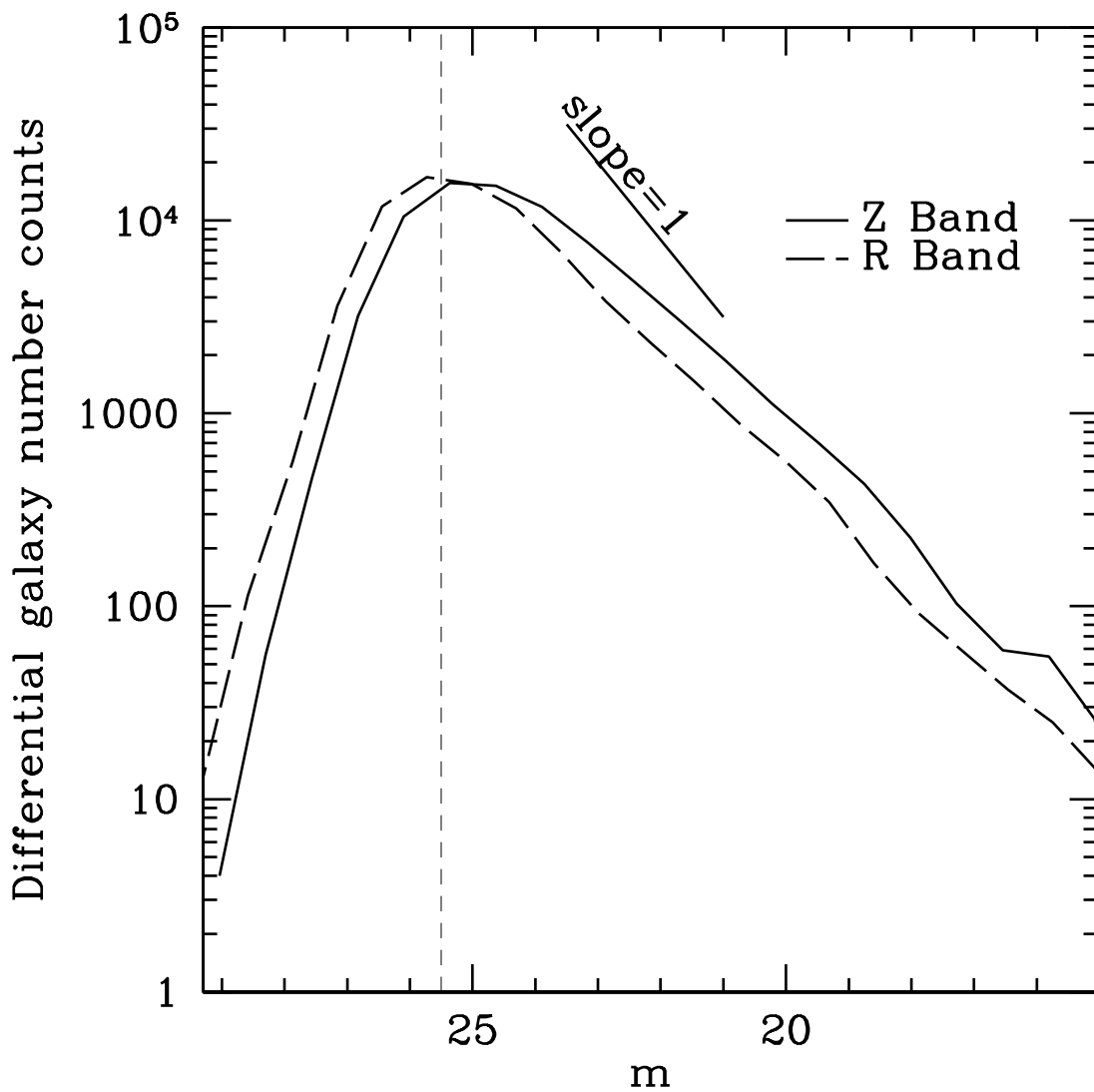


Figure 4.8 Differential number galaxy counts versus magnitude of Subaru R-band and Z-band galaxies. Because of low number counts in the cluster region, the field of view used is the entire Subaru region. A dashed vertical line indicates where the catalogue suffers from incompleteness. A solid line with slope equal to one is provided for reference.

for Subaru R-band, Z-band are plotted in Fig. 4.8. Since most of the galaxies are not behind the central region of Abell 2744, these counts are, effectively, unlensed. A line of slope $d\log(n[f])/d\log(f) = 1$ is provided for reference. For magnitudes fainter than $m \approx 19$ for Z-band and R-band, the slope is shallower than $d\log(n[f])/d\log(f) = 1$, and the net effect of the magnification bias is to decrease the galaxy counts behind a lens. This results in an anti-correlation between cluster mass and galaxies. Around $m \approx 25.5$, the counts begin to flatten off and suffer from incompleteness. Thus we choose 2 magnitude cuts, $24 \leq m \leq 25.5$ and $19 \leq m \leq 24$, for Subaru Z-band and R-band to look at magnification bias.

In the $19 \leq m \leq 24$ range, the slope of Z-band galaxies is shallower than that of R-band galaxies, so stronger anti-correlation is predicted for Z-band galaxies in this magnitude range. In fact, anti-correlations are observed for both HFFv3 and HFFv4 for the Z-band, but R-band galaxies show a positive correlation with mass in both reconstructions. This suggests that in this magnitude range, a larger fraction of R-band, compared to Z-band galaxies are cluster members.

Since faint galaxies are believed to be behind the cluster, the faintest magnitude cuts, $24 \leq m \leq 25.5$, should be anti-correlated more strongly with reconstructed mass. Fig.4.6 and Fig.4.7 shows the $24 \leq m \leq 25.5$ magnitude cut provides the strongest anti-correlation between averaged mass and Subaru galaxies, as expected. HFFv3 shows stronger anti-correlation than HFFv4 across both Subaru bands.

We can use the BPZ redshift estimates of the Subaru galaxy catalogue to check our conclusion that magnification bias affects the faintest magnitude ranges of the correlation function. Fig.4.9 shows Subaru magnitudes plotted against BPZ redshifts for both R-band (blue dots) and Z-band (red crosses) galaxies. Two dashed lines, one at the cluster redshift $z = 0.308$, and one at magnitude $m = 24$ are plotted for reference. Using a conservative redshift range for a cluster member galaxies, $\Delta z \sim \pm 0.2$, we see that at $m \geq 23$ a substantial fraction of galaxies is background to the cluster, and will contribute to the magnification bias seen at the fainter magnitudes in Figs.4.6 & 4.7. Thus, the galaxy-mass correlation functions between GRALE mass and faint Subaru galaxies reveal magnification bias exists in Abell 2744.

4.7 Conclusions

Using exquisite lens image data provided by the Hubble Frontier Field observations, and collaborative nature of the HFF project, we were able to address two questions pertaining to galaxy clusters. The first question asks how trustworthy are the uncertainties in the

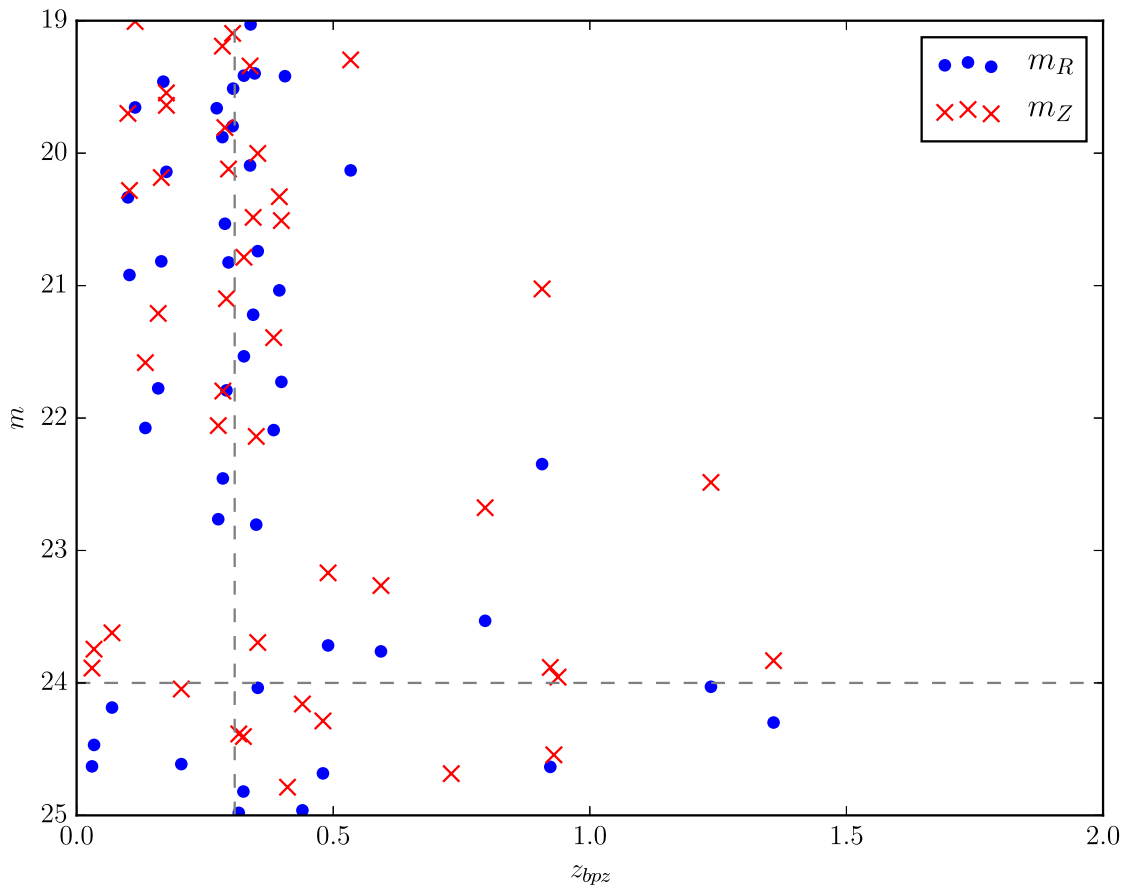


Figure 4.9 Plot of magnitudes of Subaru galaxies against BPZ redshifts. Blue dots indicate R-band Subaru galaxies and red x's are Z-band Subaru galaxies. Two lines are provided for clarity, one on the cluster redshift, $z = 0.308$, and the other at the magnitude $m = 24$ separating our two magnitude cuts.

derived mass distribution of galaxy clusters? Our answer is for GRALE only. The second question asks do galaxies follow the underlying mass distribution within a galaxy cluster? GRALE is exemplary as a method to answer this question because no inputs are related to light from galaxies.

We performed two mass reconstructions of Abell 2744 using GRALE, a free-form genetic algorithm-based lens inversion method. The first reconstruction, HFFv3, used 55 images as inputs with a mix of spectroscopic and photometric redshifts from [Richard et al. \(2014\)](#); [Johnson et al. \(2014\)](#); [Wang et al. \(2015\)](#); [Jauzac et al. \(2015\)](#). Our second reconstruction, HFFv4, made use of 91 images with spectroscopic redshifts from [Mahler et al. \(2018\)](#). To gauge the robustness of GRALE reconstruction against changes in data and small modifications in the inversion procedure, we directly compare both versions to each other. This also shows the value/usefulness of GRALE derived uncertainties. Both averaged mass maps have small Lens-plane RMSs of $0.53''$ for HFFv3 and $0.87''$ for HFFv4. The overall elongated shape of Abell 2744 and the two major cluster components are picked out by both versions. On a smaller scale, differences in the mass peaks arise because of changes in the input image list and Plummer sphere concentrations. GRALE captures the features of Abell 2744 very well and this is most evident by the area above $|\sigma_{\Sigma}| > 4$ being small, $A = 74.85$ sq. arcsec.

In regards to the cluster light and mass distributions, we find light follows our mass, reconstructed by GRALE and with no information pertaining to cluster member galaxies. This result is seen across both reconstruction versions and calculated with the galaxy-mass correlation function. Lensing magnification bias is present in Abell 2744 because the mass is anti-correlated with the faintest galaxies in the line of sight.

Chapter 5

Lens-plane RMS

5.1 Introduction

The Lens-plane RMS is a comparative metric, commonly used within the field of lens reconstruction, to gauge solutions of a galaxy cluster’s projected surface mass density. It examines how well the mass distribution reproduces observed image positions. Many massive galaxy clusters show multiple-image systems and other strong lensing features. The set of all observed images of a galaxy cluster acts as input for all lens reconstruction methods, for both parametric and free-form methods that use strong lensing data. Some lens reconstruction methods utilize the Lens-plane RMS in their optimization of the mass model solution. Other methods calculate and use the source-plane RMS. From the literature, it appears the lensing community has not decided on the exact treatment of calculating the Lens-plane RMS. This chapter will detail describe the algorithm for finding projected-forward positions and several definitions of the Lens-plane RMS.

5.2 `imgsol.py`: Algorithm to find forward projected image positions from `Grale` output

`GRALE` does not calculate the Lens-plane RMS when solving for the mass distribution, so an independent algorithm was developed. The usual output of `GRALE` for the mass distribution is an $N \times M$ grid for the projected surface mass density, in units of kg/m^2 . Initial versions of this algorithm used the grid but had trouble converging to distances smaller than the grid spacing, $\approx 0.25''$. To circumvent this problem, `GRALE` can output the mass distribution as a list of the Plummer spheres that make up the cluster mass.

To calculate the lens-plane RMS, the algorithm starts by projecting back all images to

the source plane using the lens equation Eq. 1.11 and Eq. 1.30. Visual inspection of these back-projected positions is made to ensure images of the same source are close to each other. Next, the algorithm uses the previous two equations to find the projected-forward positions in the lens plane. Given a source position, all observed image positions are used as initial guesses to find the projected-forward positions. The algorithm uses *optimize.root* from *NumPy* package to find a root, the projected-forward position, of the lens equation.

There are three cases for the result of *optimize.root*: (i) successfully converged to the correct image position (ii) successfully converged to a 'wrong' image position (iii) failed to converge. The algorithm tries this multiple times per initial guess of observed image position, with slight randomization of the initial guess position introduced after each new iteration. If case (i) arises, then the final position is accepted as the correct project-forward position.

The difference between (i) and (ii) arises when two (or more) images are very close to each other. For the simplest case of two images close to each other, using the observed images positions as initial guesses for the root finder leads to the same projected-forward position. We identify which image this projected-forward position belongs to by which ever observed image is closer. The other observed image position is labeled as a 'wrong' image. A search is then made for this wrong image, to find it's correct projected-forward position. Using the 'wrong' image position as the origin, a coordinate axes is set up with the nearest observed image position being the positive x-axis. A new projected-forward position is looked for along each axis with the root finder. This goes until a new image position is found that corresponds to the 'correct' image. The distance this projected-forward position is away from the origin is used to make sure the algorithm didn't converge to a spurious image. If a new image cannot be found then the 'wrong' image position is accepted as the projected-forward position.

The accepted image position from case (iii) is handled a bit differently than 'wrong' images from case (ii). During the initial tries at finding an accepted projected-forward position, if the algorithm fails, the count of each failed position is maintained. The failed position with the highest count is accepted as the projected-forward position then.

An additional check is made for both case (ii) and case (iii) to see if the algorithm is near a critical line. A separate code was written to make a magnification check with Eq. 1.24. The convergence and shear are calculated with Eqs. 1.31 & 1.32 for every position the root finder ends up at, with each observed position as the initial guesses. A histogram of the magnifications are produced and a cut-off is chosen such that magnification above it correspond to positions near a critical line; for example magnifications of $\mu \approx 10,000$ were

seen. For Abell 2744, the magnification cut-off was chosen as 100. If the position from the root finder is near a critical line, then it is accepted as the projected-forward position. For case (ii) this usually arises such that two (or more) images merge with each other, and trying to find additional unique images is difficult.

Finally, the list of projected-forward positions is compiled and the lens-plane RMS is calculated.

5.3 Lens-plane RMS Definitions

Each reconstruction of the mass distribution of a galaxy cluster has $i = 1, \dots, I$ sources, and each source has $j = 1, \dots, J_i$ observed images. The location of each image is denoted by $\vec{\theta}_{i,j}$. The total number of lensed images in the whole cluster is $J = \sum_{i=1, I} J_i$. Each observed image j of source i , $\vec{\theta}_{i,j}$ is lensed back to the source plane using the lens equation, Eq. 1.11, and the deflection angles calculated from the mass distribution. From here on, there are two different ways to proceed, (I) use each of these back-projected images as a source itself, or (II) average the positions of these back-projected images belonging to the same source, in the source plane, to obtain a single model-predicted source.

(I) Each of the $j = 1, \dots, J_i$ back-projected images in the source plane is used as a source itself, i.e. lensed forward, or relensed, to the lens plane, producing J_i model predicted images per each observed image, and $K_i = J_i^2$ model predicted images per source. Their locations are designated by $\vec{\theta}_{i,j,k}$. One of the J_i relensed images should coincide exactly with the corresponding observed image, and is used as a test of the code. There are a total of $K = \sum_{i=1, J} K_i = \sum_{i=1, I} (J_i)^2$ relensed images in the whole cluster.

There are three possible ways to calculate the lens plane rms using all K individual back-projected images. The first is to sum up the deviations of all the K model predicted (i.e., relensed) images from the observed images, in quadrature. Of all five methods we present here, this is the most conservative calculation because it explicitly takes into account every model-predicted image, and adds them in quadrature. It typically yields the largest rms value.

$$\left(\Delta_{\text{rms,tot}}^{\text{I}}\right)^2 = \frac{1}{K} \sum_{i=1, I} \left\{ \sum_{j=1, J_i} \left[\sum_{k=1, J_i} \left| \vec{\theta}_{i,j,k} - \vec{\theta}_{i,j} \right|^2 \right] \right\}. \quad (5.1)$$

While in eq. 5.1 sources with more images contribute more to the rms, in the second method all sources contribute equally, regardless of the number of images they have,

$$\left(\Delta_{\text{rms,src}}^{\text{I}}\right)^2 = \frac{1}{J} \sum_{i=1, I} \left\{ \sum_{j=1, J_i} \left[\frac{1}{J_i} \sum_{k=1, J_i} \left| \vec{\theta}_{i,j,k} - \vec{\theta}_{i,j} \right|^2 \right] \right\}. \quad (5.2)$$

Finally, the average position of the J_i relensed images is compared to the corresponding observed image position. The distance between these are

$$|\vec{\theta}_{\text{obs}} - \vec{\theta}_{\text{mod I}}| = (\Delta\theta_{i,j;x}^2 + \Delta\theta_{i,j;y}^2)^{1/2}, \quad (5.3)$$

where

$$\Delta\theta_{i,j;x} = \left(\frac{1}{J_i} \sum_{k=1, J_i} \theta_{i,j,k;x} \right) - \theta_{i,j;x}, \quad (5.4)$$

and similarly for the y -component. These distances are summed in quadrature to produce,

$$\left(\Delta_{\text{rms,ims}}^{\text{I}} \right)^2 = \frac{1}{J} \sum_{i=1, I} \left\{ \sum_{j=1, J_i} \left| \vec{\theta}_{\text{obs}} - \vec{\theta}_{\text{mod I}} \right|^2 \right\} \quad (5.5)$$

Typically, eq. 5.5 yields the smallest of eq. 5.1, eq. 5.2, and eq. 5.5 estimated rms values.

(II) Another way to calculate the lens plane rms is to first find the average of the J_i model back-projected images in the source plane. This gives the model-predicted source position. This is then lensed forward to obtain J_i model predicted images, one per observed image. The distance between these corresponding model-predicted and observed images is calculated,

$$\left| \vec{\theta}_{\text{obs}} - \vec{\theta}_{\text{mod II}} \right|^2 = (\theta_{\text{mod II}; i,j;x} - \theta_{i,j;x})^2 + (\theta_{\text{mod II}; i,j;y} - \theta_{i,j;y})^2 \quad (5.6)$$

and used as in eq. 5.8, except that eq. 5.6 is different from eq. 5.3.

$$\left(\Delta_{\text{rms,ims}}^{\text{II}} \right)^2 = \frac{1}{J} \sum_{i=1, I} \left\{ \sum_{j=1, J_i} \left| \vec{\theta}_{\text{obs}} - \vec{\theta}_{\text{mod II}} \right|^2 \right\} \quad (5.7)$$

We believe that most papers use this definition, however, some, like [D'Aloisio & Natarajan \(2011\)](#) take the average of eq. 5.6 values, one per source, instead of adding them in quadrature:

$$\Delta_{\text{rms,avg}}^{\text{II}} = \frac{1}{J} \sum_{i=1, I} \left\{ \sum_{j=1, J_i} \left| \vec{\theta}_{\text{obs}} - \vec{\theta}_{\text{mod II}} \right| \right\} \quad (5.8)$$

Chapter 6

Summary

Gravitational lensing is a powerful tool to study astronomical objects on a variety of scales. The massive size of galaxy clusters make them very good choices as lenses to magnify distant background galaxies. The goal of this thesis was to use the lensing power of six massive galaxy clusters of the Hubble Frontier Fields program to reconstruct their mass distributions, and to study in depth these mass distributions for insights into the characteristics of clusters. We used a free-form method, known as GRALE, to reconstruct the mass distributions using strong lensing data. In Chapter 2, we reported our existing reconstructions of each Hubble Frontier Fields cluster, including publicly available maps of lensing observables, like magnification and shear, for each reconstruction. In Chapters 3 and 4 we reviewed existing mass models of MACS J0416 and Abell 2744, respectively, while analyzing our own reconstructions of these clusters.

We used two methods to investigate if light traces mass: local mass peaks around the brightest cluster galaxies and the galaxy-mass correlation function. In our three reconstructions, one of MACS J0416 and two of Abell 2744, we found no significant offsets between the brightest cluster galaxies and distribution of mass peaks nearby on a scale of $\approx 10 - 15kpc$. In Chapter 3, we compared GRALE and two LENSTOOL-based galaxy-mass correlation functions of MACS J0416 and found agreement between all on the overall features. Around small separations, $< 1''$, the LENSTOOL galaxy-mass correlation functions had much larger amplitudes than GRALE because of modeling cluster galaxies in the reconstruction technique. In Chapter 4, our two reconstructions, using no input from cluster member galaxies, found the brightest cluster galaxies were tightly correlated to our mass distributions. An interesting feature was produced in one of the galaxy-mass correlation functions, distinctive elbows around $6 - 7''$, because of a higher concentration of Plummer spheres, around the bright galaxies.

We conclude that light traces mass within two Hubble Frontier Fields clusters, Abell 2744 and MACS J0416. The member galaxies, of these two clusters, are biased tracers of the total mass distribution. Also, we found magnification bias present in both clusters because of the anti-correlation between mass and the faintest galaxies in each cluster.

There exist many lens reconstruction methods and several previous studies have compared the statistics across them. We looked at the uncertainties derived from our free-form lens reconstruction. We presented an analysis of two GRALE reconstructions of Abell 2744, using different input data. The resulting mass models highlighted the features of the cluster comparably. So much that the area of significant differences in the mass distributions is small relative to the size of the cluster. This shows the robustness of uncertainties derived from GRALE reconstructions.

Lens-plane RMS is a conventional metric within lens reconstruction to compare the goodness of cluster mass distributions. In Chapter 5, we explained our algorithm for calculating the Lens-plane RMS, since GRALE does not incorporate the statistic within its method. While the Lens-plane RMS is widely used, a common definition has not been settled on by the community. Therefore, we presented several definitions that depend on the treatment of back and forward projected positions of images from the same source. We obtained small Lens-plane RMS values for our two Abell 2744 reconstructions, $0.53''$ and $0.87''$.

References

- Allen, S. W. 1998, *Monthly Notices of the Royal Astronomical Society*, 296, 392, doi: [10.1046/j.1365-8711.1998.01358.x](https://doi.org/10.1046/j.1365-8711.1998.01358.x)
- Bouwens, R. J., Illingworth, G. D., Oesch, P. A., et al. 2017a, *The Astrophysical Journal*, 843, 41, doi: [10.3847/1538-4357/aa74e4](https://doi.org/10.3847/1538-4357/aa74e4)
- Bouwens, R. J., Oesch, P. A., Illingworth, G. D., Ellis, R. S., & Stefanon, M. 2017b, *The Astrophysical Journal*, 843, 129, doi: [10.3847/1538-4357/aa70a4](https://doi.org/10.3847/1538-4357/aa70a4)
- Bouwens, R. J., Illingworth, G. D., Oesch, P. A., et al. 2010, *The Astrophysical Journal*, 709, L133, doi: [10.1088/2041-8205/709/2/L133](https://doi.org/10.1088/2041-8205/709/2/L133)
- Brammer, G. B., van Dokkum, P. G., Illingworth, G. D., et al. 2013, *The Astrophysical Journal*, 765, L2, doi: [10.1088/2041-8205/765/1/L2](https://doi.org/10.1088/2041-8205/765/1/L2)
- Bullock, J., Dickinson, M., Finkelstein, S., et al. 2012, *Hubble Deep Fields Initiative 2012 Science Working Group Report Table of Contents*, Tech. rep.
- Casertano, S., de Mello, D., Dickinson, M., et al. 2000, *The Astronomical Journal*, 120, 2747, doi: [10.1086/316851](https://doi.org/10.1086/316851)
- Clowe, D., Bradač, M., Gonzalez, A. H., et al. 2006, *The Astrophysical Journal*, 648, L109, doi: [10.1086/508162](https://doi.org/10.1086/508162)
- Coe, D., Bradley, L., & Zitrin, A. 2015, *The Astrophysical Journal*, 800, 84, doi: [10.1088/0004-637X/800/2/84](https://doi.org/10.1088/0004-637X/800/2/84)
- Coe, D., Umetsu, K., Zitrin, A., et al. 2012, *Astrophysical Journal*, 757, doi: [10.1088/0004-637X/757/1/22](https://doi.org/10.1088/0004-637X/757/1/22)
- Cypriano, E. S., Sodre, Jr., L., Kneib, J.-P., & Campusano, L. E. 2004, *The Astrophysical Journal*, 613, 95, doi: [10.1086/422896](https://doi.org/10.1086/422896)

- D'Aloisio, A., & Natarajan, P. 2011, *Monthly Notices of the Royal Astronomical Society*, 411, 1628, doi: [10.1111/j.1365-2966.2010.17795.x](https://doi.org/10.1111/j.1365-2966.2010.17795.x)
- Diego, J. M., Broadhurst, T., Molnar, S. M., Lam, D., & Lim, J. 2015, *Monthly Notices of the Royal Astronomical Society*, 447, 3130, doi: [10.1093/mnras/stu2660](https://doi.org/10.1093/mnras/stu2660)
- Ferrari, C., Govoni, F., Schindler, S., Bykov, A. M., & Rephaeli, Y. 2008, *Space Science Reviews*, 134, 93, doi: [10.1007/s11214-008-9311-x](https://doi.org/10.1007/s11214-008-9311-x)
- Finkelstein, S. L., Ryan, R. E., Papovich, C., et al. 2015, *The Astrophysical Journal*, 810, 71, doi: [10.1088/0004-637X/810/1/71](https://doi.org/10.1088/0004-637X/810/1/71)
- Giavalisco, M., Ferguson, H. C., Koekemoer, A. M., et al. 2004, *The Astrophysical Journal*, 600, L93, doi: [10.1086/379232](https://doi.org/10.1086/379232)
- Giovannini, G., Tordi, M., & Feretti, L. 1999, *New Astronomy*, 4, 141, doi: [10.1016/S1384-1076\(99\)00018-4](https://doi.org/10.1016/S1384-1076(99)00018-4)
- Girardi, M., & Mezzetti, M. 2001, *The Astrophysical Journal*, 548, 79, doi: [10.1086/318665](https://doi.org/10.1086/318665)
- González, J. D. R., Sharon, K., & Mahler, G. 2018. <https://arxiv.org/abs/1807.03291>
- Govoni, F., Enßlin, T. A., Feretti, L., & Giovannini, G. 2001a, *Astronomy & Astrophysics*, 369, 441, doi: [10.1051/0004-6361:20010115](https://doi.org/10.1051/0004-6361:20010115)
- Govoni, F., Feretti, L., Giovannini, G., et al. 2001b, *Astronomy & Astrophysics*, 376, 803, doi: [10.1051/0004-6361:20011016](https://doi.org/10.1051/0004-6361:20011016)
- Grillo, C., Suyu, S. H., Rosati, P., et al. 2015, *Astrophysical Journal*, 800, doi: [10.1088/0004-637X/800/1/38](https://doi.org/10.1088/0004-637X/800/1/38)
- Hudson, D. S., Mittal, R., Reiprich, T. H., et al. 2010, *Astronomy and Astrophysics*, 513, A37, doi: [10.1051/0004-6361/200912377](https://doi.org/10.1051/0004-6361/200912377)
- Ishigaki, M., Kawamata, R., Ouchi, M., et al. 2015, *The Astrophysical Journal*, 799, 12, doi: [10.1088/0004-637X/799/1/12](https://doi.org/10.1088/0004-637X/799/1/12)
- Jauzac, M., Clément, B., Limousin, M., et al. 2014a, *Monthly Notices of the Royal Astronomical Society*, 443, 1549, doi: [10.1093/mnras/stu1355](https://doi.org/10.1093/mnras/stu1355)
- Jauzac, M., Jullo, E., Eckert, D., et al. 2014b, *Monthly Notices of the Royal Astronomical Society*, 446, 4132, doi: [10.1093/mnras/stu2425](https://doi.org/10.1093/mnras/stu2425)

- Jauzac, M., Richard, J., Jullo, E., et al. 2015, *Monthly Notices of the Royal Astronomical Society*, 452, 1437, doi: [10.1093/mnras/stv1402](https://doi.org/10.1093/mnras/stv1402)
- Jauzac, M., Eckert, D., Schwinn, J., et al. 2016, *Monthly Notices of the Royal Astronomical Society*, 463, 3876, doi: [10.1093/mnras/stw2251](https://doi.org/10.1093/mnras/stw2251)
- Johnson, T. L., Sharon, K., Bayliss, M. B., et al. 2014, *The Astrophysical Journal*, 797, 48, doi: [10.1088/0004-637X/797/1/48](https://doi.org/10.1088/0004-637X/797/1/48)
- Jullo, E., Kneib, J.-P., Limousin, M., et al. 2007, *New Journal of Physics*, 9, 447, doi: [10.1088/1367-2630/9/12/447](https://doi.org/10.1088/1367-2630/9/12/447)
- Kahlhoefer, F., Schmidt-Hoberg, K., Frandsen, M. T., & Sarkar, S. 2014, *Monthly Notices of the Royal Astronomical Society*, 437, 2865, doi: [10.1093/mnras/stt2097](https://doi.org/10.1093/mnras/stt2097)
- Kahlhoefer, F., Schmidt-Hoberg, K., Kummer, J., & Sarkar, S. 2015, *Monthly Notices of the Royal Astronomical Society: Letters*, 452, L54, doi: [10.1093/mnrasl/slv088](https://doi.org/10.1093/mnrasl/slv088)
- Kawamata, R., Ishigaki, M., Shimasaku, K., et al. 2018, *The Astrophysical Journal*, 855, 4, doi: [10.3847/1538-4357/aaa6cf](https://doi.org/10.3847/1538-4357/aaa6cf)
- Kawamata, R., Oguri, M., Ishigaki, M., Shimasaku, K., & Ouchi, M. 2016, *The Astrophysical Journal*, 819, 114, doi: [10.3847/0004-637X/819/2/114](https://doi.org/10.3847/0004-637X/819/2/114)
- Koda, J., Yagi, M., Yamanoi, H., & Komiyama, Y. 2015, *The Astrophysical Journal*, 807, L2, doi: [10.1088/2041-8205/807/1/L2](https://doi.org/10.1088/2041-8205/807/1/L2)
- Kravtsov, A. V., & Borgani, S. 2012, *Annual Review of Astronomy and Astrophysics*, 50, 353, doi: [10.1146/annurev-astro-081811-125502](https://doi.org/10.1146/annurev-astro-081811-125502)
- Lam, D., Broadhurst, T., Diego, J. M., et al. 2014, *The Astrophysical Journal*, 797, 98, doi: [10.1088/0004-637X/797/2/98](https://doi.org/10.1088/0004-637X/797/2/98)
- Liesenborgs, J. 2010, PhD thesis, Universiteit Hasselt. http://research.edm.uhasselt.be/jori/phd/phdthesis_{_}jori_{_}web.pdf
- Liesenborgs, J., De Rijcke, S., & Dejonghe, H. 2006, *Monthly Notices of the Royal Astronomical Society*, 367, 1209, doi: [10.1111/j.1365-2966.2006.10040.x](https://doi.org/10.1111/j.1365-2966.2006.10040.x)
- Liesenborgs, J., De Rijcke, S., Dejonghe, H., & Bekaert, P. 2007, *Monthly Notices of the Royal Astronomical Society*, 380, 1729, doi: [10.1111/j.1365-2966.2007.12236.x](https://doi.org/10.1111/j.1365-2966.2007.12236.x)

- . 2008, *Monthly Notices of the Royal Astronomical Society*, 389, 415, doi: [10.1111/j.1365-2966.2008.13586.x](https://doi.org/10.1111/j.1365-2966.2008.13586.x)
- . 2009, *Monthly Notices of the Royal Astronomical Society*, 397, 341, doi: [10.1111/j.1365-2966.2009.14912.x](https://doi.org/10.1111/j.1365-2966.2009.14912.x)
- Lotz, J. M., Koekemoer, A., Coe, D., et al. 2017, *The Astrophysical Journal*, 837, 97, doi: [10.3847/1538-4357/837/1/97](https://doi.org/10.3847/1538-4357/837/1/97)
- Mahler, G., Richard, J., Clément, B., et al. 2018, *Monthly Notices of the Royal Astronomical Society*, 473, 663, doi: [10.1093/mnras/stx1971](https://doi.org/10.1093/mnras/stx1971)
- Mann, A. W., & Ebeling, H. 2012, *Monthly Notices of the Royal Astronomical Society*, 420, 2120, doi: [10.1111/j.1365-2966.2011.20170.x](https://doi.org/10.1111/j.1365-2966.2011.20170.x)
- Markevitch, M., Gonzalez, A. H., Clowe, D., et al. 2004, *The Astrophysical Journal*, 606, 819, doi: [10.1086/383178](https://doi.org/10.1086/383178)
- Massey, R., Williams, L., Smit, R., et al. 2015, *Monthly Notices of the Royal Astronomical Society*, 449, 3393, doi: [10.1093/mnras/stv467](https://doi.org/10.1093/mnras/stv467)
- Massey, R., Harvey, D., Liesenborgs, J., et al. 2018, *Monthly Notices of the Royal Astronomical Society*, 477, 669, doi: [10.1093/mnras/sty630](https://doi.org/10.1093/mnras/sty630)
- McLeod, D. J., McLure, R. J., & Dunlop, J. S. 2016, *Monthly Notices of the Royal Astronomical Society*, 459, 3812, doi: [10.1093/mnras/stw904](https://doi.org/10.1093/mnras/stw904)
- Medezinski, E., Umetsu, K., Okabe, N., et al. 2016, *The Astrophysical Journal*, 817, 24, doi: [10.3847/0004-637X/817/1/24](https://doi.org/10.3847/0004-637X/817/1/24)
- Meneghetti, M., Natarajan, P., Coe, D., et al. 2017, *Monthly Notices of the Royal Astronomical Society*, 472, 3177, doi: [10.1093/mnras/stx2064](https://doi.org/10.1093/mnras/stx2064)
- Merten, J., Coe, D., Dupke, R., et al. 2011, *Monthly Notices of the Royal Astronomical Society*, 417, 333, doi: [10.1111/j.1365-2966.2011.19266.x](https://doi.org/10.1111/j.1365-2966.2011.19266.x)
- Mohammed, I., Liesenborgs, J., Saha, P., & Williams, L. L. R. 2014, *Monthly Notices of the Royal Astronomical Society*, 439, 2651, doi: [10.1093/mnras/stu124](https://doi.org/10.1093/mnras/stu124)
- Mohammed, I., Saha, P., Williams, L. L. R., Liesenborgs, J., & Sebesta, K. 2016, *Monthly Notices of the Royal Astronomical Society*, 459, 1698, doi: [10.1093/mnras/stw727](https://doi.org/10.1093/mnras/stw727)

- Montes, M., & Trujillo, I. 2018, MNRAS, 000, 1. <https://arxiv.org/abs/1807.11488>
- Narayan, R., & Bartelmann, M. 1996. <https://arxiv.org/abs/9606001>
- Navarro, J. F., Frenk, C. S., & White, S. D. M. 1996, The Astrophysical Journal, 462, 563, doi: [10.1086/177173](https://doi.org/10.1086/177173)
- Ogrea, G. A., van Weeren, R. J., Jones, C., et al. 2015, The Astrophysical Journal, 812, 153, doi: [10.1088/0004-637X/812/2/153](https://doi.org/10.1088/0004-637X/812/2/153)
- Owers, M. S., Randall, S. W., Nulsen, P. E. J., et al. 2011, The Astrophysical Journal, 728, 27, doi: [10.1088/0004-637X/728/1/27](https://doi.org/10.1088/0004-637X/728/1/27)
- Plummer, H. C. 1911, Monthly Notices of the Royal Astronomical Society, 71, 460, doi: [10.1093/mnras/71.5.460](https://doi.org/10.1093/mnras/71.5.460)
- Priewe, J., Williams, L. L. R., Liesenborgs, J., Coe, D., & Rodney, S. A. 2017, Monthly Notices of the Royal Astronomical Society, 465, 1030, doi: [10.1093/mnras/stw2785](https://doi.org/10.1093/mnras/stw2785)
- Randall, S. W., Markevitch, M., Clowe, D., Gonzalez, A. H., & Bradač, M. 2008, The Astrophysical Journal, 679, 1173, doi: [10.1086/587859](https://doi.org/10.1086/587859)
- Richard, J., Jauzac, M., Limousin, M., et al. 2014, Monthly Notices of the Royal Astronomical Society, 444, 268, doi: [10.1093/mnras/stu1395](https://doi.org/10.1093/mnras/stu1395)
- Rodney, S. A., Patel, B., Scolnic, D., et al. 2015, The Astrophysical Journal, 811, 70, doi: [10.1088/0004-637X/811/1/70](https://doi.org/10.1088/0004-637X/811/1/70)
- Sebesta, K., Williams, L. L. R., Mohammed, I., Saha, P., & Liesenborgs, J. 2016, Monthly Notices of the Royal Astronomical Society, 461, 2126, doi: [10.1093/mnras/stw1433](https://doi.org/10.1093/mnras/stw1433)
- Smail, I., Ellis, R. S., Dressler, A., et al. 1997, The Astrophysical Journal, 479, 70, doi: [10.1086/303844](https://doi.org/10.1086/303844)
- Umetsu, K., & Broadhurst, T. 2008, The Astrophysical Journal, 684, 177, doi: [10.1086/589683](https://doi.org/10.1086/589683)
- Umetsu, K., Zitrin, A., Gruen, D., et al. 2016, The Astrophysical Journal, 821, 116, doi: [10.3847/0004-637X/821/2/116](https://doi.org/10.3847/0004-637X/821/2/116)
- Wang, X., Hoag, A., Huang, K.-H., et al. 2015, The Astrophysical Journal, 811, 29, doi: [10.1088/0004-637X/811/1/29](https://doi.org/10.1088/0004-637X/811/1/29)

- Williams, L. L. R., & Saha, P. 2011, *Monthly Notices of the Royal Astronomical Society*, 415, 448, doi: [10.1111/j.1365-2966.2011.18716.x](https://doi.org/10.1111/j.1365-2966.2011.18716.x)
- Williams, R. E., Blacker, B., Dickinson, M., et al. 1996, *The Astronomical Journal*, 112, 1335, doi: [10.1086/118105](https://doi.org/10.1086/118105)
- Zitrin, A., Broadhurst, T., Umetsu, K., et al. 2010, *Monthly Notices of the Royal Astronomical Society*, 408, 1916, doi: [10.1111/j.1365-2966.2010.17258.x](https://doi.org/10.1111/j.1365-2966.2010.17258.x)
- Zitrin, A., Meneghetti, M., Umetsu, K., et al. 2013, *The Astrophysical Journal*, 762, L30, doi: [10.1088/2041-8205/762/2/L30](https://doi.org/10.1088/2041-8205/762/2/L30)
- Zitrin, A., Zheng, W., Broadhurst, T., et al. 2014, *The Astrophysical Journal*, 793, L12, doi: [10.1088/2041-8205/793/1/L12](https://doi.org/10.1088/2041-8205/793/1/L12)

Appendix A

Lens-plane RMS Code

```
#
```

```
#####
```

```
# imgsol.py: This program finds image solutions for an average  
# mass map by projecting back and then forward with  
# the lens equation.
```

```
#
```

```
# Input:
```

```
#
```

```
# Output:
```

```
# source_pos.txt :: source positions from every image back-  
# projected
```

```
# pfp_ave.txt :: projected-forward positions
```

```
# lprms.txt ::
```

```
#
```

```
# NOTE: some things are commented with #, these were used for  
# getting status during the run or debugging
```

```
#
```

```
#
```

```
#####
```

```

import sys
sys.path.insert(1, '/data/kalinka/sebesta/python')
#import glparas
#import cosmology
import numpy as np
import operator
from scipy import optimize
from glparas import c, G #grab c and G from glparas.py

#####
def line(p1, p2):
#-----
    '''
    This function calculates the slope and y-intercept from two
    points and then returns them.
    p1, p2 :: input arrays with a length of 2. First index is 'x'
    coordinate, 2nd is 'y' coordinate.
    '''
    m = (p1[1] - p2[1]) / (p1[0] - p2[0]) # Calculate the slope
    of the line
    b = p1[1] - m * p1[0]
    return m, b

#####
def ptonline(xc, yc, m, b, r, add):
#-----
    '''
    This functions finds the point (x, y) on a line  $y = mx + b$ 
    that is a distance r away from (xc, yc)
    x, y :: output point
    xc, yc :: input center point
    m, b :: slope and y-intercept for line between (x,y) and (
    xc, yc)
    r :: input distance away the two points are

```



```

    add    :: boolean for either adding (true) or subtracting (
        false) terms in equation for x
    '''
    if(add == True):
        term = np.sqrt(-b**2-2*b*xc*m+2*b*yc-(xc*m)**2+2*xc*m*yc
            +(m*r)**2+r**2-yc**2)
    else:
        term = operator.neg(np.sqrt(-b**2-2*b*xc*m+2*b*yc-(xc*m)
            **2+2*xc*m*yc+(m*r)**2+r**2-yc**2))
    x = (-b*m+xc+m*yc+term)/(m**2+1)
    y = m*x+b
    return x, y

#####
class constants:
#-----
    '''
        class of cosmology constants
    '''

#####
    def __init__(self, omega_m, omega_l, H_0):
#-----
        self.omega_m = omega_m
            #matter density
        self.omega_l = omega_l
            #dark energy density / lambda
        self.omega_k = 1.0 - omega_l - omega_m #
            curvature density, for flat normally zero
        self.H = H_0
            #Hubble parameter today
        self.h = H_0/100.
            #dimensionless Hubble parameter
        self.d_h = 299792.458/H_0 #
            Hubble distance, c/H_0 with c in units of km *
            s^-1

```

```

#####
class distances:
#-----
    '''
        class of different distances in cosmology
    '''

#####
    def codist(self, z1, z2, cosmo):
#-----
        '''
            This function calculates the comoving distance
            d_c in units of Mpc.
            z1, z2 :: redshifts with z1<z2
            cosmo :: class of cosmology constants (omega_m,
                omega_l, h, etc.)
            d_c    :: comoving distance
        '''

        dz = 0.0001
        z = z1 + 0.5 * dz
        d_c = 0.0
        while(z < z2):
            f = 1.0 + z
            demon = cosmo.omega_m * f**3 + cosmo.
                omega_k * f**2 + cosmo.omega_l
            d_c += dz / np.sqrt(demon)
            z += dz

        return d_c*cosmo.d_h

#####
    def tcodist(self, z1, z2, d_c, cosmo):
#-----
        '''
            This function calculates the transverse comoving
            distance d_M in units of Mpc.
            z1, z2 :: redshifts with z1<z2

```

```

    cosmo    :: class of cosmology constants (omega_m,
           omega_l, h, etc.)
    d_c      :: comoving distance
    d_M      :: transverse comoving distance
    '''

    d_M = 0.0
    f = np.sqrt(np.abs(cosmo.omega_k))
    if(cosmo.omega_k > 0.0):
        d_M = cosmo.d_h/f*np.sinh(f*d_c/cosmo.d_h
            )
        #print 'Omega_k > 0'
    elif(cosmo.omega_k < 0.0):
        d_m = cosmo.d_h/f*np.sin(f*d_c/cosmo.d_h)
        #print 'Omega_k < 0'
    else:
        d_M = d_c
    return d_M

#####
def angdist(self, d_M, z, d_A):
#-----
    '''
    This function calculates the angular diameter
        distance d_M in units of Mpc.
    z1          :: redshift z
    d_M         :: transverse comoving distance
    d_A         :: angular diameter distance
    '''

    d_A = 0.0
    d_A = d_M/(1.0+z)
    return d_A

#####
def defl_pl(image, D, px, py, pwidth, pmass, N):
#-----
    '''

```

```

This function calculates the deflection angle at point
from numerous Plummer spheres.
image    :: point to calculate the deflection at
D        :: d_ls/d_ol/d_os
px, py   :: center plummer coordinates in arcsecs
pwidth   :: plummer width in arcsecs
pmass    :: plummer mass in solar mass units
dfx, dfy :: deflection angle coordinates
'''

dfx, dfy = 0., 0. #Initialize deflection angles
factor = 4*G/c**2 #4G/c^2 in cgs
#m_sol = 1.989e33 # Solar mass in grams
for i in xrange(N): #Sum over plummers
    dfx += factor * m_sol * pmass[i] * D * (image[0]
        - px[i]) / ((image[0] - px[i])**2 + (image[1]
        - py[i])**2 + (pwidth[i])**2) * rad_arcs**2 #
        206265^2 for converting from radians to
        arcsecs
    dfy += factor * m_sol * pmass[i] * D * (image[1]
        - py[i]) / ((image[0] - px[i])**2 + (image[1]
        - py[i])**2 + (pwidth[i])**2) * rad_arcs**2
return dfx, dfy

```

```
#####
```

```
def kappa_pl(image, D, px, py, pwidth, pmass, N):
```

```
#
```

```
'''
```

```

This function calculates the convergence (kappa) at a
point from numerous Plummer spheres.

```

```

image    :: point to calculate the convergence at
D        :: d_ls/d_ol/d_os
px, py   :: center plummer coordinates in arcsecs
pwidth   :: plummer width in arcsecs
pmass    :: plummer mass in solar mass units
kappa    :: convergence at (image[0], image[1])

```

```

'''
kappa = 0.0 #Initialize convergence
factor = 4*G/c**2 #4G/c^2 in cgs
#m_sol = 1.989e33 # Solar mass in grams
for i in xrange(N):
    kappa += factor * m_sol * pmass[i] * D * pwidth[i]
           **2 / ((image[0] - px[i])**2 + (image[1] - py
           [i])**2 + (pwidth[i])**2)**2 * rad_arcs**2 #
           206265^2 for converting from radians to
           arcsecs
return kappa

#####
def gammal_pl(image, D, px, py, pwidth, pmass, N):
#-----
'''
This function calculates the first component of the shear
(gamma) at a point from numerous Plummer spheres.
image  :: point to calculate the shear at
D      :: d_ls/d_ol/d_os
px, py :: center plummer coordinates in arcsecs
pwidth :: plummer width in arcsecs
pmass  :: plummer mass in solar mass units
gammal :: first componenet of shear at (image[0], image
      [1])
'''
gammal = 0.0 #Initialize convergence
factor = 4*G/c**2 #4G/c^2 in cgs
#m_sol = 1.989e33 # Solar mass in grams
for i in xrange(N):
    gammal += factor * m_sol * pmass[i] * D * ((image
           [1] - py[i])**2 - (image[0] - px[i])**2) / ((
           image[0] - px[i])**2 + (image[1] - py[i])**2 +
           (pwidth[i])**2)**2 * rad_arcs**2 #206265^2
           for converting from radians to arcsecs

```

```

    return gamma1

#####
def gamma2_pl(image, D, px, py, pwidth, pmass, N):
#-----
    '''
    This function calculates the second component of the
    shear (gamma) at a point from numerous Plummer spheres
    .
    image    :: point to calculate the shear at
    D        :: d_ls/d_ol/d_os
    px, py   :: center plummer coordinates in arcsecs
    pwidth   :: plummer width in arcsecs
    pmass    :: plummer mass in solar mass units
    gamma2   :: second componenet of shear at (image[0], image
    [1])
    '''
    gamma2 = 0.0 #Initialize convergence
    factor = 4*G/c**2 #4G/c^2 in cgs
    #m_sol = 1.989e33 # Solar mass in grams
    for i in xrange(N):
        gamma2 += -2.0 * factor * m_sol * pmass[i] * D *
            ((image[1] - py[i]) * (image[0] - px[i])) / ((
            image[0] - px[i])**2 + (image[1] - py[i])**2 +
            (pwidth[i])**2)**2 * rad_arcs**2 #206265^2
            for converting from radians to arcsecs
    return gamma2

'''
Grab image data that is transformed into coordinates w.r.t. Gale
center
source :: identifier for which source the image belongs too
num     :: identifier for source, but starts at 1 and
         subsequently increases by 1
z       :: redshift

```

```

'''
img = np.genfromtxt('lensplane_images.txt', dtype=({'names': ['x',
    , 'y', 'source', 'z', 'num'], 'formats': ['f8', 'f8', 'i', 'f8',
    , 'i']}))
N = len(img['x']) #Number of images

# First thing is to get angular diameter distances and critical
    surface densities for every image

# Define cosmology.
cosmo = cosmology.constants(0.3, 0.7, 70)

# Define redshifts
z_o = 0.0 # observer redshift
z_l = 0.308 # lens redshift for Abell 2744

# Initialize angular diameter arrays
d_ol = np.zeros(N)
d_ls = np.zeros(N)
d_os = np.zeros(N)
scrit = np.zeros(N)

#Check Curvature is near zero
print "Omega_k:_" , cosmo.omega_k

d_c, d_M, d_A = 0.0, 0.0, 0.0 # Initialize distances
dist = cosmology.distances() # create cosmology.distance
    instance

# For loop over images to calculate the angular diameter
    distances and critical surface densities.
for i in xrange(N):
    z_s = img['z'][i]

```

```

# Calculate the observer to lens ang dist.
d_c = dist.codist(z_o, z_l, cosmo)
d_M = dist.tcodist(z_o, z_l, d_c, cosmo)
d_A = dist.angdist(d_M, z_l, d_A)

d_ol[i] = d_A * 3.08567758e24 # Convert from Mpc to cm

# Calculate the lens to source ang dist.
d_c = dist.codist(z_l, z_s, cosmo)
d_M = dist.tcodist(z_l, z_s, d_c, cosmo)
d_A = dist.angdist(d_M, z_s, d_A)

d_ls[i] = d_A * 3.08567758e24 # Convert from Mpc to cm

# Calculate the observer to source ang dist.
d_c = dist.codist(z_o, z_s, cosmo)
d_M = dist.tcodist(z_o, z_s, d_c, cosmo)
d_A = dist.angdist(d_M, z_s, d_A)

d_os[i] = d_A * 3.08567758e24 # Convert from Mpc to cm

#Calculate critical surface density
scrit[i] = c**2/(4*np.pi*G)*d_os[i]/d_ol[i]/d_ls[i]

#Import Plummer data of mass distribution
plummers = np.genfromtxt('../A2744_extended_dir00-39_plummers.dat',
dtype=(
{'names': ['x', 'y', 'width', 'mass'], 'formats': ['f8', 'f8',
, 'f8', 'f8']}))
index = np.where(plummers['mass'] == 0.0) #Get indices of all
plummers with zero mass

#For loop to get ride of zero mass plummers by creating new
arrays (px, py, pwidth, pmass)

```



```

for n in plummers.dtype.names:
    blah = 'p'+n
    exec( blah + '_=_'np.delete(plummers[n],index[0]) ')

#Open file to save back-projected or source positions
f_src = open('source_pos.txt', 'w', 0)

defl = np.zeros((2,N))
beta = np.zeros((2,N))
image = np.zeros(2)
#For loop over images to calculate source positions
for i in xrange(N):
    image = img['x'][i], img['y'][i]
    defl[0,i], defl[1,i] = glparas.defl_pl(image, d_ls[i]/d_ol[i]
        ]/d_os[i], px, py, pwidth, pmass, len(px)) #deflection
        angle of plummer
    beta[0,i], beta[1,i] = image[0] - defl[0,i], image[1] - defl
        [1,i] #lens equation
    np.savetxt(f_src, np.array([img['source'][i], img['num'][i],
        beta[0,i], beta[1,i]]).reshape((1, 4)), fmt='%i %i %%.18
        f%%.18f', newline='\n')

#If only want to calculate source/back-projected image positions,
uncomment below
#sys.exit('Stopping file')

#Define function for optimize.root
def fvec(image):
    dfx, dfy = glparas.defl_pl(image, d_ls[i]/d_ol[i]/d_os[i], px
        , py, pwidth, pmass, len(px))
    fx = beta[0,i]+dfx-image[0]
    fy = beta[1,i]+dfy-image[1]
    return fx, fy

#Open files for recording projected-forward positions

```

```

# 'a' for append mode and 0 for unbuffered mode (writes output
  during execution)
f = open('pfp_ave.txt', 'a', 0)
f2 = open('pfp_ave_s.txt', 'a', 0) #pfp_ave_status document.
  Gives any unusual errors when calculating the forward
  projected positions.

# holder acts as indexing variable to cycle through images and
  sources.
holder = 0
num = img['num']

',',

Calculate projected-forward positions, 'reensed' image positions
  below
i index is for looping over sources, j index is for looping over
  images

Typical output for pfp_ave.txt

```

<i>x</i>	<i>y</i>	<i>source</i>	<i>image</i>
14.492806194328091252	-85.032872753471067995	22	1
13	0.000000000000000000E+00		
	+00		
52.225188706004715300	-59.447408117002346728	22	2
13	-7.687646075282827951E-10		
	8.365503845197963528		
	E-10		
41.319095506368014981	-75.664516879076643363	22	3
13	4.298783551348606125E-12		
	1.932676241267472506		
	E-12		
14.474706295057405470	-84.932449177284951247	22	1
13	2.625526462907146197E-10		
	7.909761734481435269		
	E-11		

```

52.270264221782973380    -59.136460847752744030    22    2
      13    0.000000000000000000E+00    0.000000000000000000
E+00
41.134224885480996647    -75.761144996246983396    22    3
      13    1.065814103640150279E-13    -2.842170943040400743
E-13
14.619061271139178970    -85.064869432382266723    22    1
      13    8.384404281969182193E-13    -1.421085471520200372
E-14
52.288445887853491456    -59.403678494193336235    22    2
      13    -1.152500317402882501E-10    -3.443290097493445501
E-11
41.271762373385378453    -75.744998454252055353    22    3
      13    0.000000000000000000E+00    0.000000000000000000
E+00

```

The above snippet of a pfp_ave.txt gives an idea of how the below for-loops work. The first line with I is the start of a new source, j goes from 0-2 (python uses zero indexing) while i kept the same, then i+=1 and j: 0->2, lastly i+=1 and j: 0->2 since this is a three image system. There is a self-consistency check as fx and fy are (0., 0.) when the same image is lensed back and forward

```

'''

```

```

#Select what source range to calculate solutions from
for i in xrange(N): #xrange(ii, if): Starts at ii, and ends at if
    -1
    #Print out which image(holder) and source(num) the code is
        curently at
    print 'holder:', holder, 'num[i]:', num[i]

    #This if block finds the id's of the images from the same
        source
    #Also grabs the observed images positions as refx and refy
        arrays

```

```

if holder != num[i]:
    holder = num[i]
    j = i

while (holder == num[j]):
    j = j + 1
    if(j == N):
        break

jf = j #Comment out j and i for choosing with images to
        calculate the projected forward positions of. Similar
        to above, will start at ji and finish at jf-1
ji = i

# Set up reference arrays of set of image positions to
        check if converged solutions are within their
        neighborhood
diff = jf - ji # find how many image there are
refx = np.zeros(diff) # define arrays
refy = np.zeros(diff)
##srcx = np.zeros(diff) #Arrays to calculate average
        source position
##srcy = np.zeros(diff)
for k in xrange(diff):
    refx[k], refy[k] = img['x'][ji + k], img['y'][ji + k]
    ##srcx[k], srcy[k] = beta[0, ji+k], beta[1, ji + k]

##for k in xrange(diff):
        ##beta[0, ji+k] = np.sum(srcx)/diff
        ##beta[1, ji+k] = np.sum(srcy)/diff

#Check reference arrays
print 'refx:', refx
print 'refy:', refy

```

```

#Define image arrays:
img_sol = np.zeros((diff), dtype=[('x', 'f8'), ('y', 'f8'), (
    'fx', 'f8'), ('fy', 'f8')]) #array for image solutions for
this source where k in img_sol[k] corresponds to the
image id number of source set, (ie k=0 corresponds to
first image of #(diff) image set of source i), field names
for image positions and fx & fy of lens equation
img_fail = np.empty((0), dtype=[('x', 'f8'), ('y', 'f8'), ('
    index', 'i4'), ('fx', 'f8'), ('fy', 'f8'), ('count', 'i4')
    ]) #empty array for image fail positions for this source,
field names for image positions and fx & fy of lens
equation, index corresponds to the image id number of
source set
img_wimg = np.empty((0), dtype=[('x', 'f8'), ('y', 'f8'), ('
    index', 'i4'), ('fx', 'f8'), ('fy', 'f8')]) #wimg = 'wrong
image', empty array for images that didn't converge to
the correct closest image, field names for image positions
and fx & fy of lens equation, index corresponds to the
image id number of source set
nfail = 0 #Number of fail image searches

'''
Find projected-forward image positions for images of the same
source
i index loops over source from above for-loop, used in fvec
for optimize.root
j index below loops over images
'''
for j in xrange(ji, jf):
    print 'j:', j

    # initialize image array
    image = np.zeros(2)
    image[0], image[1] = img['x'][j], img['y'][j] #Initialize
    position with observed image position

```

```

#Setup parameters for finding roots to lens equations
dfx, dfy = 0., 0. #deflection angles in x & y coordinates
success = False
count = 0 #Iterator for how many times to find projected-
forward positions
iter_suc, maxsuc = 0, 5
solx, soly, funx, funy = 0.0, 0.0, 0.0, 0.0
maxiter = 10
dbest = 100.0 # Initialize distance between image and
converged solution
while(success != True):
    #Use optimize.root to find converged solution to
    forward-projected positions
    sol = optimize.root(fvec, image)
    #print 'count:', count, iter_suc, sol.success
    #print sol.x[0], sol.x[1], sol.success

    # Check if solution converged
    if (sol.success):
        # Now check to see if converged solution is
        within the right image position
        dmin = 100.0 # Initialize minimum distance
        for k in xrange(diff): # Compute distance
            between every image and look for closest image
            d = np.sqrt((sol.x[0] - refx[k])**2 + (sol.x
                [1] - refy[k])**2)
            if(d < dmin):
                dmin = d
                kbest = k
        #print ji, kbest, j
        if(ji + kbest == j): # Check if converged to
            correct image
            img_sol[j-ji]['x'], img_sol[j-ji]['y'] = sol.
                x[0], sol.x[1]

```

```

img_sol[j-ji][ 'fx '], img_sol[j-ji][ 'fy ' ] =
    sol.fun[0], sol.fun[1]
success = True
#np.savetxt(f_tot, np.array([img['source'][i
    ], j + 1, num[i], count, iter_suc, image
    [0], image[1], sol.x[0], sol.x[1], sol.fun
    [0], sol.fun[1], sol.success]).reshape(
    #(1, 12)), fmt='%i %i %i %i %i % .18
    f % .18f % .18f % .18f % .18E
    % .18E %s ', newline='\n')
else:
    if (img_wimg.size == 0): #Check if img_wimg is
        empty
        img_wimg = np.append(img_wimg, np.array
            ([[ sol.x[0], sol.x[1], j-ji, sol.fun
            [0], sol.fun[1]]], dtype=img_wimg.
            dtype))
        count = maxiter-1 #Break out of current
            loop, only want 1 wrong img per one
            convergence loop of 'j', -1 because of
            count += 1 below within this else
            statement
    else:
        nf = 0 #count for img_wimg to see if sol.
            x is contained within it
        ni = 0 #count for matching indices within
            img_wimg
        for k in xrange(len(img_wimg['x'])):
            d = np.sqrt((img_wimg['x'][k] - sol.x
                [0])**2 + (img_wimg['y'][k] - sol.
                x[1])**2)
            if (d < 1.e-2):
                nf += 1

```

```

        if(j-ji == img_wimg['index'][k]): #
            Checks if any images within the
            same 'j' are added
            ni += 1
    #Append 'wrong image' to img_wimg if sol.
    x is not found within img_wimg or if
    the wrong image has already been added
    if(nf == 0):
        img_wimg = np.append(img_wimg, np.
            array([(sol.x[0], sol.x[1], j-ji,
                sol.fun[0], sol.fun[1])], dtype=
                img_wimg.dtype))
    if(ni == 0):
        img_wimg = np.append(img_wimg, np.
            array([(sol.x[0], sol.x[1], j-ji,
                sol.fun[0], sol.fun[1])], dtype=
                img_wimg.dtype))

    count += 1

else: #so a failure... and optimize.root didn't
converge
    if(img_fail.size == 0): #Check if img_fail is
empty
        img_fail = np.append(img_fail, np.array([(sol
            .x[0], sol.x[1], j-ji, sol.fun[0], sol.fun
            [1], 1)], dtype=img_fail.dtype))
    else:
        nf = 0 #count for img_fail to see if sol.x is
        contained within it
        for k in xrange(len(img_fail['x'])):
            d = np.sqrt((img_fail['x'][k] - sol.x[0])
                **2 + (img_fail['y'][k] - sol.x[1])
                **2)
            if(d < 1.e-2):

```



```

nff = 0 #iterator to count the
entries of img_fail that have the
same position and image index(j-ji
)
for l in xrange(len(img_fail['index'
]))):
    if(j-ji == img_fail['index'][l]):
        nff += 1
if(nff == 0): #If the image index was
not found in img_fail, append the
new 'failed' solution to img_fail
    img_fail = np.append(img_fail, np
        .array([(sol.x[0], sol.x[1], j
        -ji, sol.fun[0], sol.fun[1],
        1)], dtype=img_fail.dtype))
elif(j-ji == img_fail['index'][k]): #
If the image index was found in
img_fail and it is the same image
as the current img_fail, then
increase it's count
    img_fail['count'][k] += 1

    nf += 1
if(nf == 0 ):
    img_fail = np.append(img_fail, np.array
        ([(sol.x[0], sol.x[1], j-ji, sol.fun
        [0], sol.fun[1], 1)], dtype=img_fail.
        dtype))
    count += 1

#Give initial guess of projected-forward position a
bit of randomization
a = 0.5*np.random.rand(2)
image[0] = img['x'][j] + a[0]/2
image[1] = img['y'][j] + a[1]/2

```

```

        #If count reaches max # of iterations, break out of
        loop
        #Print number of wrong and failed images
        if (count == maxiter):
            print 'wrong_images:', img_wimg.shape
            print 'failed_images:', img_fail.shape
            success = False
            break

    #f.write('% .18f % .18f %3i %3i %3i %
    .18E % .18E \n' % (solx, soly, slab[i], j, num[i],
    funx, funy))
    #np.savetxt(f, np.array([solx, soly, img['source'][i], j
    + 1, num[i], funx, funy]).reshape(
    # (1, 7)), fmt='% .18f % .18f %3i %3i %3i
    % .18E % .18E', newline='\n')
    #f2.write('%i %i %s %i \n' % (i, j, solsuc,
    num_iters))
    #np.savetxt(f2, np.array([i + 1, j + 1, solsuc, num_iters
    ]
    # .reshape((1, 4)), fmt='%i %i
    %s %i', newline='\n')

#Print status of projected-forward positions with source i
print 'source:', i+1, 'with', diff, '#_of_images'
print 'img_sol:', img_sol
print 'img_wimg:', img_wimg
print 'img_fail:', img_fail

#Check to see if there are any image solutions that failed to
    be found
nfail = 0
for k in xrange(len(img_sol)):
    d = np.sqrt(img_sol['x'][k]**2 + img_sol['y'][k]**2)
    if (d < 1.e-6):

```

```

nfail += 1

print 'nfail:', nfail
'''
Note that the code below will copy the failed image solutions
to the img_sol array if no new image is found. This
usually happens when two converge and are near a critical
line. External code can be used to investigate if near a
critical line.
'''

wimg = [] #empty list for index of 'wrong images' that match
a solution in img_sol
ring = [] #empty list for index of 'reference images'
#Iterate through img_wimg to see if entry in img_wimg is not
within img_sol (then accept it based on img id -> img_wimg
[2,:]) or it is (then will look for another solution
around original image)
ep = 1.e-6
for m in xrange(len(img_wimg['x'])):
    count = 0
    for n in xrange(len(img_sol['x'])): #iterate through
img_sol to find matches of current img_wimg selection
        d = np.sqrt((img_sol['x'][n] - img_wimg['x'][m])**2 +
                    (img_sol['y'][n] - img_wimg['y'][m])**2)
        if(d < ep):
            wimg.append(m)
            ring.append(n)
            print wimg, ring
            count += 1

if(count == 0):
    d = np.sqrt((img_sol['x'][int(img_wimg['index'][m])])
                **2 + (img_sol['y'][int(img_wimg['index'][m])])
                **2)

```

```

if(d < ep): #if img_sol is (0., 0.)
    img_sol['x'][int(img_wimg['index'][m])] =
        img_wimg['x'][m]
    img_sol['y'][int(img_wimg['index'][m])] =
        img_wimg['y'][m]
    img_sol['fx'][int(img_wimg['index'][m])] =
        img_wimg['fx'][m]
    img_sol['fy'][int(img_wimg['index'][m])] =
        img_wimg['fy'][m]
else: #check if current img_wimg is a better solution
       than the stored img_sol of img_wimg[2,m]
    fun = np.sqrt(img_sol['fx'][int(img_wimg['index']
        ][m])**2 + img_sol['fy'][int(img_wimg['index']
        ][m])**2) #f for img_sol that img_wimg points
        too with img_wimg[2,m]
    fun2 = np.sqrt(img_wimg['fx'][m]**2 + img_wimg['
        fy'][m]**2) #f for current img_wimg
    if(fun > fun2):
        img_sol['x'][int(img_wimg['index'][m])] =
            img_wimg['x'][m]
        img_sol['y'][int(img_wimg['index'][m])] =
            img_wimg['y'][m]
        img_sol['fx'][int(img_wimg['index'][m])] =
            img_wimg['fx'][m]
        img_sol['fy'][int(img_wimg['index'][m])] =
            img_wimg['fy'][m]
else:
    print 'This_”wrong_image:” ', m, 'matches_img_sol:',
        rimg[wimg.index(m)]

```

```

'''

```

img_sol should now contain any entries of *img_wimg* that do not match any previous *img_sol* and are therefore unique solutions. In addition, if there is a match, *wimg* contains the index, *k*, of *img_wimg* that does match the *img_sol* entry with index at *img_wimg*[2,int(*wimg*[*k*])], this will be used later when searching for a new solution around the original image

A magnitude check will be performed. The magnitude at each point of *img_wimg* that matches an entry in *img_sol*. Based on *imgsol_magcheck.py*, the cutoff magnitude will be 100, every point >100 is an outlier and thus near a critical line. Thus, two images merge together. If *mag* > 100, image at index, *img_wimg*[*k*] will be copied to image at *img_wimg*['index'][int(*wimg*[*k*])]

Next part will look for an additional image solution near the reference image.

A line (*x*-axis) will be formed with the original image (*img_wimg*[2,[*wimg*[*k*]]) as vertex and contains the nearest image. A perpendicular line (*y*-axis) will also be formed, that makes a coordinate axis with the original line. The four axis lines will be used as starting points to search for a new image that is different from *img_wimg*.

```
mag_cut = 100. #cut off for magnitude check
```

```
print wimg
```

```
for m in wimg:
```

```
magx, magy = img_wimg['x'][m], img_wimg['y'][m]
```

```
print magx, magy
```

```
#Calculate the magnitude, mu
```

```

kappa = glparas.kappa_pl((magx,magy), d_ls[i]/d_ol[i]/
    d_os[i], px, py, pwidth, pmass, len(px))
gamma1 = glparas.gamma1_pl((magx,magy), d_ls[i]/d_ol[i]/
    d_os[i], px, py, pwidth, pmass, len(px))
gamma2 = glparas.gamma2_pl((magx,magy), d_ls[i]/d_ol[i]/
    d_os[i], px, py, pwidth, pmass, len(px))
detA = ((1 - kappa)**2 - gamma1**2 - gamma2**2)
mu = 1. / detA

print 'Magnitude_of_',mu

if(np.abs(mu) > mag_cut): #If the magnitude is higher
    than the cut, this image is near the critical line.
    Copy this image to img_sol
    index = wimg.index(m)
    img_sol['x'][int(img_wimg['index'][m])] = img_sol['x'
        ] [rimg[index]]
    img_sol['y'][int(img_wimg['index'][m])] = img_sol['y'
        ] [rimg[index]]
    img_sol['fx'][int(img_wimg['index'][m])] = img_sol['
        fx' ] [rimg[index]]
    img_sol['fy'][int(img_wimg['index'][m])] = img_sol['
        fy' ] [rimg[index]]

    del wimg[m] #delete entry from wimg list

print 'Mag_check_done_for_wrong_images'

#Search for new image by making a coordinate system centered
    on the original image position of img_wimg
print 'wimg:', wimg
for n in xrange(len(wimg)):
    #Grab coordinates of image, p1 is original image and p2
    is nearest image (probably the solution that the
    algorithm converged too)

```

```

p1, p2 = np.zeros(2), np.zeros(2)
p1[0], p1[1] = refx[img_wimg['index'][wimg[n]]], refy[
    img_wimg['index'][wimg[n]]]
p2[0], p2[1] = refx[rimg[n]], refy[rimg[n]]

print p1
print p2

m, b = line(p1, p2) #get slope and y-intercept of line
    between images
m_per = -(m)**-1 #get slope of perpendicular line that
    contains the converged solution
b_per = p1[1] - m_per * p1[0] #get y-intercept of
    perpendicular line

print m, b
print m_per, b_per

xc, yc = p1

# Now search along coordinate axes, x-axis is the line
    between the two image points
# y-axis is the perpendicular line, r is the radius from
    the center point of intersection
r = 0.0
image = np.zeros(2)
r_max = 5.0
newimage = False
print 'n:', n
while(r < r_max):
    r += 0.1
    print 'r_=_', r
    for l in xrange(4):
        if(l == 0): #For positive along new 'x-axis'
            image = ptonline(xc, yc, m, b, r, True)

```

```

if(l == 1): #For positive along new 'y-axis'
    image = ptonline(xc, yc, m_per, b_per, r,
                    True)
if(l == 2): #For negative along new 'x-axis'
    image = ptonline(xc, yc, m, b, r, False)
if(l == 3): #For negative along new 'y-axis'
    image = ptonline(xc, yc, m_per, b_per, r,
                    False)
#print 'image:', image
sol = optimize.root(fvec, image)
#Check if successful convergence, then see if
    converged to a different image
#print sol.x, sol.success
if(sol.success == True):
    if(np.abs(img_wimg['x'][int(n)] - sol.x[0]) >
        1.0e-2 and (np.abs(img_wimg['y'][int(n)]
        - sol.x[1]) > 1.0e-2)):
        #print sol.x

    idif = 0 #count for if succussful
        solutions are different from new
        solution
    for k in xrange(len(img_sol['x'])):
        if(np.abs(img_sol['x'][k]-sol.x[0]) <
            1.0e-2 and np.abs(img_sol['y'][k]
            ]-sol.x[1]) < 1.0e-2):
            idif += 1

if(idif == 0):
    #Check if the new solution is an
        actual solution of this source set
    d = np.sqrt((sol.x[0] - p1[0])**2 + (
        sol.x[1] - p1[1])**2)

```



```

#If the distance between the solution
and original image is greater
than either 1.5*rmax or 2*(dist
between p1 and p2) then reject it
if ( (d > r_max*1.5) or (d > 2*np.sqrt
((p1[0]-p2[0])**2 + (p1[1]-p2[1])
**2)) ):
    np.savetxt(f2, np.array([img[ '
source '][i], img_wimg[ 'index '
][wimg[n]], img[ 'num '][i], sol
.x[0], sol.x[1], sol.fun[0],
sol.fun[1], p1[0], p1[1]]).
reshape((1, 9)), fmt='%i _%i _
%i _%.18f _%.18f _%.18f _
%.18f _%.18E _%.18E',
newline='\n')
else:
    print 'new_image: _{0:.18f} _{1:.18
f} _{2:.18E} _{3:.18E}'.format(
sol.x[0], sol.x[1], sol.fun
[0], sol.fun[1])
    img_sol[ 'x '][img_wimg[ 'index '][
int(n)]] = sol.x[0]
    img_sol[ 'y '][img_wimg[ 'index '][
int(n)]] = sol.x[1]
    img_sol[ 'fx '][img_wimg[ 'index '][
int(n)]] = sol.fun[0]
    img_sol[ 'fy '][img_wimg[ 'index '][
int(n)]] = sol.fun[1]
    newimage = True
    r = r_max #break out of while
loop
    break #break out of for loop

if(newimage == False):

```

```

img_sol['x'][img_wimg['index'][int(n)]] = img_wimg['x
    '][int(n)]
img_sol['y'][img_wimg['index'][int(n)]] = img_wimg['y
    '][int(n)]
img_sol['fx'][img_wimg['index'][int(n)]] = img_wimg['
    fx'][int(n)]
img_sol['fy'][img_wimg['index'][int(n)]] = img_wimg['
    fy'][int(n)]

print 'img_sol:', img_sol

'''
The next part of code will deal with failed image solutions.
These are positions that the algorithm did not
successfully converge with.

First a magnitude check is performed with mag_cut = 100. If
the mag > 100, then the image position is near a critical
line and thus could make it hard for the algorithm to
converge.

Then, the 'count' of each entry in img_fail will be
investigated. The count of each entry corresponds to the
number of times the algorithm stopped at that position.
For each image index, the position with the highest number
of counts will be recorded to img_sol.
'''

mag_cut = 100. #cut off for magnitude check

for m in xrange(len(img_fail['index'])):
    magx, magy = img_fail['x'][m], img_fail['y'][m]
    print magx, magy

```

```

#Calculate the magnitude, mu
kappa = glparas.kappa_pl((magx,magy), d_ls[i]/d_ol[i]/
    d_os[i], px, py, pwidth, pmass, len(px))
gamma1 = glparas.gamma1_pl((magx,magy), d_ls[i]/d_ol[i]/
    d_os[i], px, py, pwidth, pmass, len(px))
gamma2 = glparas.gamma2_pl((magx,magy), d_ls[i]/d_ol[i]/
    d_os[i], px, py, pwidth, pmass, len(px))
detA = ((1 - kappa)**2 - gamma1**2 - gamma2**2)
mu = 1. / detA

print 'Magnitude_of_',mu

if(np.abs(mu) > mag_cut): #If the magnitude is higher
    than the cut, this image is near the critical line.
    Copy this image to img_sol
    index = img_fail['index'][m]
    if(img_fail['count'][m] == np.amax(img_fail['count']
    )):
        img_sol['x'][index] = img_fail['x'][m]
        img_sol['y'][index] = img_fail['y'][m]
        img_sol['fx'][index] = img_fail['fx'][m]
        img_sol['fy'][index] = img_fail['fy'][m]

print 'Mag_check_done_for_failed_images'

nz = 0 #number of zeros in img_sol
for m in xrange(len(img_sol['x'])):
    d = np.sqrt(img_sol['x'][m]**2 + img_sol['y'][m]**2)
    if(d < 1.e-6):
        nz += 1

if(nz != 0):
    for m in xrange(diff):
        maxfc = 0 #max failed counts
        for n in xrange(len(img_fail['index'])):

```

```

if(m == img_fail['index'][n] and maxfc < img_fail
    ['count'][n]):
    maxfc = img_fail['count'][n]
    img_sol['x'][m] = img_fail['x'][n]
    img_sol['y'][m] = img_fail['y'][n]
    img_sol['fx'][m] = img_fail['fx'][n]
    img_sol['fy'][m] = img_fail['fy'][n]

print 'img_sol:', img_sol

#Write img_sol for source i and image j
for j in xrange(len(img_sol)):
    np.savetxt(f, np.array([img_sol['x'][j], img_sol['y'][j],
        img['source'][i], j + 1, img['num'][i], img_sol['fx'
        ][j], img_sol['fy'][j]]).reshape((1, 7)), fmt='%...18f
        ...%...18f...%3i...%3i...%3i...%...18E...%...18E'
        , newline='\n')

```

